APPLIED COMPUTER SCIENCE

The Journal is a peer-reviewed, international, multidisciplinary journal covering a broad spectrum of topics of computer application in production engineering, technology, management and economy.

The main purpose of Applied Computer Science is to publish the results of cutting-edge research advancing the concepts, theories and implementation of novel solutions in computer technology. Papers presenting original research results related to applications of computer technology in production engineering, management, economy and technology are welcomed.

We welcome original papers written in English. The Journal also publishes technical briefs, discussions of previously published papers, book reviews, and editorials. Especially we welcome papers which deals with the problem of computer applications in such areas as:

- manufacturing,
- engineering,
- technology,
- designing,
- organization,
- management,
- economics,
- innovations,
- competitiveness,
- quality and costs.

The Journal is published quarterly and is indexed in: BazTech, Cabell's Directory, Central & Eastern European Academic Source (CEEAS), CNKI Scholar (China National Knowledge Infrastucture), DOAJ (Directory of Open Access Journals), EBSCO, ERIH PLUS, Index Copernicus, J-Gate, Google Scholar, Scope Database, Scopus, TEMA Technik und Management.

Letters to the Editor-in-Chief or Editorial Secretary are highly encouraged.

CONTENTS

Applied Computer Science, vol. 18, no. 2, pp. 5–15
doi: 10.35784/acs-2022-9

Submitted: 2022-04-17 | Revised: 2022-06-14 | Accepted: 2022-06-18

Keywords: serious game, MCI (Mild Cognitive Impairment), cognition, dementia, MMSE

Moon-gee CHOI [0000-0002-5762-2172]*

USE OF SERIOUS GAMES FOR THE ASSESSMENT OF MILD COGNITIVE IMPAIRMENT IN THE ELDERLY

Abstract

This study investigated the use of computer games to detect the symptoms of mild cognitive impairment (MCI), an early stage of dementia, in the elderly. To this end, three serious games were used to measure the visio-perception coordination and psycho-motor abilities, spatial memory, and short-term digit span memory. Subsequently, the correlations between the results of the games and the results of the Korean Mini-Mental State Examination (K-MMSE), a dementia screening test, were analyzed. In addition, the game results of normal elderly persons were compared with those of elderly patients who exhibited MCI symptoms. The results indicated that the game play time and the frequency of errors had significant correlations with K-MMSE. Significant differences were also found in several factors between the control group and the group with MCI. Based on these findings, the advantages and disadvantages of using serious games as tools for screening mild cognitive impairment were discussed.

1. INTRODUCTION

Serious games refer to games designed with content devised to achieve specific objectives in areas such as education, training, and health through fun and accessible everyday play. The utilization value of serious games is significant as they provide education, training, or testing through motivational content, and their accessibility enables processes that previously needed to be experienced face-to-face or directly to be carried out on a large scale through computers and online access (Granic, Lobel, & Engels, 2014).

Serious games are particularly useful in large-scale medical diagnosis and in screening for jobs. One of the recent leading applications has been medical serious games used for testing cognitive impairment or dementia in the elderly. Given the difficulty of completely curing dementia once it has developed, discovering and responding to initial symptoms at an early stage provides a decisive advantage for managing the disease and preventing it from becoming severe. The difficulty of discerning early dementia or mild cognitive impairment (MCI) requires the repeated testing of a large number of the elderly. Such ongoing large-scale testing is problematic (Connolly, Gaehl, Martin, Morris, & Purandare, 2011; Lopponen, Raiha, Isoaho, Vahlberg, & Kivela, 2003; Scanlon, O'Shea, O'Caoimh, Timmons, 2015).

* Department of Liberal Arts, University of Konyang, Konyang, South-Korea, mgchoi@konyang.ac.kr

Consequently, it is highly useful to develop digital content such as serious games that are easily accessible, can accommodate many users simultaneously, prevent boredom during tests, and can be carried out in a fun way.

This study aimed to determine the possibility of diagnosing MCI, an early stage of dementia, by applying various cognitive measurement algorithms related to MCI to computer-based serious games. To this end, this study implemented three cognitive measurement algorithms based on MCI in the form of serious games and compared various behavior data from playing the games between a control group and patient group who actually showed MCI symptoms. In addition, the results of the games were analyzed by comparing them with the results of the Korean Mini-Mental State Examination (K-MMSE), a specialized dementia screening test.

1.1. Serious games for dementia prevention

The development of digital cognitive measurement tools and serious games has substantially progressed over the last two decades, and extensive research is still ongoing (Beavis, Dezuanni & O'Mara, 2017). In particular, much functional content for the elderly has been developed to prevent and treat mental or physical degeneration and associated changes. Current serious games for elderly healthcare aim to enhance their physical and mental well-being, and many programs such as Nintendo, Lumosity, Smacare, Brain Training, Elevate Labs, and Psicool have been developed and commercialized.

An especially notable trend is that, although serious games were originally simple training programs created based on experts' recommendations or commonsense, recently they are being applied to specific diagnoses and treatments through more scientific and clinical experiments. For example, Manera et al. (2015) conducted experiments to measure the amnestic mild cognitive impairment (aMCI) and dementia of 21 patients using a serious game called "Kitchen and Cooking" and obtained significant results. Tong, Chignell, Tierney and Lee (2016) also examined whether it is possible for game-based tests to measure cognitive impairment. In addition, various scientific attempts are being made for mental health promotion and testing through digital applications using computerized touch-panels (Fukui et al., 2015), augmented reality, or virtual reality based cognitive training applications (Allain et al., 2014; Boletsis & McCallum, 2016; Tong, Chignell & Tierney, 2016; Zygouris et al., 2015).

Although considerable researches demonstrated that serious games were highly correlated with other methods of cognitive assessment for MCI and dementia, this field is quiet young and more questions and researches are needed. In this study, we tried to verify the possibility of diagnosing MCI with computer game trying to improve two aspects of previous studies. First, most of previous researches compared the simple game score between healthy group and MCI group. However, in computer-based serious games, various behavioral data, as well as the targeted cognitive aspects, can be systematically and efficiently collected and assessed and various characteristics associated to target disorder can be analyzed with the data. Second, most of previous researches used small size of sample less than 25 participants. However, for using serious game as diagnostic tools for massive population to screen clinical and pre-clinical conditions in the early stages of MCI, we need to verify the validity of serious games in a similar condition.

1.2. Assessment of cognitive impairment

Alzheimer's disease, a degenerative disease, is characterized by gradual onset and progression, and cognitive impairment gradually develops before full-scale behavioral and neurological symptoms are evident (World Health Organization, 2019). MCI refers to this stage of preclinical Alzheimer's disease. This is a condition in which, clinically, cognitive abilities and functional activities are relatively preserved, except for memory that has deteriorated with age. Furthermore, daily unassisted living is still possible and a diagnosis of dementia is unwarranted (Langa, & Levine, 2014). The diagnosis of MCI is important in several aspects. Early diagnosis enables the healthy period of the patient to be prolonged through early management and treatment, it allows patients to plan for the future and enables patients to preserve their quality of life (Ismail, Rajji & Shulman, 2010).

There are two main types of diagnostic tools for MCI or early dementia: screening tests and neuropsychological tests. Screening tests roughly evaluate the state of cognitive functions and the existence or absence of cognitive decline, whereas neuropsychological tests evaluate each sub-cognitive domain in detail. A representative example of the former is the MMSE (Folstein, Folsten & McHugh, 1975), which is the test most widely used. A representative example of the latter is the Consortium to Establish a Registry for Alzheimer's Disease (CERAD) assessment packet (Morris et al., 1989).

Although these two tests are considered the standard methods, with proven reliability and validity for the diagnosis of MCI (Baek, Kim, Park, & Kim, 2016), they have several limitations. Because they are pencil-and-paper-based methods, they must be carried out face-to-face and are thus not suitable diagnostic tools when we wish to assess the cognitive problems of a large number of people simultaneously. In contrast, serious games can be a good solution. With computer-based serious games, cognitive impairment and, further, the changes or reduction in cognitive abilities can be systematically measured, analyzed, and managed by repetitive play on a computer or a smartphone. This allows for the identification of dementia risk groups, which can, in turn, lead to more professional examination and treatment in partnership with specialized treatment institutions such as geriatric hospitals.

2. METHOD

2.1. Participants

The Ansan Geriatric Study in Korea – an ongoing prospective population-based cohort study among subjects that are at least 60 years old and live in the Korean city of Ansan – provided the clinical information and participants for this study. The participants in this study were 342 of 588 elderly people who participated in the Ansan Geriatric Study and who consented to participate in this study. Informed written consent for participation was obtained from each individual. Of the 342 participants, 62 were diagnosed as having an amnesic type of MCI and 280 as having no cognitive impairment (control).

2.2. Materials

2.2.1. Computerized assessment tools (serious games)

This study used three serious games: “Get Persimmon,” “Set the Table,” and “Elevator.” These computer games are prototypes developed for cognitive measurement by specialized programmers and have relatively simple goals and levels (difficulty).

Fig. 1. Screenshots of the games “Get Persimmon,” “Set the Table,” and “Elevator”

The first game, Get Persimmon, assesses visio-perception coordination and psycho-motor ability (see Figure 1). In this game, there is a bear doll on the screen that can be moved with the mouse to receive falling persimmons. There are two types of persimmons: dark purple rotten persimmons and scarlet ripe persimmons. Participants must avoid rotten persimmons and catch ripe persimmons before they fall to the ground. The number of falling persimmons changes over time. In this study, one level was set for measurement. The measured variables were total play time and mouse moving distance until the preset number of persimmons (50) was received.

The second game, Set the Table, assesses spatial memory and visual short-term memory (see Figure 1). Specifically, it assesses the ability to remember the types and positions of side dishes on the table and reproduce them correctly on the table. There are two difficulty levels: Levels 1 and 2. Participants first look at a picture that is shown to them and are then required to find and place, in their original positions, three foods in Level 1 and six foods in Level 2. Each level is played three times, and if the participant makes five or more errors, the game moves on to the next trial. The assessment variables are the total performance time at each level, number of errors until the game is finished, and reaction time from watching the presented picture until starting to set the table.

The third game, Elevator, is the same as the digit span task that assesses auditory short-term memory (see Figure 1). The participants must listen to the number of floors that the elevator must stop at and push the relevant floor numbers. There are two levels of difficulty: Levels 1 and 2. Participants must press the buttons in the correct order after listening to three floors in Level 1 and six floors in Level 2. Each level is played three times, and if the participant makes five or more errors, the game moves on to the next trial. The assessment variables are the time it takes until the correct buttons are pressed at each level and number of errors.

2.2.2. Korean Mini-Mental State Examination (K-MMSE)

This study used the K-MMSE, created by Kwon and Park (1989) for the Korean elderly and which revised the MMSE that was developed as a screening test for cognitive impairment and dementia in the elderly by Folstein et al. (1975). It is a widely used tool with proven reliability and validity (Cronbach's α of 0.86). K-MMSE consists of 19 questions that measure time orientation (5 points), spatial orientation (5 points), memory registration (3 points), attention and calculation (5 points), memory recall (3 points), language (8 points), and space–time configuration (1 point). The highest score is 30 points with a higher score signifying higher cognitive function. Scores in the range of 18 to 23 are associated with MCI, and scores below this range signify severe cognitive impairment.

2.3. Process

We analyzed the results of games played by participants after they had undergone a medical examination at the hospital. They played the games on three laptop computers. No penalty was given if they stopped a game in the middle or moved on to a different game. The experimenter collected simple personal information (to match with the clinical information provided by the Ansan Geriatric Study) from the participants who finished at least one of the three games and gave them simple souvenirs as a reward for participating.

3. RESULTS

Participant data were included in the results only if each level unit was played from the beginning to the end in each game; the data of the uncompleted level units were excluded from the analysis. First, the demographic and clinical characteristics were compared, via unpaired Student t test or ANOVA for continuous variables and by $\chi 2$ test for categorical variables, and the analysis was performed using SPSS for Windows, version 18.0. The two groups had significant differences in age and education, but not gender. The average age of the MCI group was two years older than that of the control, and the education of the MCI group was also higher. Moreover, the K-MMSE score for screening dementia also showed a statistically significant difference (see Table 1).

Tab. 1. Mean and standard deviation (in parentheses) for MCI and control group in age, gender, education, and K-MMSE.

Characteristics of Participants	MCI (n = 62)	Control (n = 280)	p-value
Age	73.11 (5.63)	71.22±4.36	0.004*
Gender	62 (18.1%)	280 (81.9%)	1.00a
Education	6.50 (4.57)	8.34 (4.95)	0.006*
K-MMSE	25.13 (3.07)	27.44 (2.00)	0.000*b

* values are presented as mean (SD) or number (%), *P < 0.05: a) $\chi 2$ test for Gender and Clinical group, b) ANCOVA test adjusted for Age and Education

Second, the correlations of the game results with age, education, and K-MMSE were analyzed. Age appears to influence the performance of the games in general. In the Get Persimmon game, age showed a correlation with time. In the Set the Table and Elevator games, age and time showed a positive correlation at the higher level of each game. In the Elevator game, which measures the digit span, age showed a correlation with the number of errors. This implies that age can be an important variable in cognitive aspects, although the correlations were not consistent across the games. Education was another important variable that can influence the result of games. Education showed negative correlations with both the playing time of the game and several other factors. The results of the games also showed a strong correlation with the K-MMSE results. The K-MMSE generally exhibited a negative correlation with the playing time, and the correlation became more general as the difficulty level increased (see Table 2).

Tab. 2. Correlations coefficient between game results and K-MMSE, Age, and Education

Game	Level	Game factors	Age	Education	K-MMSE
"Get Persimmon"		Playing time	0.146*	-0.206*	-0.306*
		Moving distance	-0.004	0.141*	0.099
"Set the Table"	**Level 1**	Number of errors	-0.011	0.006	-0.105
		Reaction time	-0.002	-0.149*	-0.181*
		Playing Time	0.062	-0.210*	-0.308*
	Level 2	Number of errors	0.044	-0.120	-0.139*
		Reaction time	0.114	-0.207*	-0.275*
		Playing Time	0.128*	-0.349*	-0.319*
"Elevator"	**Level 1**	Number of errors	0.160*	-0.007	-0.052
		Playing time	0.051	-0.138*	-0.137*
	Level 2	Number of errors	0.135*	-0.199*	-0.320*
		Playing time	0.123*	-0.356*	-0.504*

* $P < 0.05$

Next, the game results were compared between the control and MCI groups. Given the possibility that age and education might be covariates, they were controlled for. In fact, the differences between the two groups in the results of games by controlling the influence of age and education disappeared in the game playing time. The differences in game playing time were not statistically significant for the Get Persimmon game, which measures visual perception and motor skills, and for the Set the Table game, which measures short-term spatial memory. In contrast, statistical differences were observed in the Elevator game, which measures the digit span, but only in Level 2 of the game. Surprisingly, the difference in reaction time from seeing the items to memorize until actually taking action to play the game in the Set the Table game was significant in both Levels 1 and 2, even when the influence of age and education were controlled. This indicates that cognitive impairment is not simply associated with long playing time.

The last difference between the two groups is the number of errors. The number of errors showed statistically significant differences in Level 2 of the Set the Table game and Level 2 of the Elevator game and not in Level 1 in both games. This suggests that MCI is related to the number of errors only when the games require some level of difficulty.

Tab. 3. Mean and standard deviation (in parentheses) for MCI and control group in game results and *F*-value and *P*-value in ANCOVA test adjusted for Age and Education.

Game	Level	Game factors	MCI	Control	*F*-value	*P*-value
"Get Persimmon"		Playing time	83.06 (19.32)	76.25 (18.37)	3.6	0.059
		Moving distance	6078.51 (2668.82)	6398.94 (2939.76)	0.28	0.595
"Set the Table"	**Level 1**	Number of errors	0.42 (0.90)	0.39 (1.01)	0.05	0.821
		Reaction time	6.79 (5.08)	5.16 (2.89)	8.4	0.004*
		Playing time	59.04 (20.73)	56.47 (19.48)	0.04	0.833
	Level 2	Number of errors	3.27 (3.70)	2.20 (2.50)	4.04	0.045*
		Reaction time	10.29 (7.35)	7.77 (4.21)	6.36	0.012*
		Playing time	77.46 (36.03)	66.64 (27.76)	1.44	0.231
"Elevator"	**Level 1**	Number of errors	0.70 (1.25)	.56 (1.27)	0.14	0.705
		Playing time	12.94 (10.32)	10.99 (9.18)	1.23	0.268
	Level 2	Number of errors	0.98 (1.77)	2.34 (3.42)	16.27	0.000*
		Playing time	25.59 (15.18)	16.42 (9.67)	26.57	0.000*

* $P < 0.05$

4. DISCUSSIONS

Dementia currently has no treatment that can reverse the cognitive decline and restore cognitive functions to their prior levels. The only realistically possible countermeasure is to lower the incidence rate by controlling risk factors for dementia in advance and to retard the progression of dementia symptoms through early diagnosis and appropriate interventions (National Institute of Dementia, 2019). Therefore, intervention and cognitive assessment to diagnose MCI have crucial significance. The large-scale identification of early symptoms such as MCI cannot be achieved solely by the standard medical approach of pencil-and-paper testing; a more convergent approach that includes public healthcare and information and communication technologies is required.

This study aimed to determine the possibility of diagnosing MCI, an early stage of dementia, by applying various cognitive measurement algorithms related to MCI to computer-based serious games. To this end, the results of serious games were compared between patients with MCI symptoms and a control group, and also with the results of the K-MMSE specialized dementia screening test. The results show a clear difference in the K-MMSE between the MCI group and the control group, who were screened from the population over the age of 60 in Ansan, Korea. Moreover, the differences in age and education between the two groups also showed statistical significance, and similar tendencies can also be found in previous studies (e.g., Koster et al., 2005; Suh, Ju, Yeon, & Shah, 2004).

In the comparison between the game results and the K-MMSE, relatively strong correlations were observed in the game playing time, number of errors, and difficulty. However, we cannot exclude the possibility that the high correlations between the results of the serious games and K-MMSE could have been caused by the influence of age and education because it can be inferred that the age and education factors can have a significant effect on the cognitive performance related to the games. Consequently, an ANCOVA test was conducted to analyze whether the control group and the MCI group would show differences in the game results in a situation that excluded the influence of education and age. It was found that although there were differences by game and difficulty level, the results of the serious games showed their potential as auxiliary tests to distinguish between normal people and people with MCI, and also some limits. A few important implications and issues found based on analysis of the results are as follows.

First, the level of difficulty in games is very important in the design of games to distinguish between normal people and people with MCI. The games were designed with very low levels of difficulty in this study because the elderly are not accustomed to digital games. Hence, as shown in the results, the two groups exhibited no statistical difference; consequently, level 1 is not useful as a discriminator. By contrast, at Level 2, which is more difficult, the two groups showed a tendency of differences in game performance. Although more research is required regarding the relation between cognitive impairment severity and the difficulty of tasks, designing the level of difficulty to gradually increase from the very basic game level is deemed a crucial factor in serious games to distinguish between normal people and people with MCI.

Second, in computer-based serious games, various behavioral data, as well as the targeted cognitive aspects, can be systematically and efficiently collected and assessed. For example, the moving distance can be measured by mouse movement and the number of mouse clicks in the Get Persimmon game, and the types of errors, such as false positive or false negative error can be measured in the Elevator game. In this way, much behavioral data can be collected and analyzed for research on various aspects of disorder. For example, the reaction time from watching the presented picture until starting to set the table in the Set the Table game had not been expected at the beginning of the experiment to be conducive to distinguishing between normal people and people with MCI. However, this delayed reaction time can finally be employed as a highly useful factor for diagnosing MCI because such a difference in reaction time appeared regardless of the difficulty of the games. It appears to be associated with cognitive flexibility (Chelune & Baer, 1986) or executive function (Diamond, 2013), but more detailed research is required for a more accurate cognitive-based explanation. Nevertheless, this finding suggests that one of the advantages of using serious games as a diagnostic tool is that such diverse behavioral data can be derived and analyzed.

Third, cognitive abilities naturally decline with age rather than being preserved for the most part, and social factors like education may also make a difference. In other words, demographic factors such as age and education can have greater effects on game performance associated with cognitive functions. In particular, one of the major factors that can be influenced by demographic factors in serious games is playing time. As expected, the correlation analysis showed that the playing time and K-MMSE had a significant correlation, but it is very surprising that the relation disappeared when the group difference in game performance was analyzed with age and education as covariates. This suggests that the difference in playing time between groups can be sufficiently caused by demographic differences such as age and education, rather than being caused simply by cognitive impairment. In short, for screening MCI using serious games, we must calculate the effect of cognitive impairment on the games beyond the influence of demographic factors such as age and education. This requires a comprehensive approach that reflects various factors such as difficulty, reaction time (see, Tong, Chignell, Tierney, & Lee, 2016), and the number of errors, rather than just one factor.

5. CONCLUSIONS

The limitations of the standard pencil-and-paper diagnostic medical and psychological tests limit the ease with which they can be repeatedly applied to a large group of patients. Computer-based, serious games, on the other hand, permit low-cost, repetitive screening for MCI and, additionally, allow for investigation into various behavioral aspects that standard testing does not permit.

This study explored the possibility of screening MCI, an early stage of dementia, with serious games using various behavior data and relatively large size of sample. The experimental results showed the possibility that groups of general people and people with MCI can be distinguished based on various behavioral data obtained from the serious games. Furthermore, the results showed the significant correlation between game data and the score of K-MMSE.

Finally, serious game consists normally of two important components; functional and enjoyable. While the computer games developed in this study showed well the possibility of diagnostic tool as a functional component, the other component related to fun and motivation of the game is not taken into account for the study. More various and empirical researches about interaction between human and computer game including motivation, usability, engagement and so on will need to be accumulated to make game-based cognitive assessment not only accurate but also realistic and fun tests.

Funding

This research was funded by the Konyang University Research Fund in 2021.

Acknowledgments

I would like to thank Moon ho Park, who is responsible for the Ansan Geriatric Study in Korea and Ntelligent Games, Inc., who developed and provided the serious games for this study. I would also like to thank Editage (www.editage.co.kr) for English language editing.

Conflicts of Interest

There are no conflicts of interest.

Ethical Declaration

All study participants provided informed consent, and the study design was approved by the appropriate ethics review board.

REFERENCES

Allain, P., Foloppe, D. A., Besnard, J., Yamaguchi, T., Etcharry-Bouyx, F., Le Gall, D., Nolin, P., & Richard, P. (2014). Detecting everyday action deficits in Alzheimer's disease using a nonimmersive virtual reality kitchen. *Journal of the International Neuropsychological Society, 20*, 468–477.

Baek, M. J., Kim, K., Park, Y. H., & Kim, S. (2016). The validity and reliability of the Mini-Mental State Examination-2 for detecting mild cognitive impairment and Alzheimer's disease in a Korean population. *PLoS One*, *11*(9), e0163792. https://doi.org/10.1371/journal.pone.0163792

Beavis, C., Dezuanni, M., & O'Mara, J. (2017). *Serious play: Literacy, learning and digital games*. Taylor & Francis. https://doi.org/10.4324/9781315537658-1

Boletsis, C., & McCallum, S. (2016). Augmented reality cubes for cognitive gaming: Preliminary usability and game experience testing, *International Journal of Serious Games*, *3*(1), 3–16. https://doi.org/10.17083/ijsg.v3i1.106

Chelune, G. J., & Baer, R. A. (1986). Developmental norms for the Wisconsin Card Sorting Test. *Journal of Clinical and Experimental Neuropsychology, 8*(3), 219–228. http://doi.org/10.1080/01688638608401314

Connolly, A., Gaehl, E., Martin, H., Morris, J., & Purandare, N. (2011). Underdiagnosis of dementia in primary care: Variations in the observed prevalence and comparisons to the expected prevalence. *Aging & Mental Health, 15*(8), 978–984. https://doi.org/10.1080/13607863.2011.596805

Diamond, A. (2013). Executive functions. *Annual Review of Psychology, 64*, 135–168. https://doi.org/10.1146/annurev-psych-113011-143750

Folstein, M., Folsten, S., & McHugh, P.(1975). Mini-Mental State: A practical method for grading the cognitive state of patients for the clinician. *Journal of Psychiatric Research, 12*, 189–198. https://doi.org/10.1016/0022-3956(75)90026-6

Fukui, Y., Yamashita, T., Hishikawa, N., Kurata, T., Sato, K., Omote, Y., Kono, S., Yunoki, T., Kawahara, Y., Hatanaka, N., Tokuchi, R., Deguchi, K., & Abe, K. (2015). Computerized touch-panel screening tests for detecting mild cognitive impairment and Alzheimer's disease. *Internal Medicine, 54*, 895–902. https://doi.org/10.2169/internalmedicine.54.3931

Granic, I., Lobel, A., & Engels, R.C. (2014). The benefits of playing video games. *The American Psychologist, 69*(1), 66–79. https://doi.org/10.1037/a0034857

Ismail, Z., Rajji, T. K., & Shulman, K. I. (2010). Brief cognitive screening instruments: an update. *International journal of geriatric psychiatry, 25*(2), 111–120. https://doi.org/10.1002/gps.2306

Koster, A., Penninx, B. W., Bosma, H., Kempen, G. I., Newman, A. B., Rubin, S. M., Satterfield, S., Atkinson, H. H., Ayonayon, H. N., Rosano, C., Yaffe, K., Harris, T. B., Rooks, R. N., Van Eijk, J. T., & Kritchevsky, S. B. (2005). Socioeconomic differences in cognitive decline and the role of biomedical factors. *Annals of epidemiology, 15*(8), 564–571. https://doi.org/10.1016/j.annepidem.2005.02.008

Kwon, Y. C., & Park, J. H. (1989). Korean Version of Mini-Mental State Examination (K-MMSE). *Journal of Korean Neuropsychiatric Association, 28*(1), 125–135.

Langa, K. M., & Levine, D. A. (2014). The diagnosis and management of mild cognitive impairment: a clinical review. *JAMA, 312*(23), 2551–2561. https://doi.org/10.1001/jama.2014.13806

Löppönen, M., Räihä, I., Isoaho, R., Vahlberg, T., & Kivelä, S. L. (2003). Diagnosing cognitive impairment and dementia in primary health care -- a more active approach is needed. *Age and ageing, 32*(6), 606–612. https://doi.org/10.1093/ageing/afg097

Manera, V., Petit, P. D., Derreumaux, A., Orvieto, I., Romagnoli, M., Lyttle, G., David, R., & Robert, P. H. (2015). 'Kitchen and cooking,' a serious game for mild cognitive impairment and Alzheimer's disease: a pilot study. *Frontiers in aging neuroscience, 7*, 24. https://doi.org/10.3389/fnagi.2015.00024

Morris, J. C., Heyman, A., Mohs, R. C., Hughes, J. P., van Belle, G., Fillenbaum, G., Mellits, E. D., & Clark, C. (1989). The CERAD Investigators. The Consortium to Establish a Registry for Alzheimer's Disease (CERAD). Part I: Clinical and neuropsychological assessment of Alzheimer's disease. *Neurology*, *39*, 1159–1165. https://doi.org/10.1212/wnl.39.9.1159

National Institute of Dementia. (2019). *National Institute of Dementia annual report 2019*. Seongnam: National Institute of Dementia. https://nih.go.kr/contents.es?mid=a50302010000

Scanlon, L., O'Shea, E., O'Caoimh, R., & Timmons, S. (2015). Usability and validity of a battery of computerised cognitive screening tests for detecting cognitive impairment. *Gerontology*, *62*(2), 247–252. https://doi.org/10.1159/000433432

Suh, G. H., Ju, Y. S., Yeon, B. K., & Shah, A. (2004). A longitudinal study of Alzheimer's disease: rates of cognitive and functional decline. *International journal of geriatric psychiatry*, *19*(9), 817–824. https://doi.org/10.1002/gps.1168

Tong, T., Chignell, M., Tierney, M. C., & Lee, J. (2016). A Serious Game for Clinical Assessment of Cognitive Status: Validation Study. *JMIR serious games*, *4*(1), e7. https://doi.org/10.2196/games.5006

World Health Organization. (2021). *Global action plan on the public health response to dementia 2017–2025*. https://www.who.int/news-room/fact-sheets/detail/dementia

Zygouris, S., Giakoumis, D., Votis, K., Doumpoulakis, S., Ntovas, K., Segkouli, S., Karagiannidis, C., Tzovaras, D., & Tsolaki, M. (2015). Can a virtual reality cognitive training application fulfill a dual role? Using the virtual supermarket cognitive training application as a screening tool for mild cognitive impairment. *Journal of Alzheimer's disease: JAD*, *44*(4), 1333–1347. https://doi.org/10.3233/JAD-141260

Applied Computer Science, vol. 18, no. 2, pp. 16–27
doi: 10.35784/acs-2022-10

Submitted: 2022-03-22 | Revised: 2022-05-16 | Accepted: 2022-05-23

Keywords: proteomics, mass spectrometry, distributed computing, Apache Spark

Katarzyna ORZECHOWSKA [0000-0001-9797-1142]*,
Tymon RUBEL [0000-0002-1342-414X]*, *Robert KURJATA* [0000-0001-8547-910X]*,
Krzysztof ZAREMBA [0000-0002-4036-6459]*

A DISTRIBUTED ALGORITHM FOR PROTEIN IDENTIFICATION FROM TANDEM MASS SPECTROMETRY DATA

Abstract

Tandem mass spectrometry is an analytical technique widely used in proteomics for the high-throughput characterization of proteins in biological samples. Modern in-depth proteomic studies require the collection of even millions of mass spectra representing short protein fragments (peptides). In order to identify the peptides, the measured spectra are most often scored against a database of amino acid sequences of known proteins. Due to the volume of input data and the sizes of proteomic databases, this is a resource-intensive task, which requires an efficient and scalable computational strategy. Here, we present SparkMS, an algorithm for peptide and protein identification from mass spectrometry data explicitly designed to work in a distributed computational environment. To achieve the required performance and scalability, we use Apache Spark, a modern framework that is becoming increasingly popular not only in the field of "big data" analysis but also in bioinformatics. This paper describes the algorithm in detail and demonstrates its performance on a large proteomic dataset. Experimental results indicate that SparkMS scales with the number of worker nodes and the increasing complexity of the search task. Furthermore, it exhibits a protein identification efficiency comparable to X!Tandem, a widely-used proteomic search engine.

1. INTRODUCTION

Liquid chromatography-tandem mass spectrometry (LC-MS/MS) is nowadays the method of choice in proteomics, a field of studies aimed at the large-scale analysis of proteins expressed in cells, tissues, and organisms (Aebersold & Mann, 2003; Hernandez, Müller & Appel, 2006). Most proteomic studies follow a "bottom-up" strategy, in which the proteins are first digested into smaller peptides using a proteolytic enzyme. The peptides are then separated by liquid chromatography, ionized, and passed to a tandem mass spectrometer where both the masses of the parent ions and the corresponding mass spectra of their

* Warsaw University of Technology, Institute of Radioelectronics and Multimedia Technology, Poland, orzechowska@ire.pw.edu.pl, trubel@ire.pw.edu.pl, r.kurjata@ire.pw.edu.pl, k.zaremba@ire.pw.edu.pl

fragments are measured. The resulting fragmentation mass spectra (MS/MS spectra) are sequence-specific and can be used for peptide identification. In typical proteomic experiments, from several thousand to tens of millions of MS/MS spectra are collected.

Due to high complexity and sizes ranging up to several gigabytes, tandem mass spectrometry data must be processed in an automated manner. In the currently most popular approach, peptide amino acid sequences are determined by comparing the measured mass spectra with theoretical spectra derived from a database of known proteins (Hernandez, Müller & Appel, 2006; Sadygov, Cociorva & Yates, 2004). To obtain a list of potential peptides, the database is subjected to an *in silico* digestion, in which protein sequences are cut at cleavage sites specific for the proteolytic enzyme used in the experiment. Depending on the database search parameters, this initial list may be further significantly expanded to consider non-specific enzyme cleavage and post-translational modifications (PTMs) of amino acid residues. Given the complete list of peptides, for each MS/MS spectrum a two-step procedure is repeated. First, a set of candidates is selected, comprised of peptides with masses falling into a tolerance window around the mass of the parent ion. Next, a theoretical fragmentation mass spectrum is generated for each candidate peptide and compared with the experimental one. The candidate with the highest value of a scoring function is considered the best match and is assigned to the examined spectrum. With peptide sequences identified, a list of proteins present in the studied samples can be inferred. Numerous search engines, both commercial and free, have been developed over the last years to implement this generic scheme of protein identification (Perkins et al., 1999; Craig & Beavis, 2004; Cox et al., 2011; Kim & Pevzner, 2014).

Because of the huge number of candidate peptides scored against the input spectra, the database-aided interpretation of LC-MS/MS data is a computationally expensive and resource-demanding task. This is especially true when variable (i.e. potential) post-translational modifications are considered, as they cause a combinatorial growth of the search space. On the other hand, the coarse-grained nature of the problem makes it almost perfectly parallel. Thus, not surprisingly, several strategies have been proposed to speed up proteomic searches. Most of the popular protein identification systems are designed for multithreaded execution. Moreover, hardware-accelerated processing has been suggested to take advantage of the massively parallel nature of modern graphics processing units (GPUs) (Milloy, Faherty & Gerber, 2012). Large-scale computing architectures have also been employed, including clusters with worker nodes communicating using message-passing protocols, such as MPI (Duncan, Craig & Link, 2005; Bjornson et al., 2008). Unfortunately, none of these approaches are fully satisfactory: multithreading is inherently limited by the resources of a single machine, GPU computations can only accelerate the scoring phase of the algorithm, and the necessity to repeat the database digestion independently on each node of the cluster affects the scalability of MPI-based implementations.

More recently, distributed computing frameworks have been proposed to address the increasing complexity of proteomic analyses. Frameworks such as Apache Hadoop (Dean & Ghemawat, 2008) and Spark (Zaharia et al., 2010) provide an effective way to parallelize computational tasks across large heterogeneous clusters or cloud environments. They also facilitate the development of distributed applications by handling network communication, job scheduling, and failure recovery. Hadoop was first used in proteomics to create a simple distributed version of X!Tandem, a popular open-source tool for protein identification (Pratt et al., 2012). Afterwards, a more advanced search engine, called Hydra, was introduced by Lewis et al. (2012). The algorithm of Hydra is implemented following the MapReduce

programming paradigm and is designed to scale with both the number of input spectra and the size of the proteins database. Yet, its performance and flexibility are limited by the execution model of Hadoop, primarily developed and optimized for the processing of on-disk data.

Here, we introduce SparkMS, a novel distributed algorithm based on Apache Spark. This state-of-the-art framework considerably improves the restrictive MapReduce model of Hadoop by allowing in-memory caching of data and iterative operation. Spark was already employed in bioinformatic analyses (Guo et al., 2018) and utilized in proteomics for the unbiased search of PTMs in spectral libraries (Horlacher, Lisacek & Müller, 2016). In this paper, we present its application to the problem of database-aided peptide and protein identification.

The main idea behind the development of SparkMS was to create a high-performance algorithm capable of processing vast amounts of data provided by comprehensive MS-based proteomic studies. In this regard, it was essential to ensure high scalability resulting from both the parallelization of all the database search steps and the effective use of the resources of the distributed computer system. Achieving such a goal was possible by fully utilizing the Spark platform features and the appropriate design of the algorithm workflow, which also employs data structures and procedures that allow for the minimization of network transfers. At the same time, unlike in the case of Hydra, great emphasis was placed on the algorithm's flexibility and ensuring the possibility of easy adaptation of its operation to various experimental designs and different measuring instruments.

2. METHODS

The presented proteomic database search algorithm is specifically developed to be compatible with the distributed execution model of the Apache Spark framework. Spark uses a master/slave architecture, where the master node runs a driver program, which dispatches computational tasks to executors on worker nodes.

The primary data structure in Spark is the resilient distributed dataset (RDD), a collection of immutable objects or key-value pairs which can be processed in parallel. The RDDs are automatically divided into logical partitions, and a different executor may manage each partition on a separate cluster node. Spark offers two types of operations on RDDs: transformations and actions. Transformations create a new dataset from an existing one by applying some function to its records, while actions return the processing results to the driver.

SparkMS follows the above-described execution model by converting the list of input MS/MS spectra and the proteins database into RDDs and performing a set of succeeding parallel transformations. To balance the workload and limit transfers between worker nodes, a specialized partitioning scheme is used. Moreover, an interval tree is employed in the protein digestion step to reduce memory usage and accelerate the search of candidate peptides. The flowchart of the algorithm is presented in Figure 1, and its details are discussed below.

2.1. Input Data and Parameters

The input data for SparkMS consists of an MGF (Mascot Generic Format) file with experimental MS/MS spectra and a protein sequences database in FASTA format. An additional XML configuration file allows the user to specify various search parameters, including

the most important ones: the proteolytic enzyme, maximum mass deviation (MMD) of parent and fragment ions, peptide fragmentation rules, and the list of PTMs selected from the UniMod database (Creasy & Cottrell, 2004).

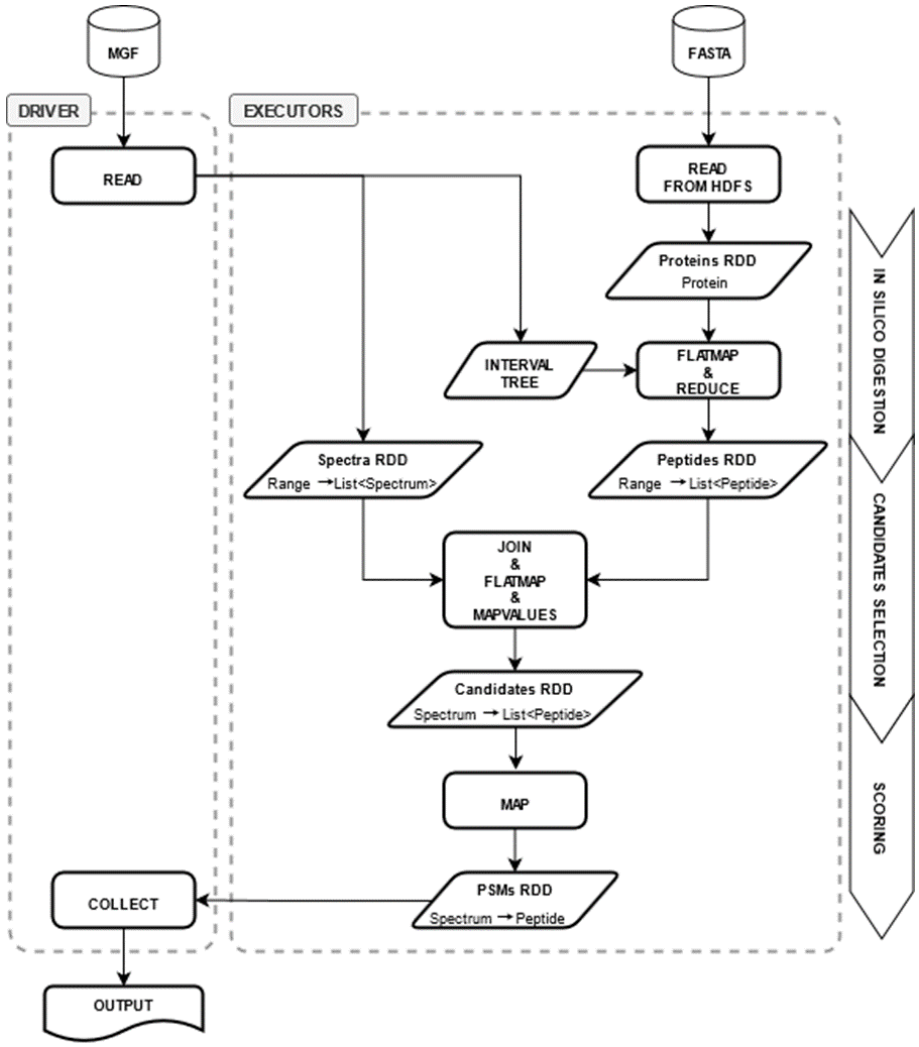

Fig. 1. Flowchart of SparkMS algorithm – the plot is divided into two parts representing sequential procedures performed on the master node (left frame) and operations executed in parallel on worker nodes (right frame) (on the right edge, the corresponding stages of the database identification process are presented; the notation *T→S* used in the description of the RDDs symbolizes *key→value* pairs with keys of type *T* and values of type *S*)

2.2. Creation of Resilient Distributed Datasets

Loading of the MGF input file takes place on the driver. Simultaneously the program creates an interval tree, i.e., a data structure that enables the efficient retrieval of intervals containing a given value. In our case, the tree stores the mass ranges of candidate peptides, calculated for each spectrum based on the parent ion mass and the user-defined MMD.

The tree is used to build a map of mass ranges (keys) and corresponding lists of experimental spectra (values), which is then parallelized to an RDD of pairs (depicted in Figure 1 as *Spectra RDD*). The interval tree itself is also provided to all executors as a broadcast variable and afterwards utilized in the *in silico* digestion step (see section 2.3).

The SparkMS implementation provides the ability to read the proteins database in FASTA format from both local or distributed filesystems. As a result, an RDD with protein records is created (*Proteins RDD* in Figure 1).

2.3. *In Silico* Protein Digestion

For each record in the proteins RDD, proteolytic peptides are generated according to the specificity of the selected enzyme and the list of considered PTMs. Isobaric modified variants of the same peptide are merged into single entries, as the exact locations of the PTMs are irrelevant for determining candidate sequences (location-specific variants will be generated only for candidate peptides before scoring – see section 2.4). To further reduce memory usage, all peptides are compared with the previously created interval tree, and only those found to fall within the mass range of at least one spectrum are stored.

The digestion step is implemented as a combination of two transformations: `flatMap` and `reduceByKey`. The first one maps proteins to their proteolytic peptides, while the purpose of the latter is to create an RDD of pairs with mass ranges as keys and aggregated lists of unique peptides as values (*Peptides RDD* in Figure 1). Both transformations subdivide the required computations among executors responsible for processing separate equal-sized partitions of the input proteins set.

2.4. Candidate Peptides Selection

In order to find candidate sequences, first, a `leftOuterJoin` is performed on the *Spectra RDD* and *Peptides RDD* using the mass range as a shared key. Next, a `flatMap` applied to the join result creates a new RDD of pairs (referenced as *Candidates RDD* in Figure 1), which assigns MS/MS spectra (keys) to lists of their candidate peptides (values). Finally, the lists of peptides are extended by a `mapValues` transformation to include sequence variants with all the possible PTM locations. The transformations are parallelized at the level of *spectrum→candidates* pairs, and a dedicated partitioner ensures even workload distribution among executors by equalizing the number of spectra in partitions. This partitioning scheme is also maintained in the scoring step of the algorithm.

2.5. Candidate Peptides Scoring

The scoring phase of the algorithm is realized by a single `map` transformation. The first task of the function applied in parallel to each entry of the *Candidates RDD* is to generate the theoretical spectra of candidate peptides following the fragmentation rules specified by the user. Next, the theoretical spectra are compared with the experimental one, and similarity scores are computed. The candidate with the highest score is assigned to the examined spectrum to form a peptide-spectrum match (PSM).

The spectra similarity is expressed in terms of a simple probabilistic score dependent on the number k of matches between the peaks of the experimental spectrum and the theoretical one (two peaks are deemed to be a match if the difference of their positions is less than the

allowed MMD of fragment ions). The score value is calculated as the probability of matching at least *k* out of the *n* theoretical peaks by pure chance, reported in logarithmic scale (Taus et al., 2011):

$$score = -10 \log_{10}[\sum_{i=k}^{n} \binom{n}{i} p^i (1-p)^{n-i}] \quad (1)$$

where: p – the probability of randomly matching a single experimental peak, estimated as:

$$p = \frac{Nd}{w} \quad (2)$$

where: N – the total number of measured peaks,
d – the fragment ions MMD,
w – the full mass range of the peaks in the experimental spectrum.

After scoring all spectra against their candidates, the resulting dataset (the *PSMs RDD* in Figure 1) is collected to the driver and saved in a human-readable text file.

3. RESULTS

The SparkMS algorithm has been implemented in the Java programming language and tested on a computer cluster. We have also implemented an alternative variant of the algorithm, which, to some extent, mimics the behaviour of the Hydra search engine (Lewis et al., 2012). This modified version (further denoted as "SparkMS (no IT)") does not use an interval tree to limit the number of peptides stored in memory after *in silico* digestion. Instead, the complete set of proteolytic peptides is preserved, divided into constant-width mass bins, and co-grouped by mass range with the input spectra to eventually form the lists of candidate sequences. Both implementations share the same source code of basic procedures (such as protein digestion, scoring function, etc.), thus they allow for an unbiased comparison of different approaches to database search on a common distributed computing platform. The two variants of SparkMS have been evaluated in regard to their protein identification performance, horizontal scalability, understood as the ability to efficiently use additional computational resources, and scalability with increasing task complexity (expressed in the number of scored candidate sequences).

3.1. Test Data and Settings

The computing infrastructure for the tests consisted of a Spark/HDFS cluster (Apache Spark version 2.3.0, Hadoop 2.9.0) composed of 6 workers and one master node connected with gigabit Ethernet. Each node was equipped with two 4-core AMD Opteron 2384 processors and 16 GB of RAM. The Spark cluster manager was configured to lunch two independent executors per node, assigning 4 cores and 6 GB of RAM to each executor. The master node was running the Spark driver process with 12 GB of RAM available.

Test data originated from a recently published study on the proteome composition of pancreatic cyst fluid (Paziewska et al., 2018). The dataset consisting of 715 972 high-resolution MS/MS spectra is available in the PRIDE repository (Vizcaíno et al., 2016) under the ID: PXD005248. The experimental spectra were searched against a database containing

173 843 target human proteins from the release 2020.06 of the UniProt/TrEMBL database (UniProt Consortium, 2019) and the same number of reversed decoy entries. Such an approach, commonly referred to as the target/decoy strategy, enables the estimation of the false discovery rate (FDR) of protein identification results (Käll et al., 2008). The search parameters were as follows: enzyme specificity – trypsin; maximum number of missed cleavages – 2; parent ions MMD – 10 ppm; fragment ions MMD – 0.01 Da; fixed PTMs – methylthiolation of C; variable PTMs – oxidation of M and acetylation of K (unless otherwise stated in the description of a particular test), and at most 3 modified sites per peptide were allowed.

For comparison purposes X!Tandem (version 2015.12.15.2) was used. The output files of both SparkMS and X!Tandem were post-processed with MScan, a software tool available at http://proteom.ibb.waw.pl/mscan.

3.2. Peptide and Protein Identification Performance

After searching against the TrEMBL database, SparkMS assigned sequences to 80 721 spectra (out of 715 972, 11.3% of the dataset) with an FDR equal to 0.01. The created peptide-spectrum matches (PSMs) corresponded to 3 548 unique peptides originating from 1 231 proteins, of which 923 were represented by at least two peptides. To ensure complete consistency, the sets of identified PSMs, peptides, and proteins were cross-checked between the two versions of the distributed algorithm and an additional single-threaded implementation. The results were also confronted with those obtained from X!Tandem, executed with corresponding parameters on the same input data. The comparison indicated a generally similar identification performance for both search engines. As it is presented in table 1, SparkMS created 0.4% fewer PSMs than X!Tandem, but simultaneously, it detected 0.8% more unique peptides and 3.4% more proteins. Noteworthy, we observed a significant overlap between the results of X!Tandem, and SparkMS, as 83.2% of the total number of peptides and 73.5% of proteins were common for the two search engines. Such a degree of commonality is typical for the comparison of different proteomic database-aided identification systems (Paulo, 2013).

Tab. 1. Comparison of SparkMS and X!Tandem in terms of the numbers of PSMs, peptides and proteins identified at an FDR threshold of 0.01.

Search engine	PSMs	Peptides	Proteins
X!Tandem	81071	3534	1189
SparkMS	80721	3548	1231

3.3. Horizontal Scalability

On a single 8-core machine, SparkMS completed the database search in 1 583 seconds, and it was 2.57 times faster than its modified version, which does not employ the interval tree (Figure 2). Moreover, it outperformed by a factor of 1.33 the X!Tandem search engine running on the same machine. With the adding of worker nodes, the execution time decreased, ultimately leading to a 4.81-fold speedup on the 6-node cluster versus a single machine. An analysis of Apache Spark runtime statistics indicated that the speedup was to some

degree limited by the relatively low network throughput of the test cluster. So, it is possible that the horizontal scalability could be improved by simply replacing the gigabit ethernet with a faster connection.

The two compared variants of SparkMS presented almost equal horizontal scalability, however, the version with the interval tree was on average 2.56 times faster. Since the numbers of protein records and scored peptides are equal in both cases, the acceleration is mostly due to a more effective candidate sequences selection. The interval tree also reduced the amount of data stored after *in silico* digestion (17.7% fewer peptides stored) and subsequently shuffled between the executors (data transfer reduced by 34.0%).

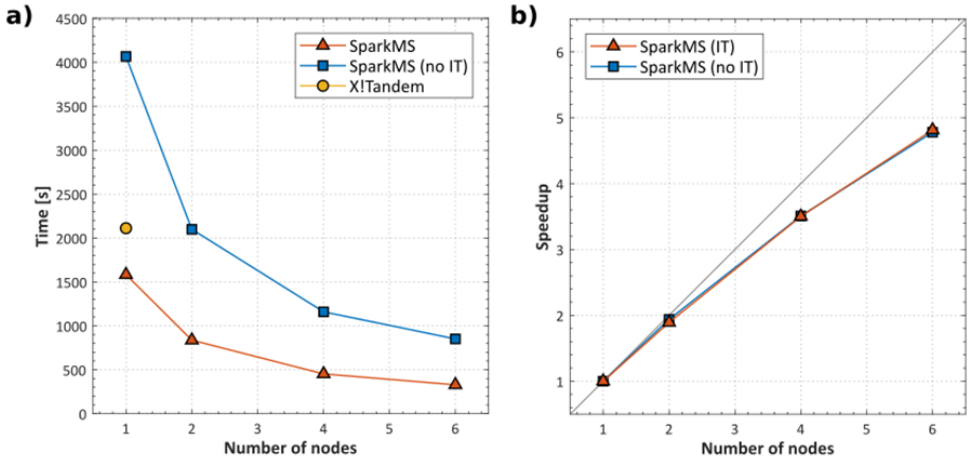

Fig. 2. Execution time in seconds (a) and speedup (b) with the number of worker nodes increasing from 1 to 6 (8 to 48 cores) – the plot presents the results of both SparkMS versions: with and without the interval tree (execution time of X!Tandem on a single node is also presented for reference; points are averaged over 5 test runs)

3.4. Scalability with Growing Task Complexity

To validate SparkMS against larger search spaces, we ran a series of tests with the number of variable PTMs increasing from none to 8 (apart from the two PTMs used in previous tests, six more were included: phosphorylation of S/T and Y, methylation of R and K, and dimethylation of R and K). This parameter greatly influences the number of possible candidate peptides, and therefore, it is well suited for verifying the ability of the algorithm to handle computationally intensive tasks. The test results are presented in Figure 3.

As expected, expanding the list of variable PTMs caused a highly nonlinear growth of task complexity. Consequently, the time needed to accomplish the database search with 8 PTMs reached 2 hr 48 min on a 48-core cluster. The speedup over a single 8-core node was 4.72, which is a value very close to the one observed in section 3.3. This indicates that the horizontal scalability of SparkMS remains unaffected even for high-complexity tasks. Notably, the relationship between the number of scored peptides and the search time was almost perfectly linear ($R^2 > 0.99$) for both SparkMS variants. As was the case earlier, the interval tree considerably accelerated the search (from 1.68 to 2.58 times). Separate tests revealed that similar conclusions also apply to the algorithm's scalability with the increasing number of input spectra.

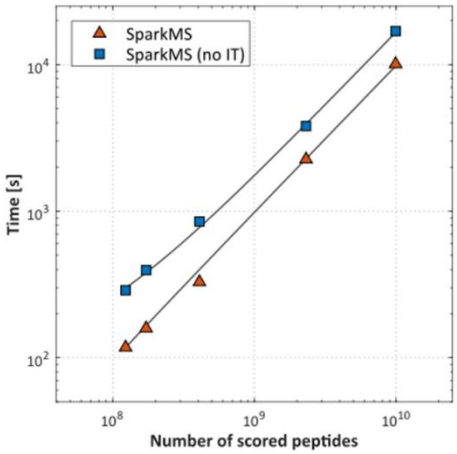

Fig. 3. Execution time on a cluster with 6 worker nodes (48 cores) as a function of task complexity, expressed in the number of scored candidate peptides (points are averaged over 5 test runs; grey lines represent linear regression fits)

4. DISCUSSION

The basic idea of the SparkMS algorithm is somewhat similar to the one used in Hydra, a previously presented search engine build on Hadoop. First and foremost, both solutions are designed to operate on clusters of heterogeneous hardware managed by distributed computing frameworks. Therefore, they inherit features such as horizontal scalability and fault tolerance. They also enable the parallelization of all stages of the protein identification process – this is a clear advantage over MPI-based or GPU-accelerated approaches.

However, despite certain similarities between the two search engines, there are also essential differences in both the algorithm design and the used programming framework. Hydra divides the search into two independent tasks, separated by disk write and read operations. In the first task, all the possible proteolytic peptides are generated, binned by mass value, and saved to a distributed filesystem. The second task is aimed at scoring the input spectra against the formerly stored peptides. Both steps are implemented as series of MapReduce operations with intermediate results serialized to disk. Such behaviour is consistent with the Hadoop workflow but is not necessarily optimal for proteomic searches.

In contrast to Hydra, SparkMS is prepared for in-memory operation, and it does not require any time-consuming disk access, aside from reading the input data and writing the results. The algorithm also does not rely upon a precalculated list of proteolytic peptides (which in the case of Hydra must be recreated each time the search parameters are changed) or any additional assumptions limiting its flexibility. In fact, its implementation is fully parameterized and can be easily adapted by the user to any specific experimental design or mass spectrometer. Moreover, the algorithm's performance and scalability benefit from the lower overheads of the Spark platform in respect to Hadoop. Further acceleration is achieved by using a custom partitioning scheme and an interval tree to select candidate peptides.

SparkMS was tested on a computer cluster against a large real-world proteomic dataset. On a single 8-core machine, SparkMS achieved an execution time comparable to X!Tandem, a standard multi-threaded search engine (notably, both programs also exhibited a similar

peptide and protein identification performance). However, the distributed algorithm provided an added value in the ability to efficiently utilize multiple worker nodes. Its horizontal scalability allowed to shorten the calculations approximately 4.8 times on a 6-node cluster, and the speedup did not deteriorate with increasing task complexity. Moreover, the observed execution times scaled linearly with the number of candidate peptides scored against the input spectra. Thus, it is possible to assume that SparkMS would accommodate even larger datasets/databases and more exhaustive search parameters. The test also clearly demonstrated the gain in speed and memory consumption resulting from employing an interval tree for candidate sequences selection, instead of using a straightforward join of mass-binned spectra and peptides, as proposed in Hydra.

The performed experiments confirmed the potential of the Spark-based algorithm to deal with proteomic searches of various sizes, including those involving the processing of vast amounts of data. However, it should be noted that the presented computational strategy also has some limitations. Specifically, in a distributed environment, the actual speedup is a function of task complexity, the number of worker nodes, and network throughput. For small inputs or restricted search parameters, the initialization overhead and the finite speed of data transfer are likely to limit the scalability, especially when the cluster size increases. Therefore, the distributed approach is best suited for computationally intensive jobs.

5. CONCLUSIONS

With constantly growing sizes of protein databases and the broader availability of fast and sensitive high-resolution spectrometers, the LC-MS/MS data processing is increasingly becoming a “big data” problem that requires an efficient and highly scalable computational strategy. To address this issue, we developed SparkMS, a new distributed algorithm for the database-aided peptide and proteins identification. The proposed algorithm takes full advantage of the Apache Spark framework to effectively parallelize all the stages of the identification process. Experimental results demonstrated that SparkMS scales with both the increasing task complexity and the number of worker nodes. Therefore, given a big enough cluster infrastructure, the algorithm is ready to perform fast and comprehensive proteomic searches, leading to a better insight into the biological problems under study.

Although the paper presents a fully functioning proteomic search engine, there is still room to improve the underlying algorithm. Its further development will primarily concern increasing the efficiency of using the cluster's computing resources. This will be achieved by introducing a more advanced data partitioning scheme in the scoring stage. The new partitioner will ensure equal numbers of candidate peptides (instead of spectra, as in the current version) in the partitions, allowing for shortened runtimes and increased scalability due to better load balancing between worker nodes.

Work is also underway to introduce an additional phase to the algorithm related to the statistical evaluation of peptide-spectra matches and to use machine learning to improve identification performance. The preliminary results of the proposed support vector machine demonstrated its ability to increase the number of correctly identified peptides at a given FDR threshold, albeit optimization is still required to exploit the full potential of the Apache Spark platform (Orzechowska & Rubel, 2021).

Finally, it is worth noting that an interesting direction of further research is the adaptation of SparkMS to the processing of data from experiments using mass spectrometry combined with cross-linking to study protein-protein interactions in complexes (Rappsilber, 2011). It is a problem of growing importance for proteomics and structural biology, the solution of which requires high computational effort, which makes it well suited to the distributed environment.

REFERENCES

Aebersold, R., & Mann, M. (2003). Mass spectrometry-based proteomics. *Nature*, *422*(6928), 198–207. https://doi.org/10.1038/nature01511

Bjornson, R. D., Carriero, N. J., Colangelo, C., Shifman, M., Cheung, K. H., Miller, P. L., & Williams, K. (2008). X!!Tandem, an improved method for running X!tandem in parallel on collections of commodity computers. *Journal of proteome research*, *7*(1), 293–299. https://doi.org/10.1021/pr0701198

Cox, J., Neuhauser, N., Michalski, A., Scheltema, R. A., Olsen, J. V., & Mann, M. (2011). Andromeda: a peptide search engine integrated into the MaxQuant environment. *Journal of proteome research*, *10*(4), 1794–1805. https://doi.org/10.1021/pr101065j

Craig, R., & Beavis, R. C. (2004). TANDEM: matching proteins with tandem mass spectra. *Bioinformatics (Oxford, England)*, *20*(9), 1466–1467. https://doi.org/10.1093/bioinformatics/bth092

Creasy, D. M., & Cottrell, J. S. (2004). Unimod: Protein modifications for mass spectrometry. *Proteomics*, *4*(6), 1534–1536. https://doi.org/10.1002/pmic.200300744

Dean, J., & Ghemawat, S. (2008). MapReduce: Simplified Data Processing on Large Clusters. *Communications of the ACM*, *51*(1), 107–113. https://doi.org/10.1145/1327452.1327492

Duncan, D. T., Craig, R., & Link, A. J. (2005). Parallel tandem: a program for parallel processing of tandem mass spectra using PVM or MPI and X!Tandem. *Journal of proteome research*, *4*(5), 1842–1847. https://doi.org/10.1021/pr050058i

Guo, R., Zhao, Y., Zou, Q., Fang, X., & Peng, S. (2018). Bioinformatics applications on Apache Spark. *GigaScience*, *7*(8), giy098. https://doi.org/10.1093/gigascience/giy098

Hernandez, P., Müller, M., & Appel, R. D. (2006). Automated protein identification by tandem mass spectrometry: issues and strategies. *Mass spectrometry reviews*, *25*(2), 235–254. https://doi.org/10.1002/mas.20068

Horlacher, O., Lisacek, F., & Müller, M. (2016). Mining Large Scale Tandem Mass Spectrometry Data for Protein Modifications Using Spectral Libraries. *Journal of proteome research*, *15*(3), 721–731. https://doi.org/10.1021/acs.jproteome.5b00877

Käll, L., Storey, J. D., MacCoss, M. J., & Noble, W. S. (2008). Assigning significance to peptides identified by tandem mass spectrometry using decoy databases. *Journal of proteome research*, *7*(1), 29–34. https://doi.org/10.1021/pr700600n

Kim, S., & Pevzner, P. A. (2014). MS-GF+ makes progress towards a universal database search tool for proteomics. *Nature communications*, *5*, 5277. https://doi.org/10.1038/ncomms6277

Lewis, S., Csordas, A., Killcoyne, S., Hermjakob, H., Hoopmann, M. R., Moritz, R. L., Deutsch, E. W., & Boyle, J. (2012). Hydra: a scalable proteomic search engine which utilizes the Hadoop distributed computing framework. *BMC bioinformatics*, *13*, 324. https://doi.org/10.1186/1471-2105-13-324

Milloy, J. A., Faherty, B. K., & Gerber, S. A. (2012). Tempest: GPU-CPU computing for high-throughput database spectral matching. *Journal of proteome research*, *11*(7), 3581–3591. https://doi.org/10.1021/pr300338p

Orzechowska, K., & Rubel, T. (2021). An SVM-based peptide identification algorithm integrated into a database search engine. *Proceedings of the XXII Polish Conference on Biocybernetics and Biomedical Engineering.*

Paulo, J. A. (2013). Practical and Efficient Searching in Proteomics: A Cross Engine Comparison. *WebmedCentral*, *4*(10), WMCPLS0052. https://doi.org/10.9754/journal.wplus.2013.0052

Paziewska, A., Polkowski, M., Rubel, T., Karczmarski, J., Wiechowska-Kozlowska, A., Dabrowska, M., Mikula, M., Dadlez, M., & Ostrowski, J. (2018). Mass Spectrometry-Based Comprehensive Analysis of Pancreatic Cyst Fluids. *BioMed research international*, *2018*, 7169595. https://doi.org/10.1155/2018/7169595

Perkins, D. N., Pappin, D. J., Creasy, D. M., & Cottrell, J. S. (1999). Probability-based protein identification by searching sequence databases using mass spectrometry data. *Electrophoresis*, *20*(18), 3551–3567. https://doi.org/10.1002/(SICI)1522-2683(19991201)20:18<3551::AID-ELPS3551>3.0.CO;2-2

Pratt, B., Howbert, J. J., Tasman, N. I., & Nilsson, E. J. (2012). MR-Tandem: parallel X!Tandem using Hadoop MapReduce on Amazon Web Services. *Bioinformatics (Oxford, England)*, *28*(1), 136–137. https://doi.org/10.1093/bioinformatics/btr615

Rappsilber, J. (2011). The beginning of a beautiful friendship: Cross-linking/mass spectrometry and modelling of proteins and multi-protein complexes. *Journal of Structural Biology*, *173*(3), 530–540. https://doi.org/10.1016/j.jsb.2010.10.014

Sadygov, R. G., Cociorva, D., & Yates, J. R., 3rd (2004). Large-scale database searching using tandem mass spectra: looking up the answer in the back of the book. Nature methods, 1(3), 195–202. https://doi.org/10.1038/nmeth725

Taus, T., Köcher, T., Pichler, P., Paschke, C., Schmidt, A., Henrich, C., & Mechtler, K. (2011). Universal and confident phosphorylation site localization using phosphoRS. *Journal of proteome research*, *10*(12), 5354–5362. https://doi.org/10.1021/pr200611n

UniProt Consortium. (2019). UniProt: a worldwide hub of protein knowledge. *Nucleic acids research*, *47*(D1), D506–D515. https://doi.org/10.1093/nar/gky1049

Vizcaíno, J. A., Csordas, A., Del-Toro, N., Dianes, J. A., Griss, J., Lavidas, I., Mayer, G., Perez-Riverol, Y., Reisinger, F., Ternent, T., Xu, Q. W., Wang, R., & Hermjakob, H. (2016). 2016 update of the PRIDE database and its related tools. *Nucleic acids research*, *44*(22), 11033. https://doi.org/10.1093/nar/gkw880

Zaharia, M., Chowdhury, M., Franklin, M. J., Shenker, S., & Stoica, I. (2010). Spark: Cluster Computing with Working Sets. *Proceedings of the 2nd USENIX conference on Hot topics in cloud computing* (*HotCloud'10*). USENIX Association.

Applied Computer Science, vol. 18, no. 2, pp. 28–42
doi: 10.35784/acs-2022-11

Submitted: 2022-04-08 | Revised: 2022-05-16 | Accepted: 2022-06-08

Keywords: image enhancement, SEM images, statistical approaches, contrast enhancement

Zaid ALSAYGH[*], *Zohair AL-AMEEN* [0000-0003-3630-2134]*

CONTRAST ENHANCEMENT OF SCANNING ELECTRON MICROSCOPY IMAGES USING A NONCOMPLEX MULTIPHASE ALGORITHM

Abstract

Microscopic technology has recently flourished, allowing unparalleled viewing of microscopic elements invisible to the normal eye. Still, the existence of unavoidable constraints led on many occasions to have low contrast scanning electron microscopic (SEM) images. Thus, a noncomplex multiphase (NM) algorithm is proposed in this study to provide better contrast for various SEM images. The developed algorithm contains the following stages: first, the intensities of the degraded image are modified using a two-step regularization procedure. Next, a gamma-corrected cumulative distribution function of the logarithmic uniform distribution approach is applied for contrast enhancement. Finally, an automated histogram expansion technique is used to redistribute the pixels of the image properly. The NM algorithm is applied to natural-contrast distorted SEM images, as well as its results are compared with six algorithms with different processing notions. To assess the quality of images, three modern metrics are utilized, in that each metric measures the quality based on unique aspects. Extensive appraisals revealed the adequate processing abilities of the NM algorithm, as it can process many images suitably and its performances outperformed many available contrast enhancement algorithms in different aspects.

1. INTRODUCTION

Microscopic technology has lately flourished, allowing to view of different microscopic elements that are invisible to the normal eye (Cocks, Taggart, Rind & White, 2018). Electron microscopes are deemed the most powerful and versatile tools for depicting the microstructures of various materials (Al-Ameen, 2018a). The capacity of a microscope to view small details has dramatically increased in recent years. The scanning electron microscope (SEM) can achieve resolutions of less than 0.4 nm (Vladár, Postek & Ming, 2009). In integrated circuits, biological cells, and other important applications, SEM is becoming increasingly demanded as vital information is frequently extracted from Such images (Feng, Ye & Pease, 2006). The SEM uses high energy with a concentrated beam of electrons to generate a variety of pulses that are used to display the examined object in the form of a digital image (Sutton et al., 2007).

[*] Department of Computer Science, College of Computer Science and Mathematics, University of Mosul, Nineveh, Iraq, zaidalobaidy1988@gmail.com, qizohair@uomosul.edu.iq

Normal humans can observe two items that are 0.2 mm at a distance without the need for magnifying lenses. Modern SEM devices, on the other hand, may achieve a resolution of 1 nm. The SEM on the other hand may enlarge objects to 300,000 times, which is much more than the standard simple microscope that can only enlarge objects to 1,500 times (Wighting, Lucking & Christmann, 2004). The SEM devices produce grayscale images that can be colorized using specific processes to make such images look more practical. Although the SEM devices have thrived, the produced images from such a device are still owning degradations, and one of the most common occurring degradations in SEM is the low-contrast effect (Ohta et al., 2012; Beekman et al., 2019; Sim, Ting, Leong & Tso, 2019; Bennet, Burr, Schmid & Hodoroaba, 2021).

The difference between the lightest and dimmest image regions is what defines the contrast, in that a high difference leads to better contrast and a low difference leads to poor contrast. As a result, the details of an image with high contrast are preserved better than the details in an image with poor contrast (Chen et al., 2018). The low contrast is an unfavorable artifact that decreases the visibility of the details and makes it difficult to extract useful information. Therefore, such an effect must be processed efficiently to produce an output image that owns better visibility and has no processing artifacts (Cakir, Kahraman, Cetin-Atalay & Cetin, 2018). Contrast enhancement (CE) is an approach that is used to improve the distribution of pixels in the image dynamic range. The fundamental goal of CE is to create an output image that is more lucid than its original version and does not include any processing artifacts (Pei, Zeng & Chang, 2004).

Various CE approaches have been presented in the past and among those approaches, the histogram equalization (HE)-based methods have been of high popularity (Hashemi, Kiani, Noroozi & Moghaddam, 2010). For SEM, various CE approaches have been introduced in the past years, and such approaches vary in their ideas. Thus, different approaches are reviewed in Section 2 of this article. Hence, a noncomplex multiphase algorithm is developed for the CE of SEM. Accordingly, it owns two key phases: Firstly, a two-step processing approach is implemented for intensity adjustment. Secondly, a gamma-corrected cumulative distribution function of the log-uniform distribution (GCCDFLUD) method is implemented to further enhance the image. Finally, an automated histogram expansion method is utilized to reallocate the pixels to the full image interval.

The assessment of the proposed algorithm is done by applying it to different real contrast distorted SEM images. Furthermore, it is appraised against different approaches and the accurateness of the outputs is considered along with the processing speed. From the results, the proposed algorithm provided satisfactory performance as it performed the best in many aspects. Finally, the organization of this study goes as follows: Section 2 contains a review of the germane methods; Section 3 includes a full description of the developed algorithm; Section 4 describes the experimentations, comparisons, and results, along with their discussions; Section 5 includes the important conclusions.

2. RELATED WORK

This part reviews different studies related to improving the contrast of SEM images to deliver a clear grasp of the formerly utilized methodologies in this field. The main aim is to highlight the previously used concepts and determine their advantages and disadvantages

so that when developing the proposed algorithm, a wide knowledge of processing concepts would be known so that the development process becomes easier. Moreover, the advantages and disadvantages are considered, in that the advantages are properly exploited, and the disadvantages are carefully avoided. In (Sengee, Sengee & Choi, 2010), a two-phase approach was proposed, in which the large histogram bins that cause the washout artifacts are divided into sub-bins using a neighborhood-based process, in which the adjacent information is arranged accordingly. In the second phase, the processed histogram is separated into two smaller histograms depending on the histogram average value and these two histograms are equalized independently using a refined HE procedure. In (Ma & Han, 2014), a fusion-based algorithm was introduced, which begins by implementing a gradient transform to attain the edge information. Next, the Laplace of Gaussian (LoG) and the median filters are applied to the input image to get the filtered high-frequency information. After that, the image low-frequency components are processed by the contrast limited adaptive histogram equalization (CLAHE) technique. The outputs of the aforesaid three steps are fused to get the output image.

In addition, a hybrid technique was presented by (Lal & Chandra, 2014), in that it starts by applying a modified sigmoid function to modify the image intensities. Then, the outcome is further processed by the CLAHE technique to get the output image. Moreover, a spatial entropy-based algorithm is introduced by (Celik, 2014), in that it computes the spatial entropy of pixels by using the spatial distribution feature of image pixels. Next, entropy is used along with specific statistical measures to redistribute the image intensities and obtain the output. Likewise, a histogram sub-blocking-based algorithm is developed by (Sim, Teh, Tey & Kho, 2016), which starts by normalizing the input image to get its correct confined information. Then, the normalized image is broken into different sub-blocks and each sub-block is enhanced using a generalized HE technique. Using the output, the mid-nodes are computed and then a piecewise equalization approach is applied. Finally, a convolution procedure is implemented to mix the processed sub-blocks and get the output of the algorithm.

Furthermore, a quad HE-based approach is presented by (Shukri, Sim & Leong, 2016), in that it separates the input into two sub-histograms, in that they are separated again into quad-histograms. Then, the four histograms are considered and normalized using a specific probability density function. Finally, a remapping and equalization procedure is implemented depending on a distinct cumulative distribution function to get the output image. Moreover, an improved contrast equalization method was introduced by (Al-Ameen, 2018a), in that it includes two key stages. The first phase includes two-step image intensity rescale procedures that are used to modify the image intensities. The second phase includes two-step processing and remapping procedures that are used to adjust the contrast and remap the intensities to the full range.

In addition, a CLAHE-sigmoid-based algorithm was presented by (Arya, Sharma & Arya, 2019), in that it begins by implementing a modified sigmoid function on the input. Then, a CLAHE approach is implemented depending on the output of the previous step. The output is finally processed by the modified sigmoid function again to get the output image. Lastly, a multi-scale top-hat-based algorithm was proposed by (Mello-Román et al., 2021), in that it initially extracts different bright and dark features of the input image by utilizing the top-hat procedure. Next, the dark and bright scale variations are determined using a specified method. After that, a separate summation of the dark and bright scale variations is obtained.

The last step includes the adjustment of the bright and dark elements, in that the adjusted bright elements are added to the image and the adjusted dark elements are subtracted from the image to get the output.

From the studied methods, different ideas were utilized in the past to process the contrast and obtain satisfactory results. Table 1 describes the examined research articles in chronological sequence, including the authors, years, methodology, difficulty, benefits, and drawbacks. As noticed, the histogram-based methods are the most used. The standard version of histogram equalization is known to deliver an unnatural appearance with brightness amplification. The improved versions of histogram equalization may also have these artifacts but with less effect. Moreover, they may also involve excessive computations to provide the output. As for the statistical-based approaches, they utilize mediocre-intricacy computations making them somewhat rapid in processing the given images. However, insufficient enhancement abilities and the presence of artifacts may be introduced. Moreover, not all the reviewed methods were successful in delivering acceptable quality results as the contrast may be insufficient, brightness amplification may happen, and some artifacts may appear more distinctly. This is deemed undesirable as efficient processing without generating visual flaws is needed. Furthermore, the SEM images are obtained with high resolution and rapid processing is also needed for such images. Hence, providing a plain-structure algorithm that can produce acceptable results with no flaws is highly needed.

Tab. 1. A synopsis of the literature review.

No.	Author & Year	Concept	Intricacy	Pros	Cons
1.	(Sengee et al., 2010)	Bi-histogram equalization	Moderate	Preserve the brightness	Some results own a hazy look
2.	(Ma & Han, 2014)	A mix of statistical, morphological, and image processing operations	High	Increase the contrast and acutance	Unnatural contrast
3.	(Lal & Chandra, 2014)	Sigmoid function with adaptive histogram equalization	High	Good performance in the dark image regions	Many computations
4.	(Celik, 2014)	Spatial entropy	Low	Non-complex method	Does not provide enough enhancement
5.	(Sim et al., 2016)	Sub-blocking multiple peak histogram equalization	Moderate	Makes the dark regions more visible	Brightness amplification
6.	(Shukri et al., 2016)	Minimum Mean Brightness error Bi-histogram equalization	Low	Provides a noticeable CE	Provides unnatural look
7.	(Al-Ameen, 2018a)	Contrast equalization	Low	Non-complex method	Needs further improvements
8.	(Arya et al., 2019)	Modified sigmoid function with limited histogram equalization	High	Good CE	Many computations
9.	(Mello-Román et al., 2021)	Multiscale top-hat transform	High	Balanced CE	Complex method

3. PROPOSED ALGORITHM

This algorithm is created based on the notion that few computations are required to generate satisfactory results, in that it should produce the filter images rapidly with no processing artifacts. This algorithm employs a mix of statistical and image filtering methods in its processing concept. Its concept is as follows: First, a two-stage adjustment procedure is implemented to modify the intensities. Then, a gamma-corrected cumulative distribution function of the log-uniform distribution (GCCDFLUD) approach is implemented to further enhance the image. Finally, an automated histogram expansion approach is used to redistribute the pixels to the full image interval. To better represent the proposed algorithm, the diagram given in Figure 1 explains the steps concisely.

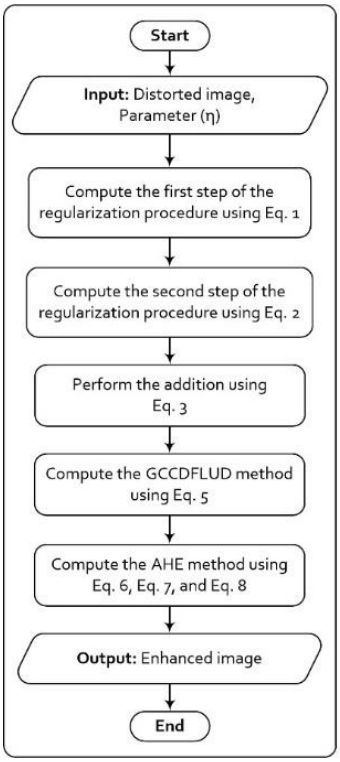

Fig. 1. Diagram of the proposed algorithm.

Explaining the proposed noncomplex multiphase (NM) algorithm in detail, the two-stage adjustment procedure is initially used to modify the poor intensities in the image in a non-linear way, better rescale such intensities, and restrain the extreme values. The two-step regularization procedure can be computed using these equations (Al-Ameen, 2018a):

$$W_{(i,j)} = \frac{O_{(i,j)}}{\left(\text{mean}\left(\left| O_{(i',j')} \right|^{\eta} \right) \right)^{1/\eta}} \tag{1}$$

$$M_{(i,j)} = \frac{W_{(i,j)}}{\left(\text{mean}\left(\min\left(\eta, \left| W_{(i',j')} \right| \right)^{\eta} \right) \right)^{1/\eta}} \tag{2}$$

where i and j are image coordinates, $W_{(i,j)}$ is the output of the first step, $O_{(i,j)}$ is a given input image, $O_{(i',j')}$ is the transpose of $O_{(i,j)}$, $M_{(i,j)}$ is the output of the first step, $W_{(i',j')}$ is the transpose of $W_{(i,j)}$, *mean* is the average, *min* is the lowest value, η is an enhancement parameter, in that it should be ($\eta > 0$), as a higher value leads to more enhancement. Next, the values of $M_{(i,j)}$ are increased by a small value τ to avoid getting the values of zero, in that the log is computed for the image in an upcoming step, and adding the value of τ helps to avoid computing the log of zero which is infinity. Here, $\tau = 0.1$, and the addition is done using the following equation:

$$T_{(i,j)} = M_{(i,j)} + \tau \tag{3}$$

Next, a gamma-corrected cumulative distribution function of the log-uniform distribution method is applied to further modify the image intensities and control the enhancement process as well. The log-uniform distribution is a statistical approach that is used to distribute values in a curvy non-linear way (Hamming, 1970). In image processing, it is proven that curvy transforms can be used to process the intensity of an image (El Malali et al., 2020). Thus, it is used and modified in this study to process the images as a vital stage. The original cumulative distribution function of the log-uniform distribution can be computed as follows (Hamming, 1970):

$$L_{(i,j)} = \frac{\log\left(T_{(i,j)}\right) - \log\left(y\right)}{\log\left(z\right) - \log\left(y\right)} \tag{4}$$

where, y is the lowest value in $T_{(i,j)}$, while z is the highest value in $T_{(i,j)}$. the above equation is further modified to control the amount of enhancement. The modified version of the above equation can be computed as follows:

$$Q_{(i,j)} = \left(\frac{\log\left(T_{(i,j)}\right) - \log\left(y\right)}{\log\left(z\right) - \log\left(y\right)} \right)^{\eta} \tag{5}$$

where, $Q_{(i,j)}$ is the output of the GCCDFLUD method. At this point, the image intensities are redistributed in a curvy way and are not distributed to the full range. Hence, an automated histogram expansion (AHE) method is implemented to well-distribute the pixels to the full image range. The AHE method can be computed as follows (Al-Ameen, 2020):

$$E_{(i,j)} = \kappa \cdot Q_{(i,j)} - \omega \tag{6}$$

$$\kappa = \frac{1}{\max\left(Q_{(i,j)}\right) - \min\left(Q_{(i,j)}\right)} \tag{7}$$

$$\omega = \frac{\min\left(Q_{(i,j)}\right)}{\max\left(Q_{(i,j)}\right) - \min\left(Q_{(i,j)}\right)} \tag{8}$$

where κ and ω are the extension parameters, $E_{(i,j)}$ is the final output of the proposed algorithm, and *max* represents the highest value.

4. RESULTS AND DISCUSSION

In this segment, the outcomes of comparisons, experiments, and related remarks are presented to analyze and demonstrate the true processing capabilities of the developed NM algorithm with a dataset of various real low-contrast SEM images. The dataset of this study was collected from different internet websites, in that the images are made available freely online. From these websites, almost 200 images were collected, in that these images are grayscale, and their sizes vary where the smallest has the size of 500×500 and the largest have the size of 3000×3000. The first website is http://www.dartmouth.edu, which includes different raw SEM images which are available freely online. The second website is https://www.ualberta.ca, which also includes different high-resolution SEM images. The third source of SEM images is from the consistence website, which can be accessed at https://www.consistence.nl/gallery/.

From this website, different unprocessed images were collected that own different sizes and are beneficial for this study. The fourth and final source of images is particle technology, which can be accessed at https://www.particletechlabs.com. The collected images are sorted, numbered, and in some cases cropped to be properly utilized. To truly measure the filtering abilities of the NM algorithm, a comparison is made with different algorithms namely, recursive mean-separate histogram equalization (RMSHE) (Chen & Ramli, 2003), dynamic histogram equalization (DHE) (Abdullah-Al-Wadud et al., 2007), adaptively increasing the value of histogram equalization (AIVHE) (Lu, Hsu & Wang, 2009), fuzzy-contextual contrast enhancement (FCCE) (Parihar, Verma & Khanna, 2017), swift algorithm (SWIFT) (Al-Ameen, 2018b), and improved contrast equalization (ICE) (Al-Ameen, 2018a). The comparison outcomes are evaluated using three no-reference quality evaluation methods, in that each metric detects the quality of the assessed images using special traits.

The used metrics are visual contrast measure (VCM) (Jang et al., 2011), blind pseudo-reference image (BPRI) (Min et al., 2017), and blind reference-less image spatial quality evaluator (BRISQUE) (Mittal, Moorthy & Bovik, 2012). The VCM is a metric that utilizes local statistical methods to measure the visual contrast in an image. The smaller output of VCM indicates better visual contrast. Moreover, the BPRI is a metric that utilizes a pseudo-reference approach with the image structural information to determine the naturalness. The smaller output of BPRI indicates better naturalness. In addition, the BRISQUE metrics

utilize a set of statistical measures to measure the quality of the apparent luminance and contrast. The smaller output of BRISQUE indicates better visual luminance and contrast. The computer used in this study has the specifications of an intel core I3-2328M 2.20 GHz processor and 4 GB of memory. MATLAB 2018a is the programming environment that is used for developing the algorithm, running the comparison algorithms, and the image evaluation methods. Figures 2 to 4 demonstrate different empirical results of the proposed algorithm. Figures 5 to 8 illustrate the comparison outcomes. Tables 2 to 5 represent the recorded image evaluation scores and runtimes. Figures 9 to 12 depict the average performances of Tables 2 to 5 as graphical charts. From Figure 2 to Figure 4, it is noticed that the outcomes of the NM algorithm are of acceptable visual quality, as they own improved contrast, preserved brightness, and no obvious processing errors, and they appear more credible to the viewer. Accordingly, when comparing the unprocessed image with its processed version, it seems as if a coat of mist has been diminished.

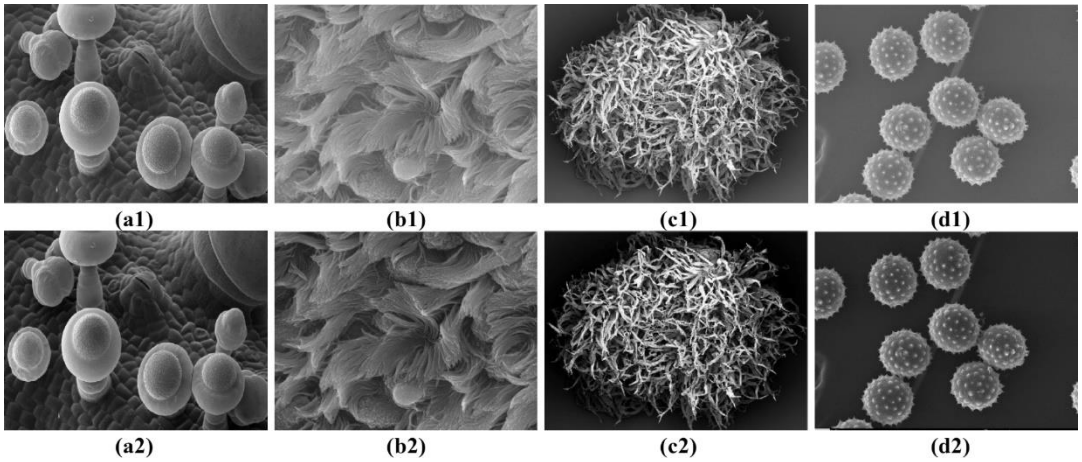

Fig. 2. The outcomes of the developed NM algorithm – (a1–d1) real contrast-distorted images, (a2–d2) results of the NM algorithm with η = 3.9, 4.9, 5, and 5.3, respectively

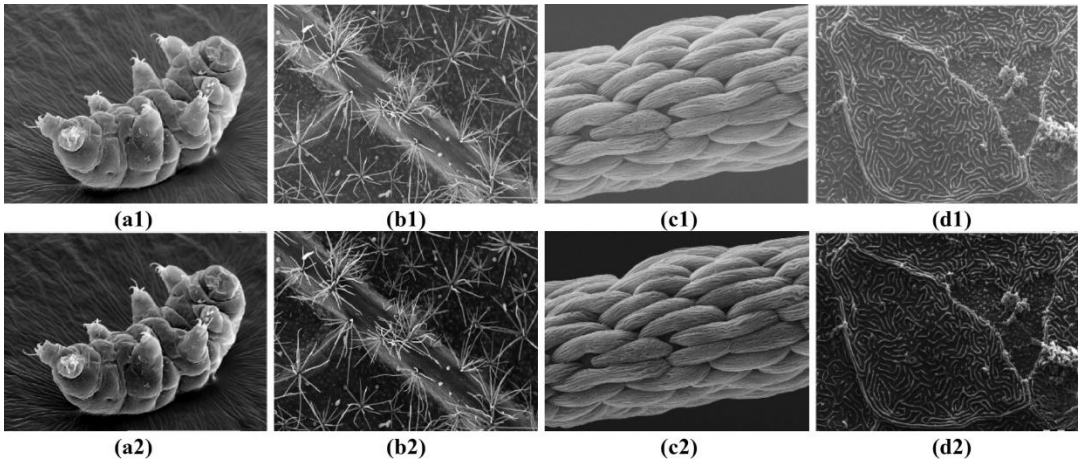

Fig. 3. The outcomes of the developed NM algorithm – (a1–d1) real contrast-distorted images, (a2–d2) results of the NM algorithm with η = 4.5, 5.2, 5.3, and 6.5, respectively

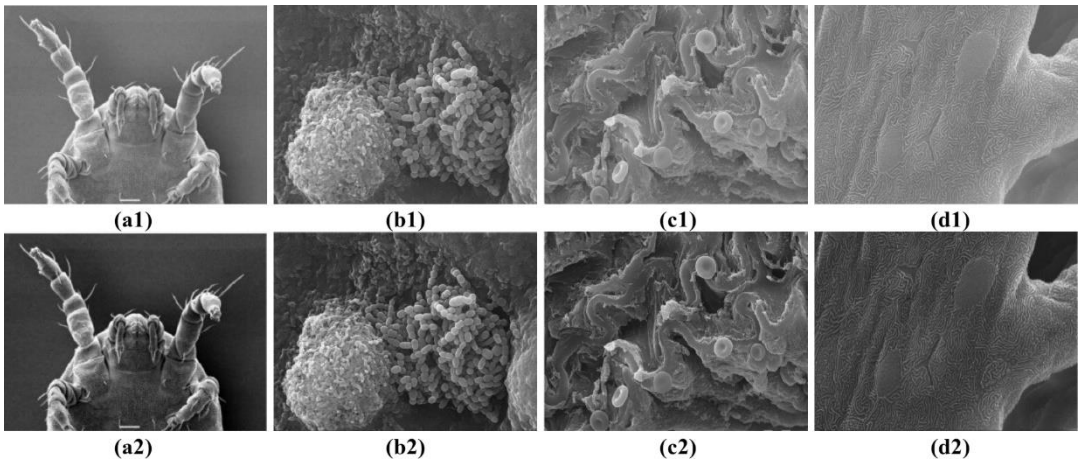

Fig. 4. The outcomes of the developed NM algorithm – (a1–d1) real contrast-distorted images, (a2–d2) results of the NM algorithm with η = 2.4, 3.9, 4.9, and 5.9, respectively

The details stood out better and the images became visually pleasing. Likewise, the NM algorithm showed promising performances as it was successful in processing many images obtained from different sources. The NM algorithm depends on the value of η, in that if it is properly chosen by the operator, the quality of the output would be desirable. From Figure 5 to Figure 12 and Table 2 to Table 5, it is spotted that dissimilar outcomes are obtained, as different algorithms in concept were implemented with numerous SEM images. The FCCE algorithm provided good contrast but amplified the brightness in different regions and darkened other regions making the image appear with an unusual look. That's why it scored low in all three metrics and was the slowest method. In addition, the SWIFT algorithm delivered a balanced performance concerning brightness and contrast, as the contrast is adjusted, and the brightness is slightly increased. Yet, it did not reach the scores of the proposed NM as it scored high in all three metrics with a slight difference from the NM algorithm. Yet, it ranked the 6th fastest method.

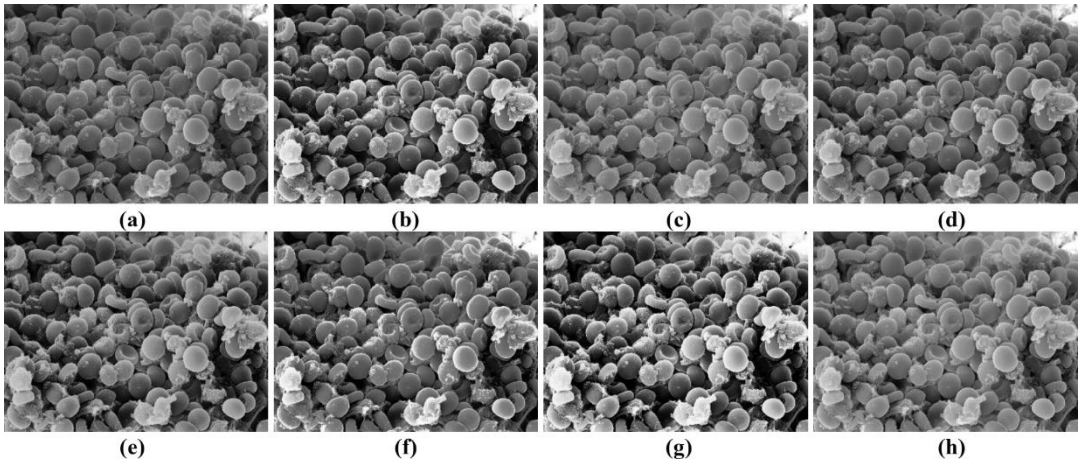

Fig. 5. The comparison outcomes (Batch -1-) – (a) real contrast-distorted SEM image, images (b–h) are processed by: (b) FCCE, (c) SWIFT, (d) ICE, (e) AIVHE, (f) RMSHE, (g) DHE, and (h) proposed NM

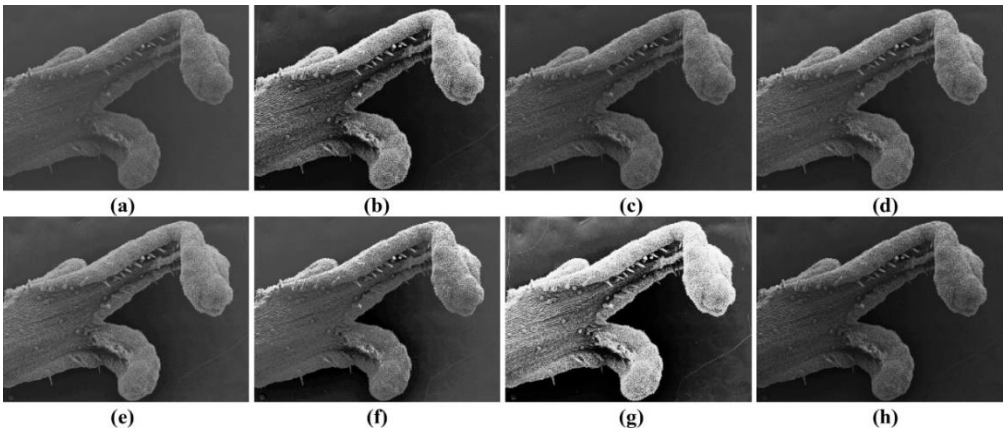

Fig. 6. The comparison outcomes (Batch -2-) – (a) real contrast-distorted SEM image, images (b–h) are processed by: (b) FCCE, (c) SWIFT, (d) ICE, (e) AIVHE, (f) RMSHE, (g) DHE, and (h) proposed NM

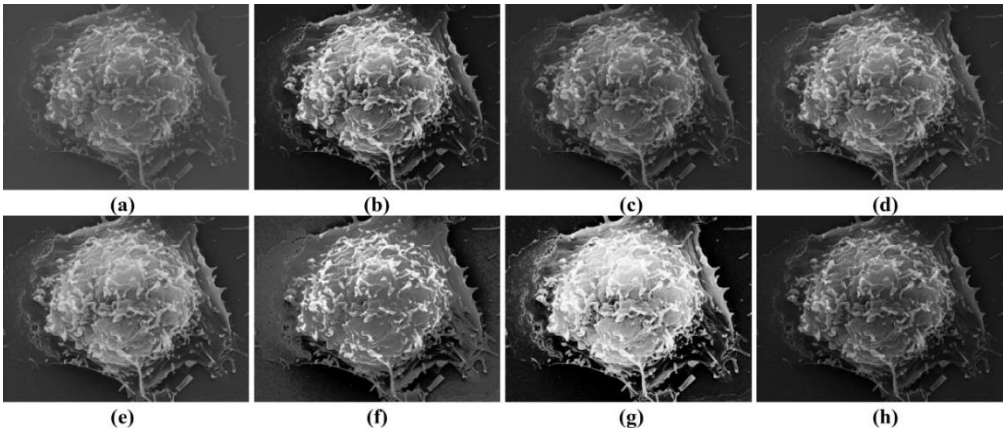

Fig. 7. The comparison outcomes (Batch -3-) – (a) real contrast-distorted SEM image, images (b–h) are processed by: (b) FCCE, (c) SWIFT, (d) ICE, (e) AIVHE, (f) RMSHE, (g) DHE, and (h) proposed NM

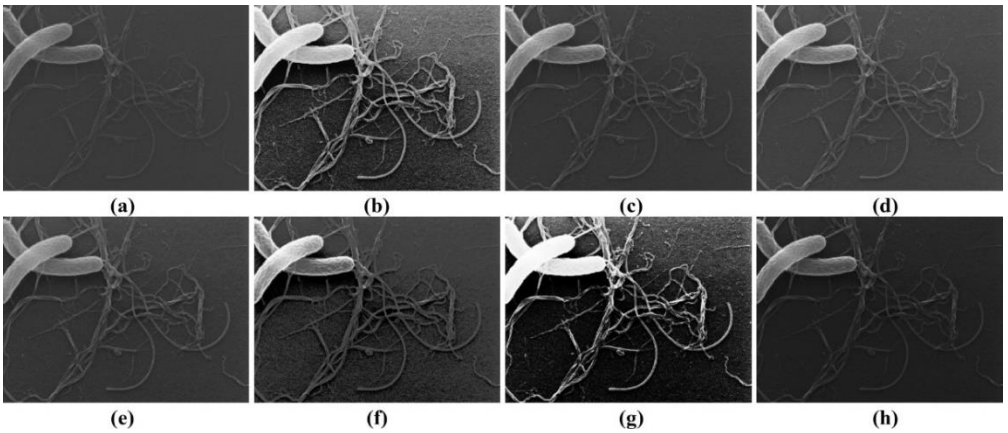

Fig. 8. The comparison outcomes (Batch -4-) – (a) real contrast-distorted SEM image, images (b–h) are processed by: (b) FCCE, (c) SWIFT, (d) ICE, (e) AIVHE, (f) RMSHE, (g) DHE, and (h) proposed NM

Moreover, the ICE algorithm delivered a reasonable performance as well but with marginally greater brightness than SWIFT with a regulated contrast, as it scored above moderate in all three metrics and was ranked the 3rd fastest method. Furthermore, the AIVHE algorithm delivered a somewhat sensible performance, with more need for contrast enhancement and brightness adjustment. Therefore, it scored moderately in all three metrics and was ranked the 5th fastest method.

Tab. 2. The recorded accuracies and their averages by the BPRI metric

Methods	Fig. 5	Fig. 6	Fig. 7	Fig. 8	Average
FCCE	0.0133	0.0164	0.0109	0.0364	0.01925
SWIFT	0.0096	-1.05E-04	0.0101	0.019	0.009649
ICE	0.0115	0.003	0.0117	0.0228	0.01225
AIVHE	0.0092	0.0099	0.0116	0.0251	0.01395
RMSHE	0.0083	0.0174	0.0108	0.0278	0.016075
DHE	0.009	0.0272	0.0141	0.0347	0.02125
Proposed NM	0.0123	-0.0049	0.0071	0.0179	**0.0081**

Tab. 3. The recorded accuracies and their averages by the BRISQUE metric

Methods	Fig. 5	Fig. 6	Fig. 7	Fig. 8	Average
FCCE	0.3385	40.1115	15.2681	41.2206	24.234675
SWIFT	-0.5849	28.5376	10.0693	36.4228	18.6112
ICE	0.4441	29.9195	10.3777	36.6058	19.336775
AIVHE	1.2809	33.1953	15.4099	40.0946	22.495175
RMSHE	0.2925	35.1319	25.4102	37.0675	24.475525
DHE	2.4419	47.1025	20.8524	45.413	28.95245
Proposed NM	-0.033	29.4091	8.9988	35.9838	**18.589675**

Tab. 4. The recorded accuracies and their averages by the VCM metric

Methods	Fig. 5	Fig. 6	Fig. 7	Fig. 8	Average
FCCE	1944.6	1.97E+03	1.44E+03	1.61E+03	1741.825
SWIFT	1.23E+03	807.3552	762.6877	338.4481	784.79775
ICE	1.25E+03	1.02E+03	968.6738	483.8228	931.37415
AIVHE	1.50E+03	1.11E+03	1.08E+03	436.2752	1032.1438
RMSHE	1.83E+03	1.44E+03	1.44E+03	721.4281	1357.107025
DHE	2.33E+03	3.02E+03	1.90E+03	1.52E+03	2190.00
Proposed NM	1346.3	787.9635	732.6598	255.0645	**780.49695**

Tab. 5. The application times and their averages (in seconds) for the comparison algorithms

Methods	Fig. 5	Fig. 6	Fig. 7	Fig. 8	Average
FCCE	0.789711	0.700735	0.604065	0.541752	0.65906575
SWIFT	0.197413	0.505441	0.344469	0.21442	0.31543575
ICE	0.100958	0.12412	0.106676	0.110124	0.1104695
AIVHE	0.101407	0.084859	0.32177	0.078892	0.146732
RMSHE	0.097669	0.094901	0.117599	0.087891	0.099515
DHE	0.102309	0.158808	0.12121	0.111865	0.123548
Proposed NM	0.097171	0.082195	0.087944	0.076719	**0.086005**

What is more, the RMSHE algorithm delivered an undesirable performance as it introduced brightness amplification and unusual contrast to the filtered images. The brightness in some areas appears massively amplified and the contrast looks unnatural with some processing artifacts. That is why it scored below moderate in all three metrics but was the 2nd fastest method. As for the DHE algorithm, it massively increased the brightness and delivered uncommon contrast. The overall look of the image is ruined, and many details were lost due to brightness amplification and the extreme darkening that happens in some areas. Therefore, it scored the lowest in all three metrics and was ranked the 4th fastest method. As for the proposed NM algorithm, it showed a clear superiority in performance over the comparison algorithms as its outcomes own balanced contrast, preserved brightness, and an overall acceptable appearance, in addition to being the fastest in runtimes. This is a noteworthy achievement as its structure is simple, yet it was able to perform better than many existing algorithms. Despite the above-mentioned primary advantages, it has one disadvantage being parameter η must be determined manually. In future work, a suitable optimization method can be utilized to automatically assess the value of η.

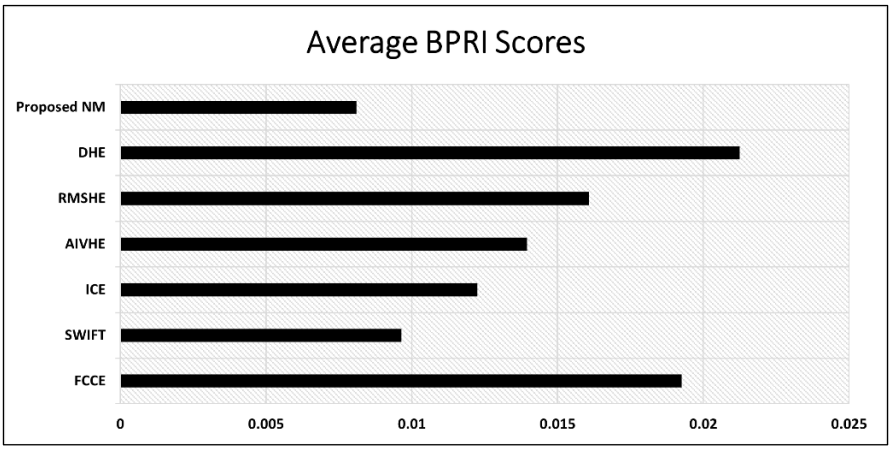

Fig. 9. The average BPRI scores

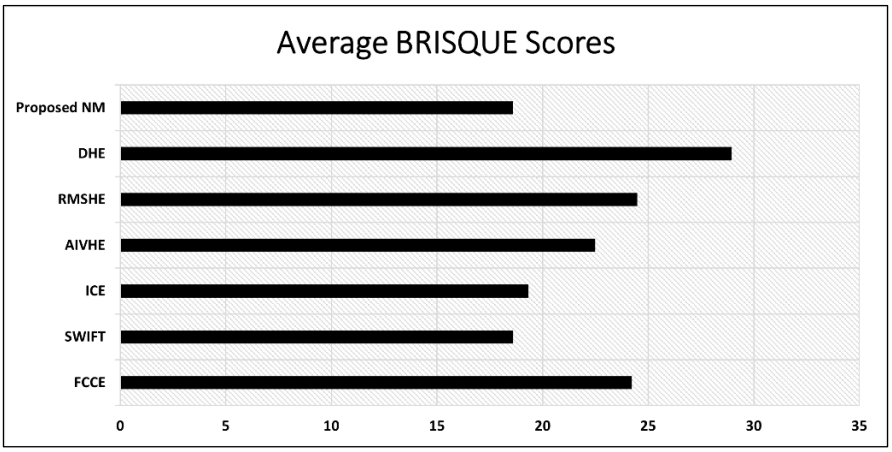

Fig. 10. The average BRISQUE scores

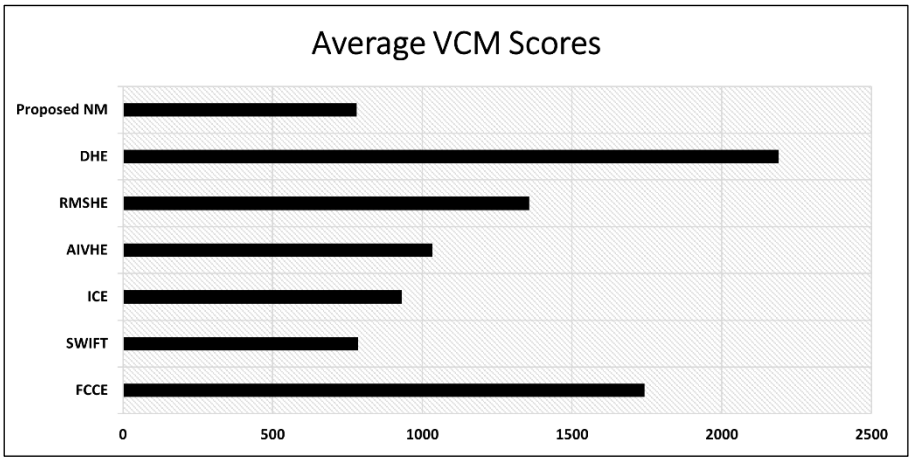

Fig. 11. The average VCM scores

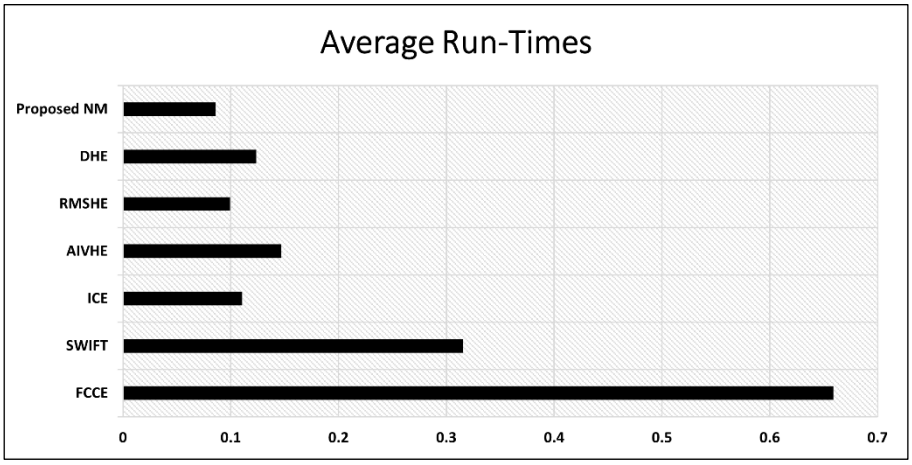

Fig. 12. The average run times

5. CONCLUSION

A simple-structure algorithm is presented in this paper to increase the observed contrast. In the proposed algorithm, a two-step regularization procedure is initially implemented to non-linearly modify the intensities. Then, a GCCDFLUD approach is implemented to further enhance the image and suppress high pixel values. Finally, an automated histogram expansion method is used to redistribute the pixels to the full image interval. Different real-contrast distorted images, evaluation methods, and comparison algorithms were utilized in this study for efficiency evaluations. The obtained results by the proposed algorithm have acceptable quality and surpassed the comparative algorithms in dissimilar facets as the attained results became more visually appealing, looked natural and it did not introduce any unnatural appearance or undesirable effects. Moreover, The NM algorithm outperformed the comparison methods in terms of runtimes, visual contrast, apparent luminance, and natural-ness as indicated by the utilized VCM, BPRI, BRISQUE metrics, and processor time.

The outcomes of this study are significant because a noncomplex algorithm was able to well-process different SEM images and avoid the drawbacks of different more advanced algorithms. As for future works, the NM algorithm may be further modified by using some specialized statistical approaches to be utilized with other image datasets that are valuable in different scientific applications. Likewise, it can be made entirely automated by using specialized artificial intelligence techniques.

Funding

This research did not receive any funding.

Conflicts of Interest

The authors declare that we don't have any conflict of interest regarding this study.

REFERENCES

Abdullah-Al-Wadud, M., Kabir, M. H., Dewan, M. A. A., & Chae, O. (2007). A dynamic histogram equalization for image contrast enhancement. *IEEE Transactions on Consumer Electronics*, *53*(2), 593–600. http://doi.org/10.1109/TCE.2007.381734

Al-Ameen, Z. (2018a). An improved contrast equalization technique for contrast enhancement in scanning electron microscopy images. *Microscopy Research and Technique*, *81*(10), 1132–1142. https://doi.org/10.1002/jemt.23100

Al-Ameen, Z. (2018b). Expeditious contrast enhancement for grayscale images using a new swift algorithm. *Statistics, Optimization & Information Computing*, *6*(4), 577–587. https://doi.org/10.19139/soic.v6i4.436

Al-Ameen, Z. (2020). Satellite image enhancement using an ameliorated balance contrast enhancement technique. *Traitement du Signal*, *37*(2), 245–254. https://doi.org/10.18280/ts.370210

Arya, V., Sharma, V., & Arya, G. (2019). An efficient adaptive algorithm for electron microscopic image enhancement and feature extraction. *International Journal of Computer Vision and Image Processing*, *9*(1), 1–16. https://doi.org/10.4018/IJCVIP.2019010101

Beekman, P., Enciso-Martinez, A., Rho, H. S., Pujari, S. P., Lenferink, A., Zuilhof, H., Terstappen, L.W. M. M., Otto, C., & Le Gac, S. (2019). Immuno-capture of extracellular vesicles for individual multi-modal characterization using AFM, SEM and Raman spectroscopy. *Lab on a Chip*, *19*(15), 2526–2536. https://doi.org/10.1039/C9LC00081J

Bennet, F., Burr, L., Schmid, D., & Hodoroaba, V. D. (2021). Towards a method for quantitative evaluation of nanoparticle from suspensions via microarray printing and SEM analysis. *Journal of Physics: Conference Series*, *1953*(1), 012002.

Cakir, S., Kahraman, D. C., Cetin-Atalay, R., & Cetin, A. E. (2018). Contrast enhancement of microscopy images using image phase information. *IEEE Access*, *6*, 3839–3850. https://doi.org/10.1109/access.2018.2796646

Celik, T. (2014). Spatial entropy-based global and local image contrast enhancement. *IEEE Transactions on Image Processing*, *23*(12), 5298-5308. https://doi.org/10.1109/TIP.2014.2364537

Chen, J., Yu, W., Tian, J., Chen, L., & Zhou, Z. (2018). Image contrast enhancement using an artificial bee colony algorithm. *Swarm and Evolutionary Computation*, *38*, 287–294. https://doi.org/10.1016/j.swevo.2017.09.002

Chen, S. D., & Ramli, A. R. (2003). Contrast enhancement using recursive mean-separate histogram equalization for scalable brightness preservation. *IEEE Transactions on Consumer Electronics*, *49*(4), 1301–1309.

Cocks, E., Taggart, M., Rind, F. C., & White, K. (2018). A guide to analysis and reconstruction of serial block face scanning electron microscopy data. *Journal of Microscopy*, *270*(2), 217–234. https://doi.org/10.1111/jmi.12676

El Malali, H., Assir, A., Bhateja, V., Mouhsen, A., & Harmouchi, M. (2020). A contrast enhancement model for x-ray mammograms using modified local s-curve transformation based on multi-objective optimization. *IEEE Sensors Journal*, *21*(10), 11543–11554. https://doi.org/10.1109/JSEN.2020.3028273

Feng, H., Ye, J., & Pease, R. F. (2006). Pattern reconstruction of scanning electron microscope images using long-range content complexity analysis of the edge ridge signal. *Journal of Vacuum Science & Technology B: Microelectronics and Nanometer Structures Processing, Measurement, and Phenomena*, *24*(6), 3110–3114.

Hamming, R. W. (1970). On the distribution of numbers. *The Bell System Technical Journal*, *49*(8), 1609–1625. https://doi.org/10.1002/j.1538-7305.1970.tb04281.x

Hashemi, S., Kiani, S., Noroozi, N., & Moghaddam, M. E. (2010). An image contrast enhancement method based on genetic algorithm. *Pattern Recognition Letters*, *31*(13), 1816–1824.

Jang, I. S., Kyung, W. J., Lee, T. H., & Ha, Y. H. (2011). Local contrast enhancement based on adaptive multiscale retinex using intensity distribution of input image. *Journal of Imaging Science and Technology*, *55*(4), 1–14.

Lal, S., & Chandra, M. (2014). Efficient algorithm for contrast enhancement of natural images. *International Arab Journal of Information Technology*, *11*(1), 95–102.

Lu, C. H., Hsu, H. Y., & Wang, L. (2009, May). A new contrast enhancement technique by adaptively increasing the value of histogram. In *2009 IEEE international workshop on imaging systems and techniques* (pp. 407–411). IEEE. https://doi.org/10.1109/IST.2009.5071676

Ma, H., & Han, L. (2014). Multi-technology integration based on low-contrast microscopic image enhancement. *Sensors & Transducers*, *163*(1), 96–102.

Mello-Román, J. C., Noguera, J. L. V., Legal-Ayala, H., Pinto-Roa, D. P., Monteiro, M. M., & Colmán, J. C. A. L. (2021). Microscopy mineral image enhancement using multiscale top-hat transform. In *2021 XLVII Latin American Computing Conference (CLEI)* (pp. 1–6). IEEE. https://doi.org/10.1109/CLEI53233.2021.9639975

Min, X., Gu, K., Zhai, G., Liu, J., Yang, X., & Chen, C. W. (2017). Blind quality assessment based on pseudo-reference image. *IEEE Transactions on Multimedia*, *20*(8), 2049–2062.

Mittal, A., Moorthy, A. K., & Bovik, A. C. (2012). No-reference image quality assessment in the spatial domain. *IEEE Transactions on Image Processing*, *21*(12), 4695–4708.

Ohta, K., Sadayama, S., Togo, A., Higashi, R., Tanoue, R., & Nakamura, K. I. (2012). Beam deceleration for block-face scanning electron microscopy of embedded biological tissue. *Micron*, *43*(5), 612–620. https://doi.org/10.1016/j.micron.2011.11.001

Parihar, A. S., Verma, O. P., & Khanna, C. (2017). Fuzzy-contextual contrast enhancement. *IEEE Transactions on Image Processing*, *26*(4), 1810–1819. https://doi.org/10.1109/TIP.2017.2665975

Pei, S. C., Zeng, Y. C., & Chang, C. H. (2004). Virtual restoration of ancient Chinese paintings using color contrast enhancement and lacuna texture synthesis. *IEEE Transactions on Image Processing*, *13*(3), 416–429. https://doi.org/10.1109/TIP.2003.821347

Sengee, N., Sengee, A., & Choi, H. K. (2010). Image contrast enhancement using bi-histogram equalization with neighborhood metrics. *IEEE Transactions on Consumer Electronics*, *56*(4), 2727–2734. https://doi.org/10.1109/TCE.2010.5681162

Shukri, N. M., Sim, K. S., & Leong, J. W. (2016). Minimum mean brightness error quad histogram equalization for scanning electron microscope images. In *2016 International Conference on Robotics, Automation and Sciences (ICORAS)* (pp. 1–6). IEEE. https://doi.org/10.1109/ICORAS.2016.7872601

Sim, K. S., Teh, V., Tey, Y. C., & Kho, T. K. (2016). Local dynamic range compensation for scanning electron microscope imaging system by sub-blocking multiple peak HE with convolution. *Scanning*, *38*(6), 492–501. https://doi.org/10.1002/sca.21285

Sim, K. S., Ting, F. F., Leong, J. W., & Tso, C. P. (2019). Signal-to-noise ratio estimation for SEM single image using cubic spline interpolation with linear least square regression. *Engineering Letters*, *27*(1), 151–165.

Sutton, M. A., Li, N., Joy, D. C., Reynolds, A. P., & Li, X. (2007). Scanning electron microscopy for quantitative small and large deformation measurements part I: SEM imaging at magnifications from 200 to 10,000. *Experimental Mechanics*, *47*(6), 775–787. https://doi.org/10.1007/s11340-007-9042-z

Vladár, A. E., Postek, M. T., & Ming, B. (2009). On the sub-nanometer resolution of scanning electron and helium ion microscopes. *Microscopy Today*, *17*(2), 6–13. https://doi.org/10.1017/S1551929500054420

Wighting, M. J., Lucking, R. A., & Christmann, E. P. (2004). The latest in handheld microscopes. *Science Scope*, *6*, 58–61.

Applied Computer Science, vol. 18, no. 2, pp. 43–55
doi: 10.35784/acs-2022-12

Submitted: 2022-03-28 | Revised: 2022-05-16 | Accepted: 2022-05-21

Keywords: finite element method (FEM), post-buckling, progressive failure analysis (PFA), delamination, cohesive zone model (CZM)

Blazej CZAJKA [0000-0002-0870-5334]*, *Patryk ROZYLO* [0000-0003-1997-3235]*, *Hubert DEBSKI* [0000-0002-1916-8896]*

STABILITY AND FAILURE OF THIN-WALLED COMPOSITE STRUCTURES WITH A SQUARE CROSS-SECTION

Abstract

This paper is devoted to the analysis of the stability and load-carrying capacity of thin-walled composite profiles in compression. The specimens reflect elements made of carbon fibre reinforced laminate (CFRP). Thin-walled columns with a square cross-section were made from 4 layers of composite in 3 different combinations of layer arrangements. Advanced numerical analyses have been carried out. In the first stage of the study, a buckling analysis of the structure was performed. In further numerical simulations, two advanced models were used simultaneously: the Progressive Failure Analysis (PFA) and the Cohesive Zone Model (CZM). The results showed significant differences between the critical load values for each layer configuration. The forms of buckling and the areas of damage initiation and evolution were also dependent on the applied layup.

1. INTRODUCTION

Thin-walled structures have been a very common type of load-bearing structure in many sectors of industry for many years. They have a major role to play in the construction of aircraft, vehicles and modern buildings. Thin-walled structural elements with different cross-sections, both open and closed (stringers, frames, profiles), are used to transfer loads. Due to the favourable weight/strength ratio, especially for aeronautical structures, more and more components are being manufactured from composite materials in favour of traditional engineering materials. One of the widely used composites is the continuous carbon fibre reinforced polymer (CFRP) laminate. It is also characterised by chemical and corrosion resistance and high fatigue strength (Chung, 1994). It is used in aviation to manufacture many responsible parts such as fuselage and landing gear components, airframes, and helicopter blades (Freeman, 1993). The most commonly used method of manufacturing critical composite parts is the autoclave technique (Campbell, 2004, 2006), which ensures high strength of these parts, repeatability of the manufacturing process, as well as low

* Lublin University of Technology, Faculty of Mechanical Engineering, Department of Machine Design and Mechatronics, Lublin, Poland, blazej.czajka@pollub.edu.pl, p.rozylo@pollub.pl, h.debski@pollub.pl

internal porosity of the composite material. Thin-walled load-bearing elements during exploitation should be used in the stable range, which is the subject of many scientific papers (Berardi, Perrella, Feo & Cricri, 2017; Fascetti, Feo, Nistici & Penna, 2016; Kubiak, Kolakowski, Swinarski, Urbaniak & Gliszczynski, 2016).

Buckling of a structural member may occur due to, for example, compressive loading (Debski, Teter, Kubiak & Samborski, 2016). This results in operation of the structure in the coverage range and accelerated failure. During stable working, thin-walled composite structures show the possibility of continuing to carry the axial compressive load, even after the buckling phenomenon has occurred (Koiter, 1963; Kubiak, Kolakowski, Swinarski, Urbaniak & Gliszczynski, 2016; Singer, Arbocz & Weller, 2000). As shown by previous studies (Debski, Rozylo, Gliszczynski & Kubiak, 2019; Falkowicz, Mazurek, Rozylo, Wysmulski & Smagowski, 2016; Wysmulski, Debski, Rozylo & Falkowicz, 2016), they have a large reserve of load-carrying capacity as long as the buckling is elastic in nature and the post-buckling equilibrium path remains stable. Therefore, the study of stability and the load-carrying capacity of thin-walled composite structures, requires analysis both in the state before and after the occurrence of loss of stability (Paszkiewicz & Kubiak, 2015; Rozylo, Debski, Wysmulski & Falkowicz, 2018). The analysis of composite structures determines the study of the full load range up to failure (Abrate, 1998) and the description of the phenomena of initiation and evolution of failure (Liu, Gu, Peng & Zheng, 2015). Many papers also demonstrate the ability of the described structures to carry loads after failure of the first laminate layer, as well as significant differences in limit load values, depending on the configuration of the composite layers (Debski, Teter, Kubiak & Samborski, 2016). Composite elements are characterised by a more complex failure mechanism than traditional materials (e.g. metals). They may fail as a result of tension or compression of the fibres, tension or compression of the matrix, and shear between layers (Camanho & Matthews, 1999; Lapczyk & Hurtado, 2007). This requires that experiments be conducted using several measurement methods simultaneously and that advanced failure models be applied during numerical simulations. Numerical analyses allowing observation of failure initiation and evolution phenomena are usually carried out using the progressive failure analysis (PFA) model (Camanho & Matthews, 1999; Lapczyk & Hurtado, 2007), whereas the cohesion zone model (CZM) is usually applied to describe the delamination phenomenon (Liu, Gu, Peng & Zheng, 2015).

In most of the published works, the authors focus only on open cross-sections. The current study is based on a comparison of thin-walled columns with a square cross-section (closed cross-section) prepared in 3 different laminate layer configurations. Furthermore, the numerical simulations have been carried out in a more detailed way than in previously published works. Both PFA and CZM numerical models were used simultaneously. Furthermore, the cohesion zones were used globally. Previous work uses cohesive zones only at delamination locations on real specimens during experimental tests. This definitely simplifies the model and may lead to the omission of delamination phenomena in other areas of the elements. The present work is devoted exclusively to numerical analysis as a preliminary to further research on closed sections. In order to validate the simulation results obtained, experimental tests are planned to be carried out in the next stages.

2. METHOD

2.1. Object of research

In this study, columns made of a closed square profile with a height equal to 250 mm were examined. The internal side length of the square was 40 mm. For a better representation of the real specimens, a corner rounding was used. The composite was made of 4 layers of laminate, each 0.1 mm thick. The exact dimensions of the model are shown in Figure 1. In this paper, 3 different configurations of the arrangement of the laminate layers were analysed:

- P1 – [0/90/90/0],
- P2 – [90/0/0/90],
- P3 – [45/0/0/45].

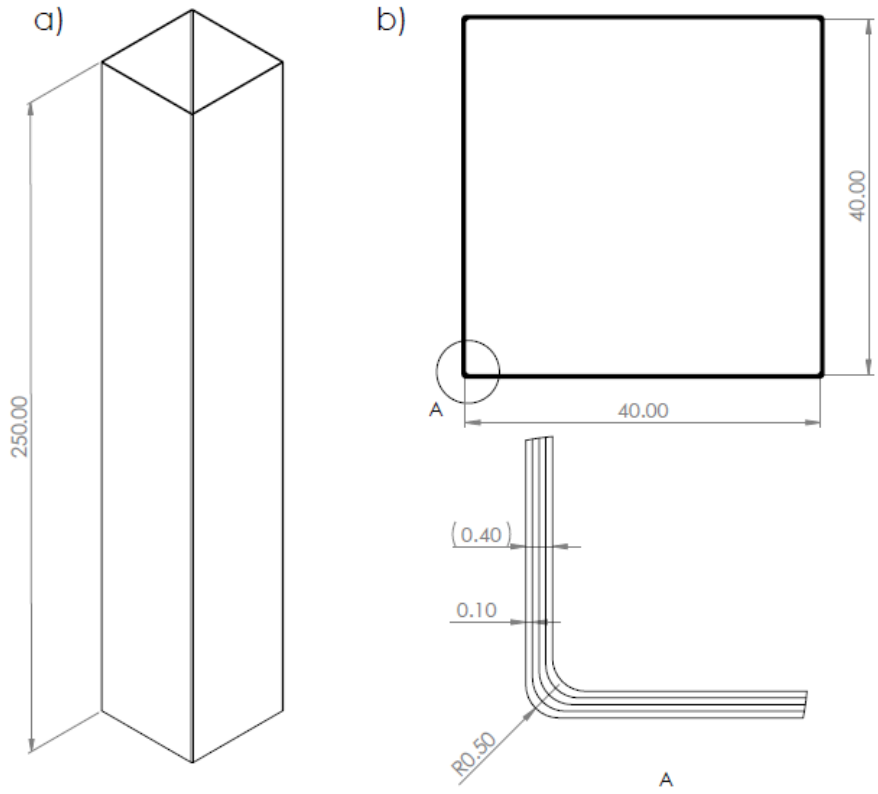

Fig. 1. Test specimen: a) specimen height, b) cross-sectional parameters

The specimens were made of carbon-epoxy laminate (CFRP). The used mechanical and strength properties are similar to those found in the literature (Rozylo, Debski, Wysmulski & Falkowicz, 2018) and shown in Table 1.

Tab. 1. Material properties of CFRP

Symbol	Property	Value	Unit
E_1	Young's modulus (along fibres)	130000	MPa
E_2	Young's modulus (perpendicular to fibres)	6500	
G_{12}	Kirchhoff modulus	5000	
ν_1	Poisson's coefficient	0.3	–
F_{T1}	Tensile Strength (along fibres)	2000	MPa
F_{C1}	Compressive Strength (along fibres)	100	
F_{T2}	Tensile Strength (perpendicular to fibres)	1500	
F_{C2}	Compressive Strength (perpendicular to fibres)	50	
F_{12}	Shear Strength	100	

2.2. Numerical analysis

The simulations were carried out based on the finite element method (FEM) using the Abaqus software. The first part of the research consisted in the analysis of the buckling of the structure. The Progressive Failure Analysis (PFA) and Cohesive Zone Model (CZM) were used to analyse post-buckling, loss of load-carrying capacity and delamination.

The first stage of the research was to solve the eigenproblem based on the minimum potential energy criterion. This allowed to obtain the buckling form and the critical load value. The critical load value was defined using the equation:

$$\left(K_0^{NM} + \lambda_i K_\Delta^{NM}\right) v_i^M = 0 \tag{1}$$

where: K_0^{NM} represents the stiffness matrix (corresponding to the base state), which includes the effects of preloads (P^N), K_Δ^{NM} denotes the differential initial stress as well as load stiffness matrix due to the incremental loading pattern (Q^N), λ_i represent the eigenvalues, v_i^M constitute the buckling mode shapes – eigenvectors, ^{M} and ^{N} refer to degrees of freedom M and N (of the whole model), $_i$ refers to the $_i$th mode of buckling. The critical buckling loads are $P^N + \lambda_i Q^N$. Furthermore, v_i^M constitute normalized vectors (and do not represent real magnitudes of deformation at critical load).

Then, simulations of non-linear loss of stability and load-carrying capacity of the structure were performed. The study also included the phenomenon of delamination occurring between the composite layers. In order to better represent the real phenomena, imperfections of the model from the form of buckling obtained in the first stage of research were used.

The preparation of the computational models involved making each laminate layer separately and then adding contact relations between them with the properties of cohesive layers. This made it possible to observe the delamination phenomenon in the whole model.

During the test, thin-walled composite columns were subjected to compressive loads over the full range up to failure. Two non-deformable plates were added to the ends of each column in order to best represent real conditions. Contact relationships were established between the composite columns and the plates in the normal and tangential directions. One of the plates (bottom plate) was fully fixed by removing all degrees of freedom. The upper plate was fixed in all directions except the direction along the height of the test specimen (Z axis). A compressive force was applied to this plate (fig. 2).

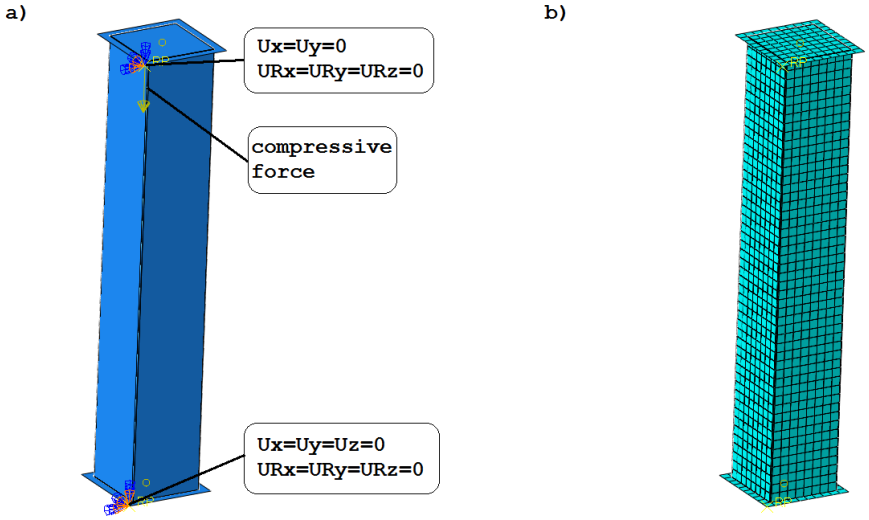

Fig. 2. Test specimen: a) constraints and loading, b) discrete model

The prepared models were discretised. Non-deformable, four-node elements with a linear shape function (R3D4) were used for the support plates. SC8R elements (eight-node shell elements with linear shape function) were used for the laminate layers. The numerical model for each layer layout consisted of 200 R3D4 elements, 8000 SC8R elements and 16562 nodes. A view of the discrete model is shown in Figure 2.

3. RESULTS

3.1. Buckling analysis

The analysis of the buckling of the structure showed significant differences between the studied arrangements of composite layers. The differences can be seen both in the values of critical loads causing buckling of the composite columns and in the form of buckling of the structure.

As shown in the graph (Fig. 3.), the obtained buckling load for the K3 configuration was the highest and amounted to about 804 N. The loss of stability for K1 and K2 occurred at similar load values of 703 N and 694 N, respectively. The load for the K3 configuration was therefore 14% and 16% higher respectively. This suggests that the use of layers at 45 degrees to the compressive force reinforces the structures and increases the buckling strength.

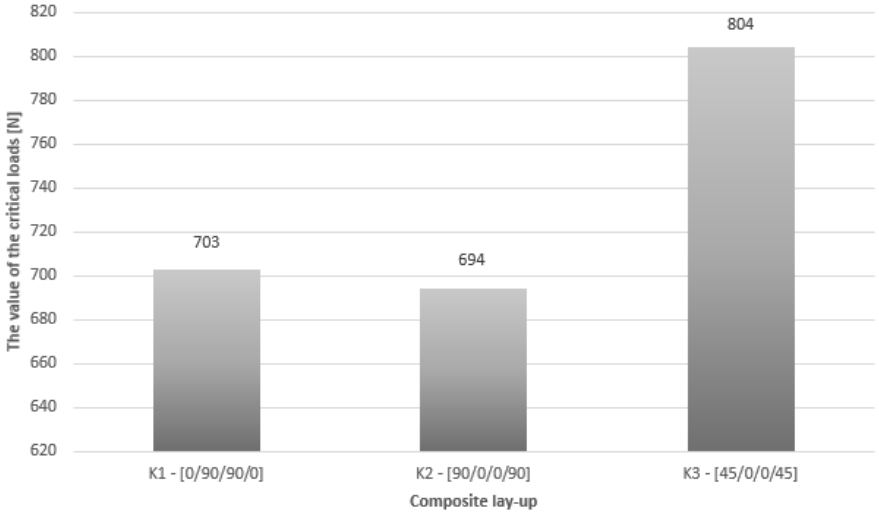

Fig. 3. Critical load values

The buckling forms, shown in Figure 4, are completely different depending on the layup. For configuration K1, 4 half-waves occur on each wall. The appearance of the half-waves is symmetrical with respect to the planes passing through the centres of the opposite edges of the cross-section. For the K2 configuration there is also symmetry, but the number of occurrence of half-waves has significantly increased to 9 on each wall. A completely different form of buckling is visible on the specimen in the K3 configuration. There are 5 half-waves on two of the walls and 7 half-waves on the other two walls. There is no symmetry as seen in the previous specimens. The half-waves are arranged at an angle of 45 degrees, according to the arrangement of fibres in the outer and inner layer of the composite.

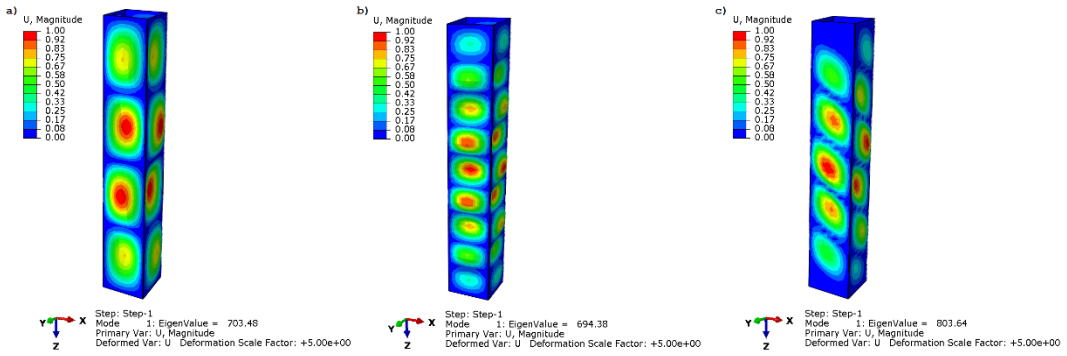

Fig. 4. Buckling view for layer arrangements: a) K1, b) K2, c) K3

3.2. Damage initiation

Damage initiation was analysed using two criteria: Tsai-Wu and Hashin. The results obtained with these criteria did not show much difference from each other. The biggest deviation was recorded for the K2 configuration, but it did not exceed 3.5%. Achieved values

of damage initiation forces and their differences between the used criteria are summarised in Table 2. In K1 and K2 configurations, damage initiation occurred at similar loads (for selected criteria). Opposite to buckling, configuration K3 was found to be the least strong at the time of damage initiation. The damage initiation load for K3 compared to the other configurations was about 16% lower according to the Tsai-Wu criterion and about 18% lower according to the Hashin criterion. It is important to emphasise that the failure initiation loads are as much as 5 to 7 times higher than the critical loads causing buckling of the structure. According to the Hashin criterion, the damage initiation occurred as a result of matrix tension – in the case of K1 configuration, and matrix compression in the case of K2 and K3 configurations.

Tab. 2. Load values for damage initiation (Tsai-wu and Hashin criteria)

Composite layup	Damage initiation forces [N]		Difference	
	Tsai-Wu criterion	Hashin criterion	[N]	[%]
K1	4995	5129 (matrix tension)	134	2.68
K2	4905	5128 (matrix compression)	168	3.43
K3	4218	4218 (matrix compression)	0	0

The distributions of damage initiation obtained with the Tsai-Wu criterion are shown in Figure 5. The analysis by using this criterion shows that initiation for each of the systems occurs on the inner layer, and only for the K1 configuration also on the outer layer.

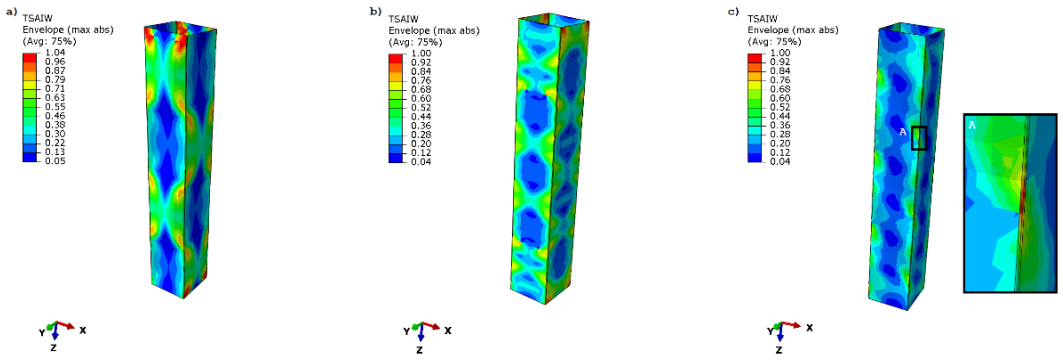

Fig. 5. Distribution maps of damage initiation on layer 1 – Tsai-Wu criterion: a) K1, b) K2, c) K3

For the Hashin criterion, for all configurations the damage initiation is visible on the inner layer. A view of the damage initiation distribution according to this criterion is shown in Figure 6.

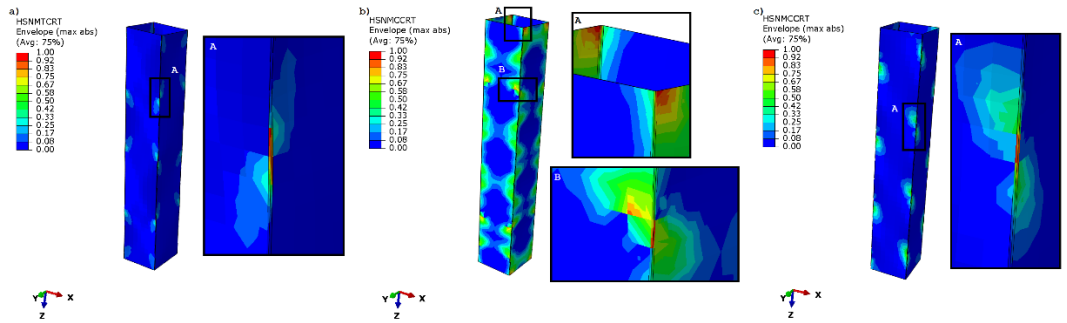

Fig. 6. Distribution maps of damage initiation on layer 1 – Hashin criterion: a) K1, b) K2, c) K3

In general, the areas exposed to damage initiation are the corners of the tested columns and the buckling half-wave hinge locations at the edges of the element. The areas of damage initiation are identical except the layup configuration K1. For this layup, according to the Tsai-Wu criterion, the corners are the locations of damage initiation. In the case of analysis using the Hashin criterion, damage initiation occurs at the edges of the element at the half-wave inflection point. Low values for this criterion are observed in the corners.

3.3. Damage evolution

The application of progressive failure analysis (PFA) has allowed the study of the areas of occurrence, the failure mechanism and the loads at the time of damage evolution. The damage evolution occurred in 1 layer of the composite for each of the investigated configurations. The areas were identical to those observed at failure initiation (Fig. 7).

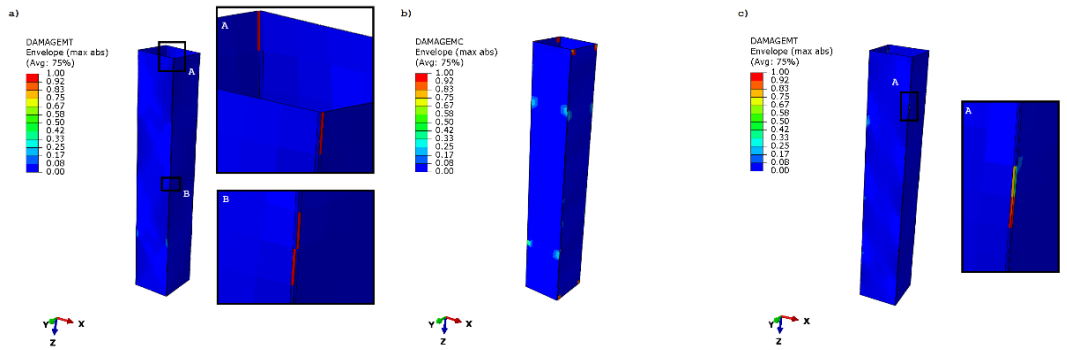

Fig. 7. Areas of damage evolution in different layups: a) K1 – DAMAGEMT, b) K2 – DAMAGEMC, c) K3 - DAMAGEMT

For the K1 and K3 layer configurations, the damage occurred by tension of the composite matrix (DAMAGEMT), while for K2 it occurred by compression of the matrix (DAMAGEMC). During the tests carried out for all configurations, matrix damage occurred in both tension and compression before the tested structure lost its load-carrying capacity. For configurations K2 and K3 the fibre damage (DAMAGEFC) was also observed in compression but after the loss of load-carrying capacity. The fibre failure due to tension (DAMAGEFT) and, in the case of K1, due to compression were not reached during the tests.

The loads that caused the reach of the individual parameters are summarised in the table below (Tab. 3).

Tab. 3. Load values at damage evolution

Composite layup	Load values [N]			
	DAMAGEMC	DAMAGEMT	DAMAGEFC	DAMAGEFT
K1	5602	**5518**	–	–
K2	**5557**	5826	5116*	–
K3	6471	**5486**	6321*	–

* – evolution has taken place after the loss of load-carrying capacity

3.4. Delamination

Observation of the delamination phenomenon was possible by using the cohesive zone model (CZM). Both the initiation (CSMAXSCRT) and evolution of delamination (CSDMG) occurred in areas close to the initiation and evolution of failure. The main areas exposed to delamination were the corners of the elements and the half-wave inflection points at their edges. The locations of occurrence between layers 3 and 4 for the K2 configuration are shown in Figure 8.

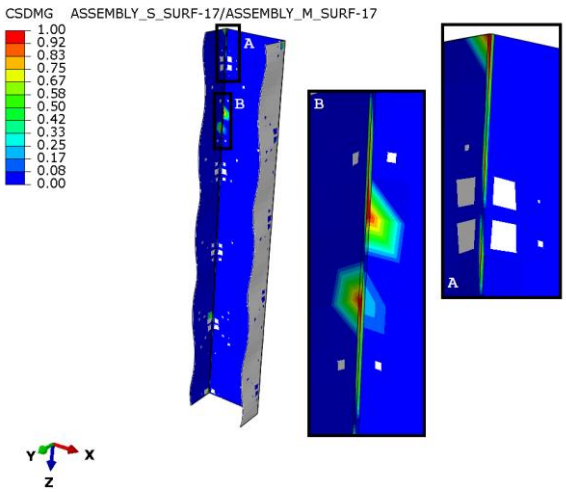

Fig. 8. Locations of delamination between layers 3 and 4 - K2 configuration

The applied numerical model allowed for excellent visualisation of the delamination phenomenon for the tested samples. It is especially visible in the corners of the investigated composite columns. The following figure (Fig. 9) shows a view of delamination for the K2 configuration.

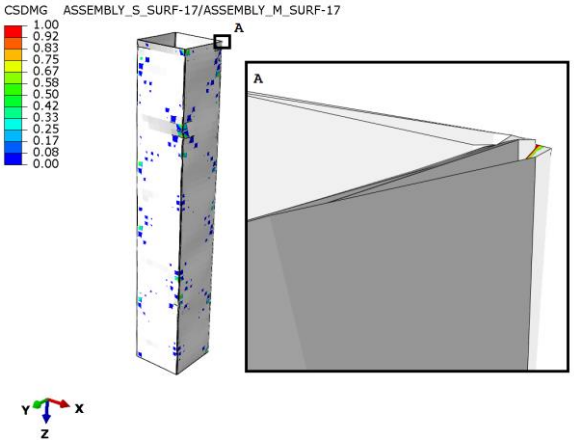

Fig. 9. Delamination view for K2 configuration

For each of the tested configurations, delamination initiation between at least two layers occurred before damage initiation. Delamination initiation was achieved for all specimens between each layer during the tests. Each of them occurred before the loss of load-carrying capacity of the tested structures. The delamination evolution was not achieved only between layers 2 and 3 in the K1 configuration. For each configuration, at least between two of the layers delamination occurred before the loss of load-carrying capacity of the structure. The occurrence of the phenomenon in the load-carrying area of composite structures confirms the importance of its analysis. This may allow better prediction of the behaviour of real structures made of laminates.

3.5. Equilibrium paths and loss of load-carrying capacity

By carrying out the study over the full load range, the moment of loss of bearing capacity was obtained. In order to analyse this phenomenon, equilibrium paths were determined. They allow for a convenient analysis of the sequence of occurrence of particular phenomena during compression of the tested specimens. The equilibrium path for the K3 configuration is shown in Figure 10.

In the presented configuration, delamination initiation occurred at forces of 3083 N and 3257 N. Subsequently, damage initiation occurred at a force of 4218 N (according to Tsai_Wu and Hashin's criterion). Although this point was exceeded, the structure still carried the load, which increased continuously. Successively, the matrix damage evolution took place by tension, compression and then the delamination between layers 1 and 2, and layers 3 and 4 occurred. Loss of load-carrying capacity occurred only when a load of 6642 N was reached. In the same calculation step, delamination evolved between layers 2 and 3.

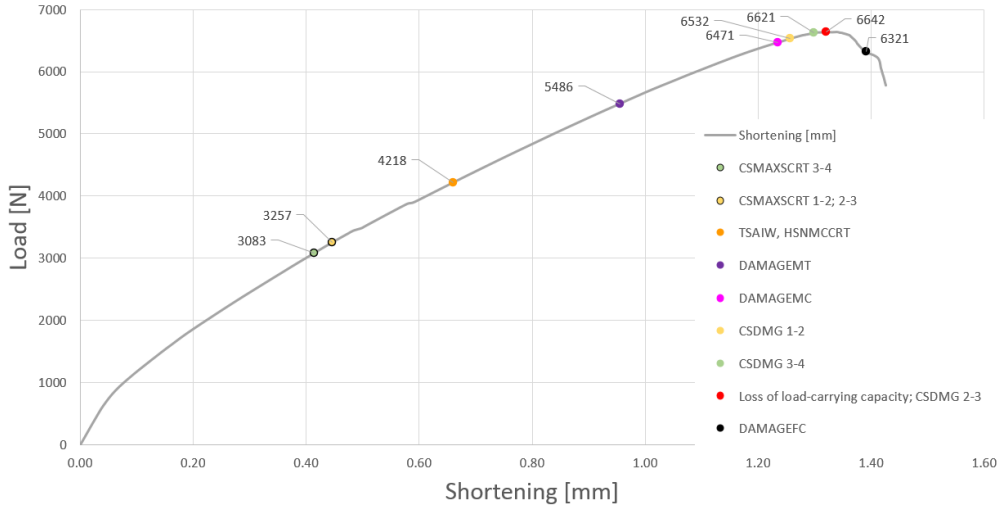

Fig. 10. Equilibrium path – K3 layup

The load causing loss of load-carrying capacity for all the tested composites was significantly higher than the load causing damage initiation. For the K3 configuration, this difference was as high as 2424 N, which is about 57% of the value of the damage initiation load. For K1 and K2 configurations the differences were smaller but also significant. They were 622 N (12%) and 922 N (19%), respectively. The K3 configuration was characterized by the highest load-carrying capacity (Fig. 11).

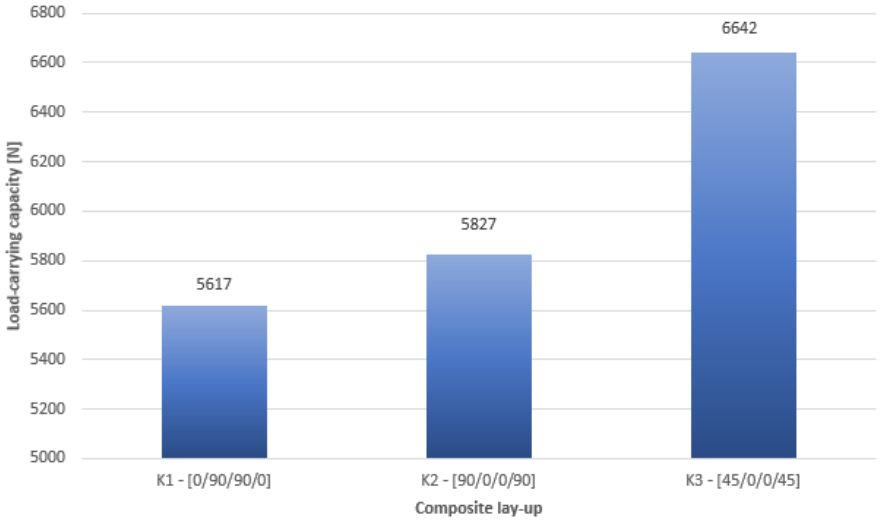

Fig. 11. Load-carrying capacity for different configurations

4. CONCLUSIONS

The numerical analyses carried out allowed comparison of composite thin-walled columns with square cross-sections and various arrangements of laminate layers. They also provided a preliminary study of the stability and load-carrying capacity of compression composite profiles with closed cross-sections. The conducted research results in the following conclusions:

- the buckling analysis of thin-walled structures with square cross-section is possible by using FEM and solving the eigenproblem,
- applying the PFA model allows to thoroughly analyse the post-buckling behaviour of composite columns with square cross-section,
- the Cohesive Zone Model (CZM) is a useful method to analyse the phenomenon of delamination in composite structures with closed cross-section,
- the arrangement of composite layers has a significant influence on buckling, initiation and evolution of damage, delamination, as well as the load-carrying capacity of composite structures,
- the sample with layers arranged at the angle of 45 degrees was characterised by the lowest stability of the structure, but at the same time the highest load-carrying capacity,
- for all tested configurations the phenomenon of delamination occurred before the loss of load-carrying capacity, which confirms the importance of its investigation,
- each of the tested specimens lost its load-carrying capacity at a load significantly higher than the load occurring at the damage initiation.

Future experimental research using a universal testing machine is planned as part of the project No. 2021/41/B/ST8/00148 (National Science Centre, Poland). The study of the composite structure damage will be performed based on acoustic emission method and microscopic analysis. A digital microscope with a mobile head will be used to record the forms of failure during compression of the specimens.

Funding

The publication was financed by Grant – Lublin University of Technology Doctoral School – Błażej Czajka.

Acknowledgments

The research has been conducted under project No. 2021/41/B/ST8/00148 (National Science Centre, Poland)

REFERENCES

Abrate, S. (1998). *Impact on Composite Structures.* Cambridge University Press.

Berardi, V. P., Perrella, M., Feo, L., & Cricri, G. (2017). Creep behavior of GFRP laminates and their phases: Experimental investigation and analytical modelling. *Composites Part B: Engineering*, *122*, 136–144. https://doi.org/10.1016/j.compositesb.2017.04.015

Camanho, P. P., & Matthews, F. L. (1999). A Progressive Damage Model for Mechanically Fastened Joints in Composite Laminates. *Journal of Composite Materials*, *33*(24), 2248–2280. https://doi.org/10.1177%2F002199839903302402

Campbell, F. C. (2004). *Manufacturing Processes for Advanced Composites.* Elsevier B.V.

Campbell, F. C. (2006). *Manufacturing Technology for Aerospace Structural Materials.* Elsevier Ltd.

Chung, D. D. L. (1994). *Carbon Fiber Composites.* Elsevier Inc.

Debski, H., Rozylo, P., Gliszczynski, A., & Kubiak, T. (2019). Numerical models for buckling, postbuckling and failure analysis of pre-damaged thin-walled composite struts subjected to uniform compression. *Thin-Walled Structures*, *139*, 53–65. https://doi.org/10.1016/j.tws.2019.02.030

Debski, H., Teter, A., Kubiak, T., & Samborski, S. (2016). Local buckling, post-buckling and collapse of thin-walled channel section composite columns subjected to quasi-static compression. *Composite Structures*, *136*, 593–601. https://doi.org/10.1016/j.compstruct.2015.11.008

Falkowicz, K., Mazurek, P., Rozylo, P., Wysmulski, P., & Smagowski, W. (2016). Experimental and numerical analysis of the compression thin-walled composite plate. *Advances in Science and Technology Research Journal*, *10*(31), 177–184. https://doi.org/10.12913/22998624/64063

Fascetti, A., Feo, L., Nisticò, N., & Penna, R. (2016). Web-flange behavior of pultruded GFRP I-beams: A lattice model for the interpretation of experimental results. *Composites Part B: Engineering*, *100*, 257–269. https://doi.org/10.1016/j.compositesb.2016.06.058

Freeman, W. T. (1993). The use of composites in aircraft primary structure. *Composites Engineering*, *3*(7–8), 767–775. https://doi.org/10.1016/0961-9526(93)90095-2

Koiter, W. (1963). *Elastic Stability and Post Buckling Behavior in Nonlinear Problems.* University of Wisconsin Press.

Kubiak, T., Kolakowski, Z., Swinarski, J., Urbaniak, M., & Gliszczynski, A. (2016). Local buckling and post-buckling of composite channel-section beams – Numerical and experimental investigations. *Composites Part B: Engineering*, *91*, 176–188. https://doi.org/10.1016/j.compositesb.2016.01.053

Lapczyk, I., & Hurtado, J. A. (2007). Progressive damage modeling in fiber-reinforced materials. *Composites Part A: Applied Science and Manufacturing*, *38*(11), 2333–2341. https://doi.org/10.1016/j.compositesa.2007.01.017

Liu, P. F., Gu, Z. P., Peng, X. Q., & Zheng, J. Y. (2015). Finite element analysis of the influence of cohesive law parameters on the multiple delamination behaviors of composites under compression. *Composite Structures*, *131*, 975–986. https://doi.org/10.1016/j.compstruct.2015.06.058

Paszkiewicz, M., & Kubiak, T. (2015). Selected problems concerning determination of the buckling load of channel section beams and columns. *Thin-Walled Structures*, *93*, 112–121. https://doi.org/10.1016/j.tws.2015.03.009

Rozylo, P., Debski, H., Wysmulski, P., & Falkowicz, K. (2018). Numerical and experimental failure analysis of thin-walled composite columns with a top-hat cross section under axial compression. *Composite Structures*, *204*, 207–216. https://doi.org/10.1016/j.compstruct.2018.07.068

Singer, J., Arbocz, J., & Weller, T. (1998). *Buckling Experiments: Experimental Methods in Buckling of Thin-Walled Structures, Volume 1: Basic Concepts, Columns, Beams and Plates.* John Wiley & Sons Inc.

Wysmulski, P., Debski, H., Rozylo, P., & Falkowicz, K. (2016). A study of stability and post-critical behaviour of thin-walled composite profiles under compression. *Eksploatacja i Niezawodnosc-Maintenance and Reliability*, *18*(4), 632–637. http://dx.doi.org/10.17531/ein.2016.4.19

Applied Computer Science, vol.18, no. 2, pp. 56–70
doi: 10.35784/acs-2022-13

Submitted: 2022-05-16 | Revised: 2022-06-17 | Accepted: 2022-06-21

Keywords: Leaf Disease Detection, Convolutional Neural Network, Deep Learning, Transfer Learning.

Mahmoud BAKR[*], *Sayed ABDEL-GABER*[**], *Mona NASR*[**], *Maryam HAZMAN*[*]

TOMATO DISEASE DETECTION MODEL BASED ON DENSENET AND TRANSFER LEARNING

Abstract

Plant diseases are a foremost risk to the safety of food. They have the potential to significantly reduce agricultural products quality and quantity. In agriculture sectors, it is the most prominent challenge to recognize plant diseases. In computer vision, the Convolutional Neural Network (CNN) produces good results when solving image classification tasks. For plant disease diagnosis, many deep learning architectures have been applied. This paper introduces a transfer learning based model for detecting tomato leaf diseases. This study proposes a model of DenseNet201 as a transfer learning-based model and CNN classifier. A comparison study between four deep learning models (VGG16, Inception V3, ResNet152V2 and DenseNet201) done in order to determine the best accuracy in using transfer learning in plant disease detection. The used images dataset contains 22930 photos of tomato leaves in 10 different classes, 9 disorders and one healthy class. In our experimental, the results shows that the proposed model achieves the highest training accuracy of 99.84% and validation accuracy of 99.30%.

1. INTRODUCTION

Agriculture is a major component of the Egyptian economy, contributing up to 11.3 percent of Gross Domestic Product (GDP) and 28 percent of all jobs. The economy relies on agricultural product quality, which is affected by weather and other environmental factors. Since a wide range of agricultural products are produced and exported to many countries, it is vital to generate high-quality products with an acceptable yield. Over 80% of the human diet is comprised of plants production. Plants are afflicted by a variety of plant diseases, including bacteria, fungus, and viruses. According to Food and Agriculture Organization (FAO), plant pests and diseases are responsible for losses of 20 to 40% of global food production (Plant Health and Food Security, 2017). For Egypt, assisting in the resolution of this issue is a huge challenge helping to achieve food security.

[*] Climate Change Information Center and Expert Systems, Agricultural Research Center, Egypt, mah.bakr.2005@gmail.com
[**] Faculty of Computers and Artificial Intelligence, Helwan University, Cairo, Egypt, m.nasr@helwan.edu.eg

In the case of farming, disease mitigation has recently become a significant factor. Plant disease identification is essential in the field of agriculture since plant diseases are unavoidable. The most diseases' symptoms are appeared on plant leaves. So, checking the status of a diseased plant's leaves is the simplest technique to figure out if it's infected. Plant disease recognition is a challenging task for agriculture specialists to tackle since it necessitates the use of scientific procedures and a long period of observation (Mohamed, Abdel-Gaber, Nasr & Hazman, 2020).

The shortage of agricultural extension workers involved in providing agricultural advice and guidance to farmers has become a major problem in Egypt. So that, farmers become dependent on themselves or the Internet to solve any problem they face in agricultural operations.

As the widespread use of smart phones among farmers, as well as the widespread use of graphics processing units (GPU) in computers and servers, and the rapid advancement of artificial intelligence, computer vision, and deep learning techniques, it becomes a necessary to develop an automated system that can perform plant disease recognition operations and provide an effective solution.

Plant diseases can be detected using CNNs (Venkatesh et al., 2020). CNN is one of the most powerful pattern identification techniques for massive data sets. CNN has a really encouraging performance in terms of detecting these disorders. Various CNN classification architectures, VGG16, Inception V3 and DenseNet201 were previously used in diseases detection (Venkatesh et al., 2020; Peyal et al., 2021).

In order to develop an automatic plant leaf disease detection, a comparison study is applied to find the high accuracy CNN deep learning models. Then the one with highest results is used as the base transfer learning model for our proposed model. The base transfer learning model works as feature extraction followed by a CNN classifier. The contributions of this research are:

a) comparison among some transfer learning based models,
b) proposed model based on DenseNet transfer learning as features extractor and a CNN classifier.

In the presented study, Tomato leaves images a subset of the plantvillage images dataset are used. It includes 22930 photos for 10 different classes downloaded from kaggle website (Kaggle, 2018). These classes are: tomato Bacterial spot, tomato early blight, tomato late blight, tomato leaf mold, tomato septoria leaf spot, tomato spider mites two spotted spider mite, tomato target spot, tomato yellow leaf curl virus, tomato mosaic virus and tomato healthy. First, the selected tomato images dataset is resized and augmented to be ready for training the classification model. In order to improve the classification results, we do some fine-tuning to classification models and rerun the classification models. Then, we test different models against subset of images. The DenseNet model gives the highest accuracy used as features extractor to our proposed CNN model. Finally, we compared the results and analyze them.

The paper is arranged as follows: Section 2 describe previous related works. Methodology has been explained in Section 3. Section 4 highlights the proposed model. Section 5 holds experimental result and analysis. Concluding remarks is in Section 6.

2. LITERATURE REVIEW

Over the years, there has been debate on how to detect plant diseases. Many researchers have used machine learning approaches to construct a variety of acceptable designs for detecting plant diseases.

The authors in (Rangarajan, Purushothaman & Ramesh, 2018) utilised AlexNet and VGG16 to classify six different tomato diseases as well as a healthy class. The performance was assessed by changing the number of images, batch sizes, and weight and bias learning rates. They concluded that AlexNet outperforms VGG16 in terms of accuracy and execution time. It should be noted that, given that this work is also aimed at the classification of diseases found in tomato plants. Their proposed methodology was developed based on the results reported by this comparison, allowing support in the delimitation of the work and selection of architectures to implement. While being able to discard the implementation of VGG16 due to the disadvantages it presents in comparison to AlexNet, particularly in the computable domain.

The authors in (Hong, Lin & Huang, 2020) used transfer learning to reduce the size of the training data, the time and the computational costs when building deep learning. They classify 9 types of disease leaves including healthy tomato leaves. Five deep network structures of Resnet50, Xception, MobileNet, ShuffleNet and Densenet121_Xception were applied to perform the feature extraction. Those network structures with different learning rates were compared in experiment. Adjust the appropriate training parameters and test those networks. Compared the five convolutional neural network, the parameters and the average accuracy are different. The best recognition accuracy of Densenet_Xception is 97.10%, but the parameters of Densenet_Xception are at most. The recognition accuracy of ShuffleNet is 83.68%, and the paramenters are small.

The authors in (Kabir, Ohi & Mridha, 2020) investigated an optimal plant disease identification model combining the diagnosis of multiple plants. They used data that collected from various online sources and it included leaf images of six plants: tomato, potato, rice, corn, grape, and apple. They implemented numerous popular convolutional neural network (CNN) architectures. They found that the Xception as well as DenseNet architectures perform better in multi-label plant disease classification tasks.

The authors in (Agarwal et al., 2020) applied a CNN based approach for the disease detection and classification of Tomato. The experimental results shows the efficacy of the proposed model over pre-trained model i.e. VGG16, InceptionV3 and MobileNet. The classification accuracy varies from 76% to 100% with respect to classes and average accuracy of the proposed model is 91.2% for the 9 disease and 1 healthy class.

The authors in (Afifi, Alhumam & Abdelwahab, 2021) developed and evaluated several methods for identifying plant diseases with little data. They used three CNN architectures (ResNet18, ResNet34, and ResNet50) to build two baseline models, a Triplet network and a deep adversarial Metric Learning (DAML) approach. These approaches were trained from a large source domain dataset and then tuned to identify new diseases from few images, ranging from 5 to 50 images per disease. Their proposed approaches were evaluated in the case of identifying the disease and plant species together or only if the disease was identified, regardless of the affected plant. The results show that the baseline model achieved an accuracy of 99% when the shift from source domain to target domain was small and 81% when that shift was large and outperformed all other competitive approaches.

The authors in (Ji, Zhang & Wu, 2020) proposed a CNN model to identify grape diseases from images into 4 classes. The proposed model is a united CNNs architecture based on Google InceptionV3 and ResNet50 called UnitedModel. UnitedModel takes advantage of the combination of InceptionV3's width and ResNet50's depth and learn from the output features layers from both models. The proposed UnitedModel achieves 99.17% accuracy.

In this paper, we compare four different deep learning models based on transfer learning. As our pre-trained model in Transfer Learning, we mostly employed the DenseNet201 network, a common CNN architecture. Several Transfer Learning architectures were also examined with a few additional well-known pre-trained models (VGG16, Inception V3 and ResNet152V2) and compared to DenseNet201. Additionally, Fine-Tuning has been performed to improve the detection accuracy. The dataset in our experiment includes 9 different diseases as well as the images from healthy plants. Our method for detecting plant diseases is presented in the below section.

3. METHODOLOGY

In this paper, several types of supervised deep learning techniques are utilized to detect tomato leaves diseases. We aim to explore their performance in detecting the 10 considered tomato diseases and concluding the best of them. Then we will use the best model as the base model for our proposed model.

Several steps are necessary for the implementation of deep learning models. The data set is first collected, then divided into two portions, usually 80 percent training and 20 percent validation. Deep learning models are then trained from scratch or using the transfer learning technique, and training/validation plots are created to determine the models' significance. The images are next classified using performance metrics (type of plant disease), and finally, visualization techniques/mappings are utilized to classify the images (Saleem, Potgieter & Arif, 2019).

It has been demonstrated that CNNs do not require pre-processing, feature extraction, or feature classification in order to perform image recognition. The trained model, on the other hand, can swiftly classify the image. The training of a large-scale neural network takes a long time, and it requires a massive number of data sets. Also manually labelling data according to specified selection criteria is laborious and expensive (Chen et al., 2020).

When developing deep learning models, transfer learning is a knowledge sharing strategy that decreases the size of the training data, the time, and the computing cost. Transfer learning allows a pre-trained model's learning to be transferred to a new model. Transfer learning is a machine learning approach in which CNNs trained for a task is reused as the starting point for a model on another task (Peyal et al., 2021; Chen et al., 2020).

In order to compare between different models, we follow the steps shown in Fig. 1. First, we select the tomato images dataset, which is a subset form plantvillage images dataset. Then the required preprocessing of images like resizing is applied. After augmenting the images, we build the training model using the selected classification models. To improve results of the used models, we do some fine-tuning to the classification models and retrain them to get better results. Then we test the selected models against subset of images. Finally, we analyse the findings and the results.

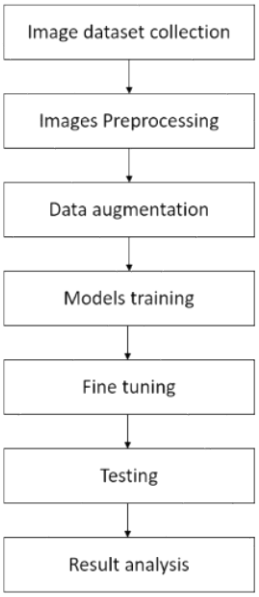

Fig. 1. Steps of Detection and classification process for leaf diseases

3.1. Tomato leaves images dataset

Tomato Dataset is a subset of the larger plantvillage dataset (Kaggle, 2018). It contains 22930 images, divided into three sets: 75% for training, 20% for validation and 5% for testing. A tomato leaf appears in every image in the data set, and the leaf takes up the majority of the image's space and provides an almost constant background. The data set divided into 10 classes, 9 classes of tomato diseases beside the tomato healthy class. The 10 classes were as follow: tomato Bacterial spot, tomato early blight, tomato late blight, tomato leaf mold, tomato septoria leaf spot, tomato spider mites two spotted spider mite, tomato target spot, tomato yellow leaf curl virus, tomato mosaic virus and tomato healthy. They are shown in Fig. 2. Table 1 shows the number of images for each disease.

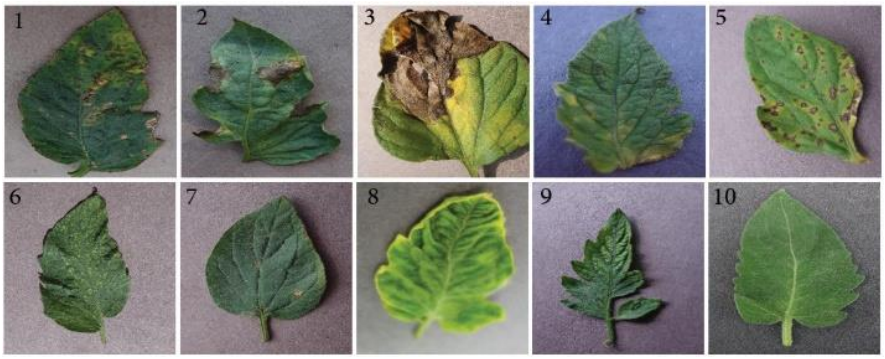

Fig. 2. Examples of tomato 10 classes – (1) Bacterial spot, (2) Early blight, (3) Late blight, (4) Leaf mold, (5) Septoria leaf spot, (6) Spider mites two spotted, (7) Target spot, (8) Yellow leaf curl virus, (9) Mosaic virus and (10) Tomato healthy

Tab. 1. Images count for each class of Tomato dataset

Tomato Class	Training Images	Validating Images	Testing Images
Bacterial spot	1,617	425	85
Early blight	1,824	480	96
Late blight	1,758	463	93
Leaf mold	1,788	470	94
Septoria leaf spot	1,658	436	87
Spider mites Two-spotted	1,654	435	87
Target spot	1,736	457	91
Yellow leaf curl virus	1,863	490	98
Mosaic virus	1,700	448	90
healthy	1,830	481	96

3.2. Image preprocessing

Image preprocessing enhances the quality of the image data needed for image classification. Geometric transformations of images, such as image rotation, scaling, and translation, are used in preprocessing approaches. In this step, we decreased the resolution of all of the images to 224*224 pixels during the preprocessing stages, the original images are 256*256 pixels. It must ensure that all images are of the same size and resolution.

3.3. Augmentation Process

CNN requires a large amount of training data to achieve improved results (Shorten & Khoshgoftaar, 2019). In order to improve the model's performance, image augmentation is frequently required to create the best deep CNN model with insufficient training data. Image augmentation increases the amount of images in the data set and reduces overfitting by adding a few distorted photos to the training data. When the network learns the data rather than the overall pattern of the dataset, this is known as overfitting. Image augmentation artificially creates training images using a range of processing methods or a combination of processing methods such as image flipping, rotation, blur, relighting, and random cropping (Chen et al., 2020). In our study we do the following for images augmentation: scaling the images, shearing, zooming and horizontal flipping.

3.4. Fine-tuning

Fine-tuning is a technique for improving a function's efficiency. It makes little adjustments to improve the outcome. The adjustment process is so important that even minor changes have a significant impact on the training process in terms of computation time, convergence speed, and the number of processing units used (Too, Yujian, Njuki & Yingchun, 2019). This fine-tuning process was repeated several times to improve the accuracy of our model. The parameters used for training and fine-tuning that give best results are as shown in Table 2.

Tab. 2. Fine-Tuning parameters and values used through training models

Parameter	Value
Batch size	32
Steps per epoch	545
Epoch	50
Validation steps	1
Optimizer	Adam
Activation function	Softmax

3.5. Training the models

In this step, the selected CNN models trained on the data set of tomato diseases identification. During the training process, the fixed low-level network parameters are unchanged, the high-level network parameters are fine-tuned. The tomato disease image is input into the network to train the high-level parameters of the network, and the trained model is used to classify the 10 classes of tomato leaves. The selected CNN are VGG16, Inception V3, Resnet152V2 and DenseNet201.

3.5.1. VGG16

The VGG architecture was introduced in 2014 by Simonyan and Zisserman of Oxford University's Visual Geometry Group and Google DeepMind. It's popular because it's straightforward, with only 16 convolutional layers stacked on top of one another. It features two fully connected layers with 4096 nodes each and a softmax classifier, as well as max-pooling layers that help reduce volume size (Simonyan & Zisserman, 2015). VGG16 is made up of thirteen convolution layers, including five combined max-pooling layers and three completely connected layers, according to their research. The rectified linear unit (ReLU) function comes after the second fully connected dense layer. The network's last layer is a softmax regression classifier, which uses probability to classify the input images. For VGG16 architecture, the image input size is appointed to 224 x 224 x 3. Fig. 3 shows the architecture of VGG16 model. In our study, for transfer learning of VGG16, the last layer with 1000 output classes was deleted and the model output was flattened then, a dense layer with 10 outputs -tomato classes- was added to the model.

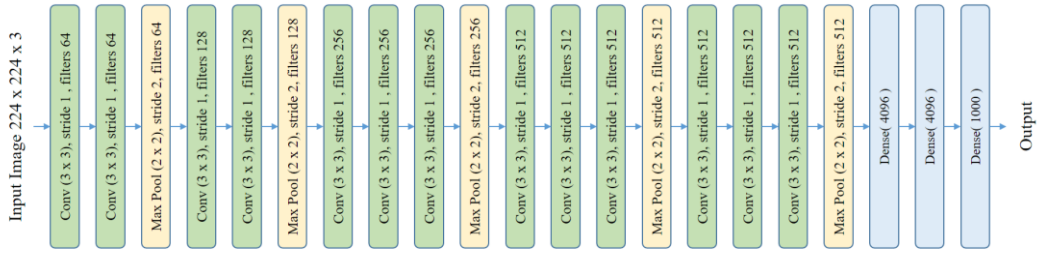

Fig. 3. VGG16 architecture

3.5.2. Inception V3

The deep convolutional architecture Inception V3 is commonly utilized for classification problems. Szegedy and his colleagues presented their model concept based on the GoogleNet design (Szegedy et al., 2016). By changing the inception module, Inception V3 was created. Each block of the Inception V3 network comprises several symmetric and asymmetric building blocks, as well as various branches of convolutions, average pooling, max pooling, concatenated, dropouts, and fully-connected layers. Because there are 42 layers and 29.3 million parameters in this network, the computational cost is just 2.5 times that of GoogleNet. Finally, the scientists discovered that by reducing the number of parameters and further regularising the network with batch normalised auxiliary classifiers label smoothing, they can train a high-quality network on tiny training sets (Szegedy et al., 2016). Fig. 4 shows the architecture of Inception V3 model. In our study, for transfer learning of Inception V3, the top layer was deleted and the model output was flattened then, a dense layer with 10 outputs -tomato classes- was added on the top of the model.

Fig. 4. Inception V3 architecture

3.5.3. Resnet152V2

A CNN architecture with hundreds or thousands of convolutional layers is known as a Residual Network (ResNet) (Gulli & Pal, 2017). Additional layers' efficacy was reduced by previous CNN configurations. ResNet has a large number of layers and is extremely fast. The main difference between ResNetV2 and the original (V1) is that V2 applies batch normalization to each weight layer before applying it. ResNet has great performance in image recognition and localization tasks, demonstrating the importance of numerous visual recognition tasks (Kumar, Arora, Harsh & Sisodia, 2020). Fig. 5 shows the architecture of Resnet152V2 model which include 152 layers in depth and build mainly from 3-layer blocks. In our study, for transfer learning of Resnet152V2, the last output layer was deleted and the model output was flattened then, a dense layer with 10 outputs – tomato classes – was added to the top of the model.

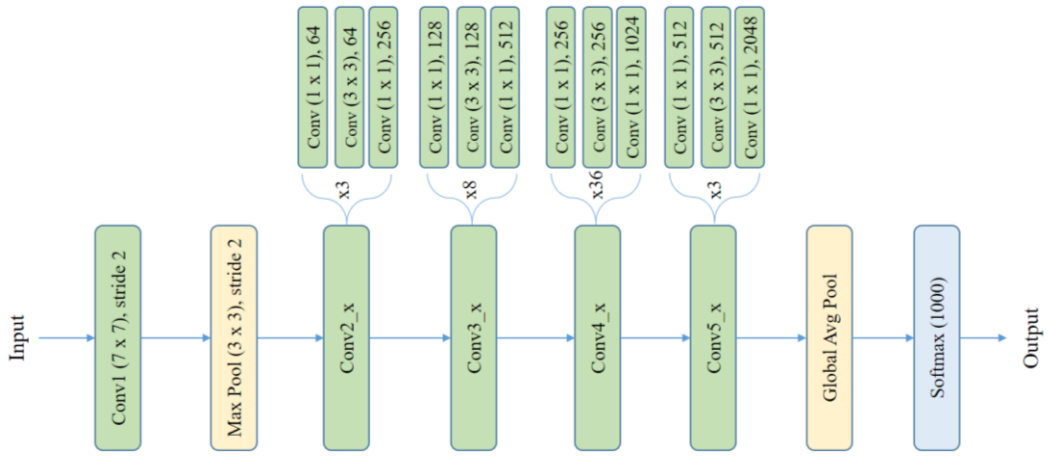

Fig. 5. ResNet152V2 architecture

3.5.4. DenseNet201

Authors in (Huang, Liu & Weinberger, 2016) proposed a highly linked convolutional network design in their study. All layers in the network are connected directly to each other in a feed-forward manner to enable maximum information flow between them. All previous layers' feature-maps are utilized as inputs into each layer, and its own feature-maps are used as inputs into all subsequent layers. DenseNets solves the vanishing-gradient problem while drastically reducing the number of parameters. Fig. 7 shows the architecture of DenseNet201 model which explained in more detailed in the following section.

4. PROPOSED MODEL

In this section, the proposed model based on a pre-trained model and CNN classifier is designed for the prediction and classification of tomato diseases from infected leaves images. The pre-trained architecture utilized in the proposed model is DenseNet201 as it gives the highest accuracy among other models. DenseNet201 is used to extract features, which are then fed into a CNN for classification. The test set and validation set are then used to evaluate the proposed model. As shown in Fig. 6, the suggested model contains five phases. The first phase is data pre-processing. The second phase is data augmentation. The feature extraction phase, which uses the pre-trained architecture DenseNet201 with transfer learning, is the third phase. The classification of tomato leaf diseases using the retrieved features and the CNN classifier is the fourth phase. The final phase is performance measurement and analysis. The first two phases of images pre-processing and data augmentation are done the same way as explained in section 3.

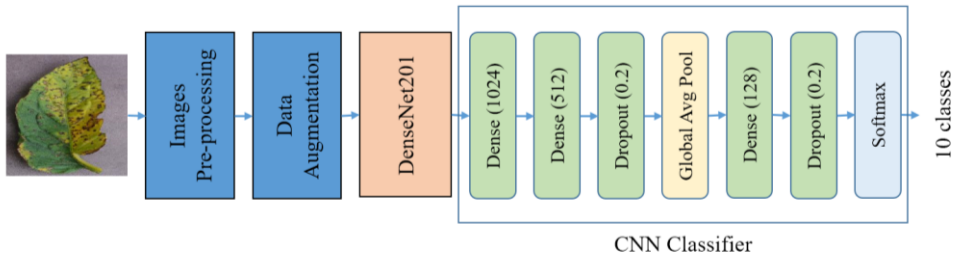

Fig. 6. The proposed model

In the third phase, the DenseNet201 model was proposed, which uses transfer learning to extract features automatically and leverage their weights learnt on the ImageNet dataset to reduce calculation workload. DenseNet201's architecture allows for the creation of simple and straightforward models. It's also feasible to reuse features across layers, making the architecture's parameters more efficient and allowing for more variation in subsequent layers and improved performance. The architecture connects each layer to all other layers in a feed-forward approach. Additionally, the DenseNet201 model uses a pooling layer and bottleneck structure. As a result, this architecture minimizes model complexity and property parameters, making it more efficient. Each layer of DenseNet201 network implements a nonlinear transformation, and the nonlinear transformation includes the convolution (Conv), pooling, rectified linear units (ReLU) and batch normalization (BN) (Huang, Liu & Weinberger, 2016). Unlike other networks, the output of each layer is used as the input for each subsequent layer in the Densenet201 network (i.e., X0, X1, X2, X3 and X4), so there are L(L+1)/2 connections in an L-layer DenseNet201 network (Huang, Liu & Weinberger, 2016). In the current study, the DenseNet201 architecture contains 707 layers and about 20 million parameters. The numbers of parameters of different models used in this study are shown in Table 3. The images dimensions in the input layer are set to 224 x 224 x 3. Fig.7 shows the architecture of DenseNet201.

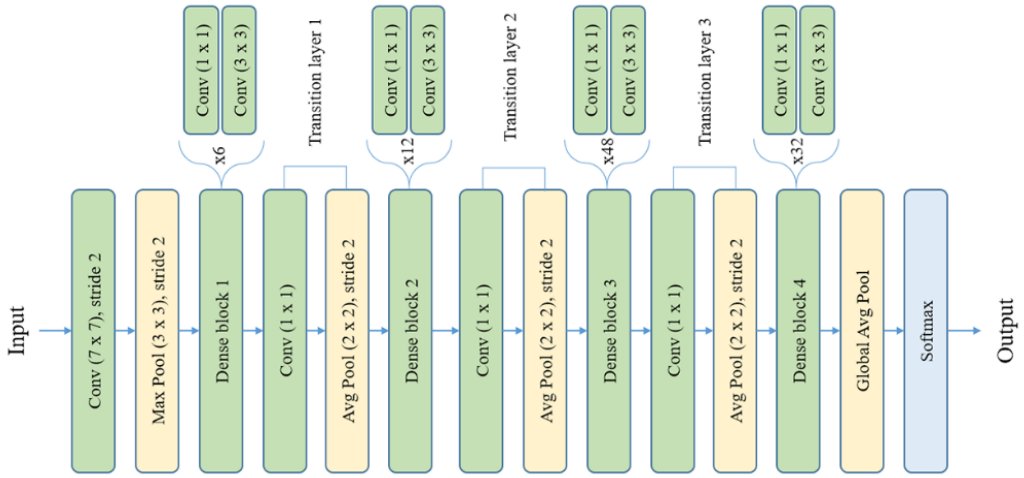

Fig. 7. DenseNet201 architecture

In the fourth phase, the classification output layers of the DenseNet201 network are removed in the fourth phase, and six layers for the classification task are proposed. Fig. 6 depicts the architecture of the suggested model based on DenseNet201. The first layer is a dense layer with 1024 neuron and a Rectified Linear Unit (ReLu) as an activation function. The second layer is also a dense layer with 512 neurons and activation ReLu. To avoid overfitting, the third layer is a dropout layer with a dropout rate of 0.2, which indicates that 20% of the neurons will output 0. The fourth layer is a global average pooling layer for size reduction of features maps. In the fifth layer is a dense layer with 128 neurons and activation ReLu. The sixth layer is a dropout layer with dropout rate 0.2. The last layer is a dense layer with 10 neurons and Softmax activation function. The last layer output the 10 classes of tomato diseases. In the following section, we go through the results of our proposed model in detail and compare it to other transfer learning-based models.

5. EXPERIMENTAL AND DISCUSSIONS

Our experiment is implemented using Jupyter Notebook (Jupyter.Org, 2021) which is an open-source web application. It has several algorithms' coding for both feature extraction and classification. Also, it includes code for data cleaning and transformation, numerical simulation, statistical modelling, data visualization, machine learning, and much more. The machine over which this research has been accomplished is having an NVIDIA GeForce RTX 2060 graphic card with dedicated 6.0 GB of RAM and 1920 CUDA Cores. Processor: Intel(R) Core(TM) i7-10750H CPU @ 2.60GHz. Memory: 16.0 GB.

In our experiment first: tomato leaves images from plantvillage dataset were resized into 224×224. Then the augmentation was performed. We used the weights of imagenet for saving time of training and getting higher accuracies (Huang, Liu & Weinberger, 2016). We used Adam optimizer, softmax activation function and batch size equals 32. Learning rate and other parameters was set to default values.

Then, we used four CNN models, VGG16, Inception V3, ResNet152V2 and DenseNet201, with transfer learning technique to classify tomato diseases and compare them with our proposed model. Fig. 8 shows the accuracy and loss of different models.

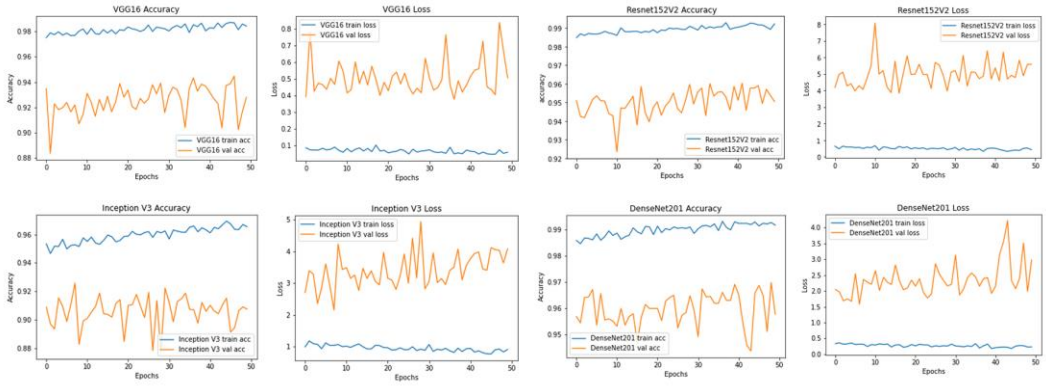

Fig. 8. Accuracy and loss of different models

Tab. 3. Results of different models

Model	Parameters (M)	Training Accuracy	Validation Accuracy	Loss	Val. Loss	Time/Step (Seconds)
VGG16	15	0.9869	0.9447	0.0466	0.4049	360.661
Inception V3	22.3	0.9560	0.9258	0.9437	2.1475	146.269
Resnet152V2	59.34	0.9909	0.9603	0.4428	4.5758	225.413
DenseNet201	19.30	0.9910	0.9698	0.3089	1.9804	164.300
Proposed Model	20.88	0.9932	0.9797	0.0230	0.0898	173.327

The results of these experiments are shown in Table 3. It shows that our proposed model has high accuracy. It achieved the highest training accuracy of 99.32 % and validation accuracy of 97.97 %.

The obtained results of the five models are analyzed to enhance the results. However, the architectures evaluation is made depending upon two parameters, validation accuracy and confusion matrix. The term validation accuracy defines how accurately the trained model is tracking the trained data. On the other hand, the sum of each column within a confusion matrix corresponds to the false positive rate (FP), and the false-negative rate (FN) for each class corresponds to each row's amount. The diagonal numbers represent the exact positive rate (TP), and the exact negative rate (TN) is the sum of all other diagonal numbers. Nevertheless, the formulas applied to measure accuracy, precision, recall, and F1 score of an architecture are as follows:

$$Accuracy = \frac{T_P + T_N}{T_P + T_N + F_P + F_N} \tag{1}$$

$$Precision = \frac{T_P}{T_P + F_P} \tag{2}$$

$$Recall = \frac{T_P}{T_P + F_N} \tag{3}$$

$$F1\_Score = \frac{2 \times Recall \times Precision}{Recall + Precision} \tag{4}$$

The classification accuracy is a standard performance measure used to evaluate the efficacy of the classifier. Where TP (true positive)-correctly classified positive samples, TN (true negative)-correctly classified negative samples, FP (false positive)-misclassified negative samples and FN (false negative)-misclassified positive samples.

Tab. 4. Accuracy, Precision, Recall and F1 score for different models

Model	Accuracy	Precision	Recall	F1 Score
VGG16	0.9447	0.94	0.93	0.93
Inception V3	0.9258	0.93	0.92	0.92
Resnet152V2	0.9603	0.95	0.95	0.95
DenseNet201	0.9698	0.96	0.96	0.96
Proposed Model	0.9797	0.97	0.97	0.97

To evaluate the efficiency of different models, performance parameters such as Classification Accuracy, Precision, Recall, F1-Score are calculated as shown in Table 4. Fig. 9 shows the accuracy and loss of the proposed model. Fig. 10 shows the confusion matrix for the accuracy of the performance of the test data for the classified 10 plant leaf diseases by using proposed model. The results of the test data set is nearly the same as the results of validation data set.

Since the DenseNet201 model achieved the highest accuracy in transfer learning classification among other models and other properties of DenseNet mentioned in section 4, we used it as the base transfer learning model for features extraction to build our proposed model for tomato disease identification. DenseNet201 model also has small number of training parameters in comparison with the Resnet152V2 model as shown in Table 3 which is giving also better accuracy and that affecting the size of the model and the training time.

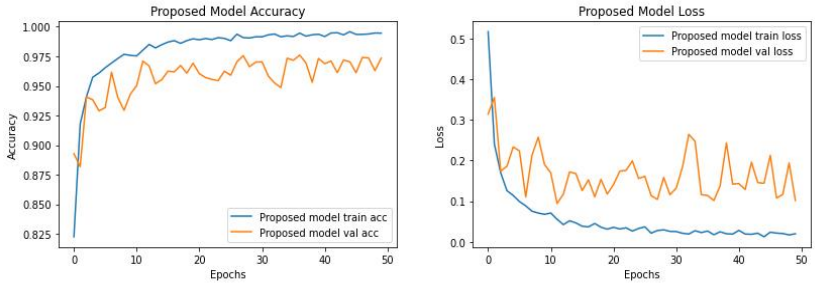

Fig. 9. Accuracy and loss of Proposed Model

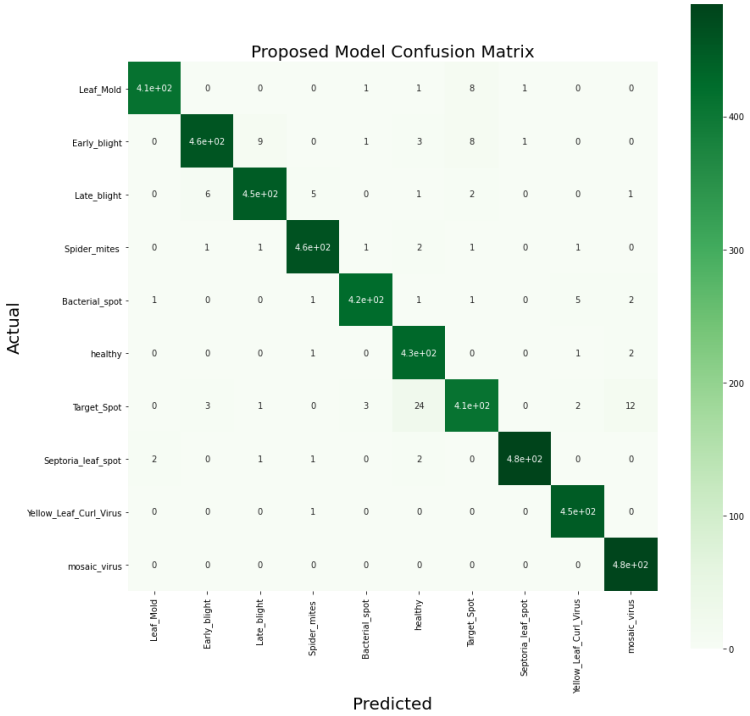

Fig. 10. Confusion matrix for proposed model

In our case, DenseNet201 contains 707 layers. One of the benefits of DenseNet201 model architecture is that we can train all layers or some layers or only the last level of layers. As we did in the first phase and get the results shown in Table 3. We did some fine-tuning by retraining about half layers of the DenseNet201 model layers – 300 layers – in the phase of features extraction and get better training accuracy of 99.84%, validation accuracy of 99.30% and testing accuracy of 99%, Training time per step: 190.349 second, validation loss: 0.0866. Table 5 shows the results of proposed model after retraining some layers.

Tab. 5. Proposed model performance values after training some layers of base model

Performance Metrics	Value
Training Accuracy	99.84%
Validation Accuracy	99.30%
Validation Loss	0.0866
Training time per step	190.349 seconds
Testing Accuracy	99.0%
Precision	0.99
Recall	0.99
F1 Score	0.99

6. CONCLUSION

In this paper, a comparison study has been conducted to find the best deep CNN model for using in plant leaves diseases detection. Four deep CNN models, DenseNet201, VGG16, Inception V3 and ResNet152V2 were trained and tested using the tomato leaf disease data set. Applying transfer learning technique to save time and effort in training these models. The data set was split into 75% for training, 20% for validation and 5% for testing, and were labelled with 10 different classes of diseased including healthy tomato leaves images. The results for each case are presented in Table 3. We also proposed a classification model based on DenseNet201 and transfer learning. In our proposed model the DenseNet201 model works as features extraction phase that followed by a CNN classifier. The results shows that the proposed model gives the highest accuracy. We apply additional fine-tuning by training some additional layers of the model during transfer learning not only the last level of layers. Finally, the results show that: the parameters and the average accuracy of the five convolutional neural networks are different. Our proposed model gives the highest accuracy.

In future work, we plan to expand our research with other pre-trained CNNs to solve multi-classification tasks. Apply our proposed model to more plants and diseases. Build a plant disease diagnosis application that help the farmers in Egypt.

REFERENCES

Afifi, A., Alhumam, A., & Abdelwahab, A. (2021). Convolutional Neural Network for Automatic Identification of Plant Diseases with Limited Data. *Plants*, *10*(1), 28. https://doi.org/10.3390/plants10010028

Agarwal, M., Singh, A., Arjaria, S., Sinha, A., & Gupta, S. (2020). ToLeD: Tomato Leaf Disease Detection using Convolution Neural Network. *Procedia Computer Science*, *167*, 293–301. https://doi.org/10.1016/j.procs.2020.03.225

Chen, J., Chen, J., Zhang, D., Sun, Y., & Nanehkaran, Y. A. (2020). Using deep transfer learning for image-based plant disease identification. *Computers and Electronics in Agriculture*, *173*, 105393. https://doi.org/10.1016/j.compag.2020.105393

Gulli, A., & Pal, S. (2017). *Deep Learning with Keras*. Packt.

Hong, H., Lin, J., & Huang, F. (2020). Tomato Disease Detection and Classification by Deep Learning. In *2020 International Conference on Big Data, Artificial Intelligence and Internet of Things Engineering (ICBAIE)* (pp. 25–29). IEEE. https://doi.org/10.1109/ICBAIE49996.2020.00012

Huang, G., Liu, Z., & Weinberger, K. Q. (2016). Densely Connected Convolutional Networks. *CoRR*, *abs/1608.06993*. http://arxiv.org/abs/1608.06993

Ji, M., Zhang, L., & Wu, Q. (2020). Automatic grape leaf diseases identification via UnitedModel based on multiple convolutional neural networks. *Information Processing in Agriculture*, *7*(3), 418–426. https://doi.org/10.1016/j.inpa.2019.10.003

Jupyter.org. (2021). https://jupyter.org

Kabir, M. M., Ohi, A. Q., & Mridha, M. F. (2020). A Multi-Plant Disease Diagnosis Method using Convolutional Neural Network. *CoRR*, *abs/2011.05151*. https://arxiv.org/abs/2011.05151

Kaggle. (2018). https://www.kaggle.com/noulam/tomato/download

Kumar, V., Arora, H., Harsh, & Sisodia, J. (2020). ResNet-based approach for Detection and Classification of Plant Leaf Diseases. In *2020 International Conference on Electronics and Sustainable Communication Systems (ICESC)* (pp. 495–502). IEEE. https://doi.org/10.1109/ICESC48915.2020.9155585

Mohamed, A., Abdel-Gaber, S., Nasr, M., & Hazman, M. (2020). An Intelligent Approach to Mitigate Effects of Climate Change and Insects on Crops. *International Journal of Computer Science and Information Security (IJCSIS)*, *18*(3), 75–79.

Peyal, H. I., Shahriar, S. M., Sultana, A., Jahan, I., & Mondol, Md. H. (2021). Detection of Tomato Leaf Diseases Using Transfer Learning Architectures: A Comparative Analysis. In *2021 International Conference on Automation, Control and Mechatronics for Industry 4.0 (ACMI)* (pp. 1–6). IEEE. https://doi.org/10.1109/ACMI53878.2021.9528199

Plant health and food security. (2017). *FAO*. http://www.fao.org/3/a-i7829e.pdf

Rangarajan, A. K., Purushothaman, R., & Ramesh, A. (2018). Tomato crop disease classification using pre-trained deep learning algorithm. *Procedia Computer Science*, *133*, 1040–1047. https://doi.org/10.1016/j.procs.2018.07.070

Saleem, M. H., Potgieter, J., & Arif, K. M. (2019). Plant Disease Detection and Classification by Deep Learning. *Plants*, *8*(11), 468. https://doi.org/10.3390/plants8110468

Shorten, C., & Khoshgoftaar, T. M. (2019). A survey on Image Data Augmentation for Deep Learning. *Journal of Big Data*, *6*(1), 60. https://doi.org/10.1186/s40537-019-0197-0

Simonyan, K., & Zisserman, A. (2015). Very Deep Convolutional Networks for Large-Scale Image Recognition. In Y. Bengio & Y. LeCun (Eds.), *3rd International Conference on Learning Representations, ICLR 2015, San Diego, CA, USA, May 7-9, 2015, Conference Track Proceedings*. http://arxiv.org/abs/1409.1556

Szegedy, C., Vanhoucke, V., Ioffe, S., Shlens, J., & Wojna, Z. (2016). Rethinking the Inception Architecture for Computer Vision. In *2016 IEEE Conference on Computer Vision and Pattern Recognition (CVPR)* (pp. 2818–2826). IEEE. https://doi.org/10.1109/CVPR.2016.308

Too, E. C., Yujian, L., Njuki, S., & Yingchun, L. (2019). A comparative study of fine-tuning deep learning models for plant disease identification. *Computers and Electronics in Agriculture*, *161*, 272–279. https://doi.org/10.1016/j.compag.2018.03.032

Venkatesh, Nagaraju, Y., Sahana, T. S., Swetha, S., & Hegde, S. U. (2020). Transfer Learning based Convolutional Neural Network Model for Classification of Mango Leaves Infected by Anthracnose. In *2020 IEEE International Conference for Innovation in Technology (INOCON)* (pp. 1–7). IEEE. https://doi.org/10.1109/INOCON50539.2020.9298269

Applied Computer Science, vol. 18, no. 2, pp. 71–85
doi: 10.35784/acs-2022-14

Submitted: 2022-05-31 | Revised: 2022-06-23 | Accepted: 2022-06-27

Keywords: acoustic emission, machine learning, osteoarthritis, knee joint, kinetic chain

Robert KARPIŃSKI [0000-0003-4063-8503]*, **

KNEE JOINT OSTEOARTHRITIS DIAGNOSIS BASED ON SELECTED ACOUSTIC SIGNAL DISCRIMINANTS USING MACHINE LEARNING

Abstract

This paper presents the results of a preliminary study on simplified diagnosis of osteoarthritis of the knee joint based on generated vibroacoustic processes. The analysis was based on acoustic signals recorded in a group of 50 people, half of whom were healthy, and the other half – people with previously confirmed degenerative changes. Selected discriminants of the signals were determined and statistical analysis was performed to allow selection of optimal discriminants used at a later stage as input to the classifier. The best results of classification using artificial neural networks (ANN) of RBF (Radial Basis Function) and MLP (Multilevel Perceptron) types are presented. For the problem involving the classification of cases into one of two groups HC (Healthy Control) and OA (Osteoarthritis) an accuracy of 0.9 was obtained, with a sensitivity of 0.885 and a specificity of 0.917. It is shown that vibroacoustic diagnostics has great potential in the non-invasive assessment of damage to joint structures of the knee.

1. INTRODUCTION

The knee joint is the largest and one of the most complex joints in the human body. During everyday activities, it is exposed to significant loads, often several times the weight of the human body, which makes it extremely vulnerable to injury and the possibility of osteoarthritis (Arendt, Miller & Block, 2014; Będziński, 1997; Krakowski, Karpiński, Maciejewski & Jonak, 2021). It is one of the most susceptible to the loss of articular cartilage and, as a result, to the development of degenerative changes in the joints of the human body (Cross et al., 2014; Krakowski, Gerkowicz, et al., 2019; Kyu et al., 2018). Osteoarthritis is a clinical syndrome characterized by progressive degeneration of articular cartilage that may involve the entire joint, including synovial membranes and fragments of subchondral bone (Befrui et al., 2018; Krakowski, Karpiński, Jonak & Maciejewski, 2021; Krishnan et al., 2000). It is now one of the most common causes of pain and disability in middle-aged and elderly people and a major cause of impairment of activities of daily living (Hunter & Bierma-

* Department of Machine Design and Mechatronics, Faculty of Mechanical Engineering, Lublin University of Technology, Lublin, Poland, r.karpinski@pollub.pl
** Department of Psychiatry, Psychotherapy, and Early Intervention, Medical University of Lublin, Lublin, Poland, robertkarpinski@umlub.pl

Zeinstra, 2019; McDonough & Jette, 2010). The incidence of osteoarthritis is influenced by a number of factors such as work, sports, musculoskeletal injuries, obesity and gender (Felson, 2004; Johnson & Hunter, 2014; Krakowski, Karpiński, Maciejewski, Jonak & Jurkiewicz, 2020; Krakowski, Karpiński, Jojczuk, Nogalska & Jonak, 2021; Reyes et al., 2015).

Non-invasive diagnosis of knee osteoarthritis is most often carried out based on physical examination and typical imaging techniques such as radiography (X-ray) (Hayashi, Roemer & Guermazi, 2019; Richette & Latourte, 2019), computed tomography (CT) (Ahn & El-Khoury, 2006), magnetic resonance imaging (MRI) (Krakowski, Nogalski, Jurkiewicz, Karpiński, Maciejewski & Jonak, 2019) and also ultrasound (US) (Mathiessen et al., 2016; Möller et al., 2008). Invasive methods include arthroscopy of the joint during which intraoperative assessment is performed, but this procedure carries a risk of complications as with any surgery. The main limitations of diagnostic imaging for the assessment of osteo-arthritis undoubtedly include the low sensitivity of detecting lesions at an early stage of their (Krakowski, Nogalski, et al., 2019) and the limited accessibility especially for patients living in smaller towns. These methods are also associated with high costs related to the use of specialized equipment and the need to employ highly qualified staff. Considering the above facts, it seems extremely important to develop an inexpensive, non-invasive method of assessing damage to joint structures, allowing diagnostics to be performed in the orthopedic office during routine examinations.

An alternative to the currently used methods may be vibroacoustic diagnostics. This method is widely used in non-invasive diagnostics of machines where it gives very good results (Figlus, Kozioł & Kuczyński, 2019; Jedliński et al., 2015; Jedliński & Jonak, 2015). For the diagnosis of the knee joint, this method was first proposed by Blodgett in 1902 (Blodgett, 1902). Depending on the efficiency of lubrication, the joint systems generate vibrations and noises. The same is true for the knee joint and other joints in the human body. Changes in the mechanical properties and surface structure of the articular cartilage, such as the appearance of bumps, cracks or cartilage defects in the successive stages of degenerative changes, influence the vibroacoustic signals recorded during movement of the knee joint (Karpiński, Machrowska & Maciejewski, 2019; Prior et al., 2010; van den Borne et al., 2007). Fig. 1 shows images taken during arthroscopy of the knee showing healthy (a) and degenerated (b) articular cartilage. Analysis of the differences in the characteristic parameters of the recorded signals may allow for a preliminary assessment of the condition of the joint and allow for accelerated diagnosis and selection of an appropriate therapy. In addition, this method provides information about the mutual cooperation of intra- and extra-articular structures of the moving joint, in most other cases we obtain information about the joint in a static position (Kernohan et al., 1990; Rangayyan & Wu, 2008; Walters, 1929; Wu, 2015). The application of machine learning methods can be extremely useful in the analysis of issues related to non-invasive diagnosis of articular cartilage damage based on vibroacoustic signals.

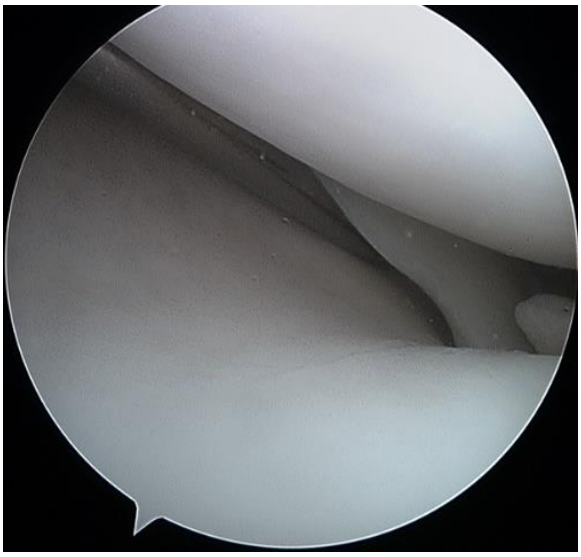

(a)

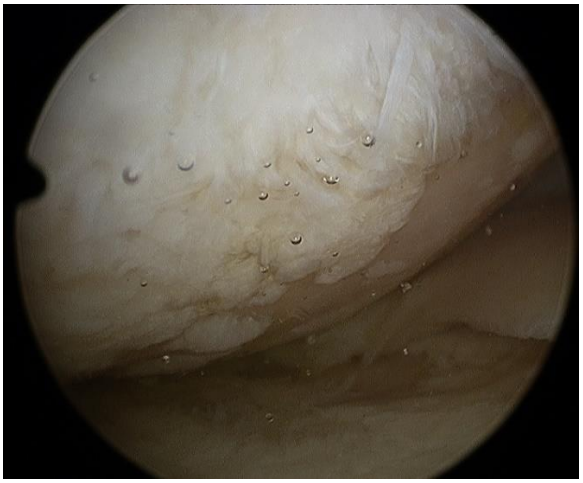

(b)

Fig. 1. Arthroscopic images of healthy (a) and degenerated (b) articular cartilage

The purpose of this study is to evaluate the usefulness of selected discriminants determined for acoustic signals generated in the knee joint, recorded in the control group (healthy subjects) and the study group (confirmation of degenerative changes), in the diagnosis of cartilage damage of the knee joint using machine learning.

2. MATERIALS AND METHODS

2.1. Participants and study protocol

The study was conducted on a group of 50 volunteers, half of whom were healthy people (HC group) and the other half, people previously qualified by an orthopedic surgeon, for surgery including arthroscopy or total knee replacement due to the presence of degenerative changes in the knee joint. All surgeries were performed by a surgeon specializing in TKR or arthroscopy according to a standard protocol depending on the type of surgery. During surgery, the extent of cartilage damage and the location of cartilage damage were accurately assessed. The International Cartilage Repair Society (ICRS) scale was used to assess cartilage (Brittberg & Winalski, 2003; Cameron, Briggs & Steadman, 2003). The control group, on the other hand, consisted of people without any complaints occurring in the knee joints. Signal recording in this group was carried out in laboratory conditions in the premises of the Lublin University of Technology. In the case of the study group, the recording of signals took place in the conditions of the orthopaedic department on the day of admission to hospital preceding the surgery. The examination in both groups was preceded by physical tests and a questionnaire examination, allowing to determine the condition of the joint. The protocol was identical in both groups and was conducted by a specialist in orthopedics and traumatology of the musculoskeletal system. In the control group, the signal recorded for one randomly selected limb was analyzed, while in the case of subjects in the study group, the signal acquired from the limb qualified for surgery was analyzed. The whole procedure was conducted in accordance with the principles of good clinical practice and was approved by the bioethics committee of the Medical University of Lublin (consent no. KE-0254/261/2019). Details of the groups are summarized in Table 1.

Tab. 1. Characteristics of study participants

Study group	N	Males/ Females	Age (years ± SD)	Heigh (m ± SD)	Weight (kg ± SD)	BMI	Tegner-Lyshom score
Healthy control (HC)	25	9/16	25.04 ± 5.76	1.72 ± 0.09	68.00 ± 15.33	22.69 ± 2.98	100 ± 0.0
Osteoarthritis (OA)	25	9/16	61.40 ± 9.11	1.68 ± 0.08	90.84 ± 14.36	32.38 ± 4.82	34.00 ± 9.54

To record acoustic signals the author's measurement system was used, consisting of a microcontroller with peripheral devices for signal acquisition in the form of a CM01b piezoelectric microphone, a rotary encoder installed on a typical knee orthosis and a computer with software for signal recording. The signals were recorded with the microphone, while the encoder was used to measure the flexion angle and limb position. The sampling frequency was 1400 Hz and the resolution was 10 bits. Details of the measurement system are described in previous work (Karpiński, Machrowska & Maciejewski, 2019; Karpiński et al., 2022b). Signals were recorded for a closed kinetic chain (CKC) where standing up from a sitting position to full upright was realized. A movement in the range of 90° – 0° – 90° was considered as one cycle. The cycle duration was approximately 2s and depended on the individual predisposition of the patient. The measurement was conducted for ten complete cycles. The signals obtained in this way contained some artifacts including mainly the

registration of time series before and after cycles of movements, random noise, and electrical network disturbances. In order to remove these disturbances, the signals were subjected to a preprocessing procedure involving the removal of insignificant fragments of the time series before and after the analyzed movements. For this purpose, a procedure was used to semi-automatically remove irrelevant signal samples from the encoder data. A trend line was also removed from the signals using the EEMD procedure, which is described in more detail in the papers (Huang et al., 1998; Jonak et al., 2019; Karpiński et al., 2022b; Machrowska & Jonak, 2018; Wu, 2015). For the signals prepared in this way, selected discriminants were determined.

2.2. Feature extraction

In diagnostic practice it is very important to use simple discriminants of vibration acoustic signals, which are easy to determine and allow assessment of the type of damage present (Madej, Czech & Konieczny, 2003). An observable quantity associated with a technical condition may be classified in the group of diagnostic symptoms, provided that the relationships describing this phenomenon are determined (Stanik et al., 2013). The changes occurring in the observed signal in a unit of time take many instantaneous values, which often, due to the dynamics of changes, makes it impossible to observe each change of the instantaneous value in the analysis (Cempel, 2005; Stanik et al., 2013). However, it is important to define the values of signals describing the characteristic points of greatest importance for the overall signal analyzed. In this study, the following signal discriminants were determined for the analyzed acoustic signals:

1. Straightened average value (SA):

$$\bar{x} = \frac{1}{N}\sum_{i=1}^{N}|x_i| \tag{1}$$

where: x_i – the value of the discrete signal at the nth point, $n = 1, \dots, N$,
N – number of samples in the signal.

2. Root mean square (RMS):

$$x_{RMS} = \sqrt{\frac{1}{N}\sum_{i=1}^{N} {x_i}^2} \tag{2}$$

3. Peak value (PV):

$$\hat{x} = max|x_i| \tag{3}$$

4. Peak to peak value (PPV):

$$x_{PPV} = |x_{max} - x_{min}| \tag{4}$$

5. Crest Factor (CF):

$$x_{CF} = \frac{\hat{x}}{x_{RMS}} \tag{5}$$

6. Impact Factor (IF):

$$x_I = \frac{\hat{x}}{\bar{x}} \tag{6}$$

7. Shape factor (SF):

$$x_{SF} = \frac{x_{RMS}}{\bar{x}} \tag{7}$$

8. Variance (VAR):

$$x_{VAR}^2 = \frac{1}{N-1}\sum_{i=1}^{N}(x_i - \bar{x})^2 \tag{8}$$

9. Kurtosis (KUR):

$$x_{KUR} = \frac{\frac{1}{N}\sum_{i=1}^{N}(x_i-\bar{x})^4}{\left[\frac{1}{N}\sum_{i=1}^{N}(x_i-\bar{x})^2\right]^2} \tag{9}$$

A detailed description of the designated discriminants was presented in the author's previous work (Karpiński et al., 2021a, 2021b, 2022a, 2022b) and other studies (Jedliński & Jonak, 2020; Stanik i in., 2013).

2.3. Statistical Analysis

Statistical analysis to determine whether there were statistically significant differences between the determined signal discriminants for signals recorded in the HC and OA groups was performed using Statistica 13.3. The significance level was taken as $\alpha = 0.05$.

The first step in the analysis was to test whether the values of the individual discriminants of the acoustic signals in the both groups have a normal distribution. For this purpose, three tests were performed: Kolmogorov-Smirnov test, Lilliefors test and Shapiro-Wilk test (Karpiński, Szabelski & Maksymiuk, 2019a; Rabiej, 2018; Szabelski, 2018).

Analysis of equality of variance was performed using three tests: F (Fisher's), Levene's, and Brown and Forsyth. For results characterized by normality of distribution and equality of variance – Student's t-test was used to analyze the equality of the resulting means of individual signal discriminants, at the assumed level of significance. For the results characterized by normality of distribution but lack of equality of variance – to analyze the equality of mean values of signal discriminants we used Student's t-test with separate variance estimation (Cochran-Cox test) (Karpiński, Szabelski & Maksymiuk, 2019b; Rabiej, 2018). For discriminants that did not have a normal distribution, the Mann-Whitney U test with a continuity correction was used. This correction is used to ensure that the test statistic can accommodate all real number values as assumed by the normal distribution. Discriminants showing statistically significant differences were determined from the analyses and were used as inputs to the neural classifiers.

2.4. Machine learning

Machine learning (ML) is a subset of artificial intelligence (AI). It is an area devoted to algorithms whose performance improves automatically based on collected experience, or exposure to data. A subset of machine learning is deep learning (DL), within which are artificial neural networks (ANNs) (Machrowska, Karpiński, et al., 2020; Machrowska,

Szabelski, et al., 2020). A neural network is a collection of appropriately connected neurons arranged in layers. Artificial neural networks are one type of highly parameterized statistical models. They have been developed based on information about the functioning of the nervous system of living organisms and are capable of mapping extremely complex functions (Bauer, Stütz & Kley, 2021; Dudek-Dyduch, Tadeusiewicz & Horzyk, 2009; Tadeusiewicz, 1993). Technically, an artificial neuron is an element whose properties correspond to selected properties of its biological counterpart. Each neuron has at least one input and one output. The signals at the inputs are multiplied by factors referred to as synaptic weights. Each neuron calculates a weighted sum of its inputs, which are then summed. The activation level determined in this way becomes the argument of the transition function (activation function), which calculates the output of the neuron. The values of weights can be changed, which allows the network to learn and adapt to the problem being solved. ANNs find application in solving problems related to data processing and analysis, prediction and classification especially when the analyzed issues involve poorly known phenomena and processes (Badurowicz, 2022; Kosicka, Krzyzak, Dorobek & Borowiec, 2022; Rogala, 2020; Szabelski, Karpiński & Machrowska, 2022).

In the analyzed problem classification was carried out using the Statistica 13.3 package (Tulsa, OK, USA), which includes modules covering machine learning and artificial neural networks. A built-in algorithm was used to automatically search for multilevel perceptron (MLP) and radial basis function (RBF) neural networks with the best possible parameters. Acoustic signal discriminants that had statistically significant differences between the study groups in the statistical analysis were used as input data. The data were randomly divided 70% for training, 15% for testing and 15% for validation. The outputs of the neural networks, on the other hand, proposed a simplified partitioning that allowed assigning the cases to one of the two groups OA and HC. Results for sets of the three best MLP and RBF networks are presented. The parameters for automatic design of MLP and RBF neural networks in Statistica software are shown in Figure 2.

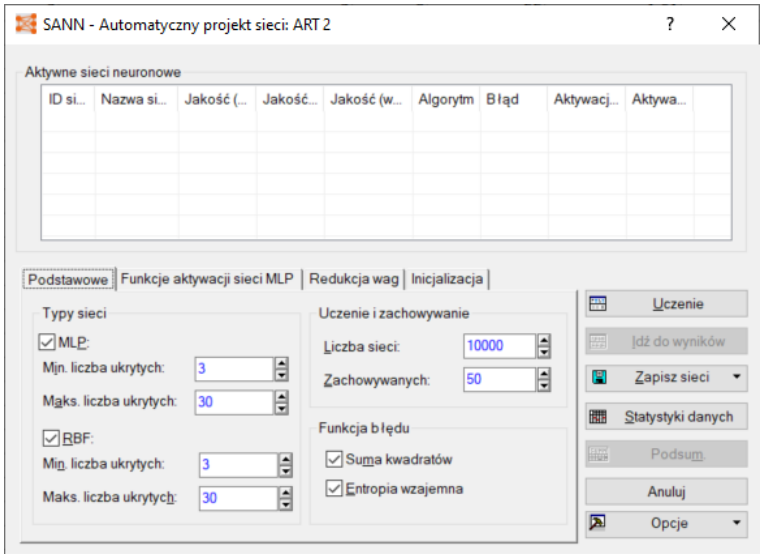

Fig. 2. The parameters for automatic design of MLP and RBF neural networks

3. RESULTS

3.1. Statistical analysis

Checking whether the values of individual discriminants of acoustic signals have normal distribution was carried out using Kolmogorov-Smirnov test, Lilliefors test and Shapiro-Wilk test. The results of the performed analyses are summarized in Table 2. The following hypotheses were assumed in the analysis:

H_0 – Variables within the analyzed groups have normal distribution.

H_1 – Variables within the analyzed groups do not have normal distribution.

Tab. 2. Results of statistical analysis to test the normality of distribution

Discriminant	Study group	N	maks D	K-S	Lillief.	W	p
Straightened average value (SA)	OA	25	0.168	p > .20	p < .10	0.932	0.098
Root mean square (RMS)	OA	25	0.159	p > .20	p < .15	0.942	0.165
Peak value (PV)	OA	25	0.266	p < .10	**p < .01**	**0.773**	**0.000**
Peak to peak value (PPV)	OA	25	0.192	p > .20	**p < .05**	**0.838**	**0.001**
Crest Factor (CF)	OA	25	0.275	**p < .05**	**p < .01**	**0.804**	**0.000**
Impact Factor (IF)	OA	25	0.226	p < .15	**p < .01**	**0.753**	**0.000**
Shape factor (SF)	OA	25	0.314	**p < .05**	**p < .01**	**0.569**	**0.000**
Variance (VAR)	OA	25	0.165	p > .20	p < .15	0.934	0.105
Kurtosis (KUR)	OA	25	0.214	p < .20	**p < .01**	**0.889**	**0.010**
Straightened average value (SA)	HC	25	0.104	p > .20	p > .20	0.986	0.973
Root mean square (RMS)	HC	25	0.134	p > .20	p > .20	0.961	0.428
Peak value (PV)	HC	25	0.235	p < .15	**p < .01**	**0.789**	**0.000**
Peak to peak value (PPV)	HC	25	0.266	p < .10	**p < .01**	**0.524**	**0.000**
Crest Factor (CF)	HC	25	0.190	p > .20	**p < .05**	**0.782**	**0.000**
Impact Factor (IF)	HC	25	0.309	**p < .05**	**p < .01**	**0.522**	**0.000**
Shape factor (SF)	HC	25	0.326	**p < .01**	**p < .01**	**0.454**	**0.000**
Variance (VAR)	HC	25	0.110	p > .20	p > .20	0.964	0.500
Kurtosis (KUR)	HC	25	0.166	p > .20	p < .10	**0.813**	**0.000**

On the basis of the analyses performed, it can be concluded that in the case of discriminants such as Straightened average value (SA), Root mean square (RMS) and Variance (VAR), there are no grounds to reject the hypothesis of normality of distribution, because for these variables for the W Shapiro-Wilk test obtained levels of $p > \alpha = 0.05$. In the case of other discriminants, the results obtained give grounds to reject the hypothesis of normality of distribution and assume that these discriminants do not have normal distribution. The next step in the analyses conducted for discriminants having a normal distribution was to conduct an analysis of equality of variance using three tests: F (Fisher's), Levene, and Brown and Forsyth. Depending on the results of equality of variance analysis, the analysis of equality of means was conducted using Student's t-test (in case of equality of variance) and Student's t-test with separate variance estimation (in case of non-equality of variance). The results of the analyses of equality of variance and equality of means are presented in Table 3.

Tab. 3. Results of Student's t-test and Student's t-test with the separate estimation of variance

Discriminant	Mean OA	Mean HC	t	p	t sep.	p	Standard deviation	Standard deviation	F quotient	p	Levene's	p	Brn-Fors	p
Straightened average value (SA)	119.96	224.50	-5.66	0.00	-5.66	0.000	65.72	64.99	1.02	0.957	0.133	0.717	0.118	0.733
Root mean square (RMS)	157.24	263.53	-5.04	0.00	-5.04	0.000	74.75	74.27	1.01	0.975	0.120	0.731	0.062	0.804
Variance (VAR)	25919.25	59888.86	-6.19	0.00	-6.19	0.000	17297.74	21301.67	1.52	0.314	0.743	0.393	0.646	0.426

The results obtained show that the mean values for individual discriminants have statistically significant differences between HC and OA groups. In the analyzed case, all discriminants were characterized by equality of variance, so the results of Student's t-test were taken into account in the analysis of equality of means.

For discriminants that did not have a normal distribution, the analyses used the Mann-Whitney U test with continuity correction. The results obtained are presented in Table 4. On the basis of Mann-Whitney U-test it can be stated that in case of discriminants such as Peak value (PV) ($p = 0.004$), Peak to peak value (PPV) ($p = 0.008$), Crest Factor (CF) ($p = 0.000$) and Kurtosis (KUR) ($p = 0.000$) between the tested groups there are statistically significant differences on the assumed significance level. These differences were not found for discriminants such as Impact Factor (IF) ($p = 0.535$) and Shape factor (SF) ($p = 0.561$), due to the lack of statistically significant differences these discriminants were not included in further considerations.

Tab. 4. Mann-Whitney U test results

Discriminant	Sum of ranks	Sum of ranks	U	Z	p	2*1str.
Peak value (PV)	488.00	787.00	163.00	**-2.89**	**0.004**	**0.003**
Peak to peak value (PPV)	501.00	774.00	176.00	**-2.64**	**0.008**	**0.008**
Crest Factor (CF)	873.00	402.00	77.00	**4.56**	**0.000**	**0.000**
Impact Factor (IF)	605.00	670.00	280.00	-0.62	0.535	0.538
Shape factor (SF)	607.00	668.00	282.00	-0.58	0.561	0.564
Kurtosis (KUR)	899.00	376.00	51.00	**5.06**	**0.000**	**0.000**

3.2. Classification

The results for the most accurate classifiers proposed by the automatic neural network selection algorithm of the Statistica package are presented below, three cases each for multilayer perceptron (MLP) and radial basis function (RBF) networks. Seven discriminants having statistically significant differences between the analyzed groups were used as input data, viz: Straightened average value (SA), Root mean square (RMS), Variance (VAR), Peak

value (PV), Peak to peak value (PPV), Crest Factor (CF), Kurtosis (KUR). The detailed results of learning, testing and validation accuracy for each network in all analyzed variants are shown in Table 5.

Tab. 5. Accuracy of learning, testing and validation for selected MLP and RBF neural networks

Network name	Accuracy (learning) %	Accuracy (testing) %	Accuracy (validation) %	Learning algorithm	Error function	Activation (hidden)	Activation (output)
MLP 7-22-2	88.89	100.00	85.71	BFGS 10	Entropy	Tanh	Softmax
MLP 7-10-2	88.89	100.00	85.71	BFGS 14	Entropy	Tanh	Softmax
MLP 7-7-2	83.33	100.00	85.71	BFGS 14	Entropy	Exponential	Softmax
RBF 7-9-2	88.89	85.71	85.71	RBFT	Entropy	Gauss	Softmax
RBF 7-10-2	86.11	85.71	85.71	RBFT	Entropy	Gauss	Softmax
RBF 7-5-2	83.33	85.71	85.71	RBFT	Entropy	Gauss	Softmax

The highest learning accuracy of 88.89% was observed for MLP 7-22-2, MLP 7-10-2 and RBF 7-9-2, while the lowest accuracy of 83.33% was observed for MLP 7-7-2 and RBF 7-5-2, respectively. In the case of testing accuracy, all MLP networks scored 85.71% while RBF networks scored 85.71%. The validation accuracy was identical for all the networks presented and was 85.71% respectively.

Information on the classification results for each group and all cases is shown in Table 6. The highest classification accuracy of 90% was obtained for MLP-type networks having 10 and 22 neurons in the hidden layer, respectively. For the best RBF-type network, the obtained classification accuracy was slightly lower than that of MLP-type networks at 88%. The obtained results show that both networks of multilayer perceptron type and networks with radial basis functions perform well in the analyzed problem and give comparable results of classification accuracy.

Tab. 6. Summary of classification accuracy of MLP and RBF

Network name		HC	OA	Total
MLP 7-22-2	Total	25.00	25.00	50.00
	Correct	23.00	22.00	45.00
	Correct (%)	92.00	88.00	90.00
MLP 7-10-2	Total	25.00	25.00	50.00
	Correct	22.00	23.00	45.00
	Correct (%)	88.00	92.00	90.00
MLP 7-7-2	Total	25.00	25.00	50.00
	Correct	21.00	22.00	43.00
	Correct (%)	84.00	88.00	86.00
RBF 7-9-2	Total	25.00	25.00	50.00
	Correct	23.00	21.00	44.00
	Correct (%)	92.00	84.00	88.00
RBF 7-10-2	Total	25.00	25.00	50.00
	Correct	21.00	22.00	43.00
	Correct (%)	84.00	88.00	86.00
RBF 7-5-2	Total	25.00	25.00	50.00
	Correct	21.00	21.00	42.00
	Correct (%)	84.00	84.00	84.00

There are many tools to assess the validity of classifiers among others are ROC curves, and metrics such as F1-score and Matthews correlation coefficient (MCC). ROC curves are a visualization of the relationship between the effectiveness of positive classifiers (sensitivity) and the ineffectiveness of negative case classification (1-specificity) at each probability level. A detailed summary of the performance of each classifier is shown in Table 7. The highest AUC value of 0.941 was obtained for the MLP 7-10-2 network with a sensitivity of 0.917 and a specificity of 0.885. For the RBF-type network, the highest value of 0.931 was obtained for the network with 9 neurons in the hidden layer with a sensitivity of 0.852 and a specificity of 0.913. A summary of the ROC curves for all the proposed classifiers is shown in Figure 3.

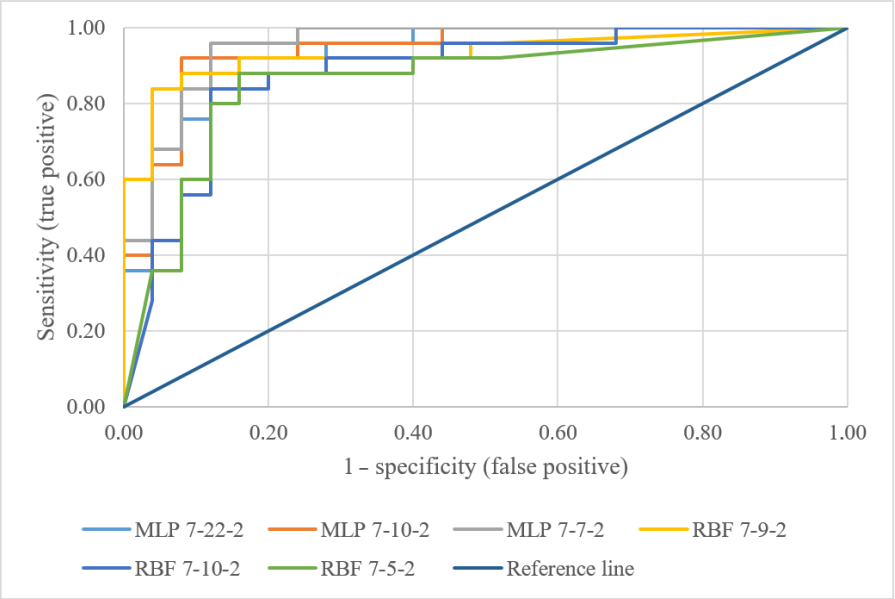

Fig. 3. Comparison of ROC curves for selected classifiers.

Tab. 7. Performance comparison of selected MLP and RBF classifiers

Network name	Sensitivity	Specificity	AUC	ROC Treshold	Accuracy	Precision	Recall	F1 score	MCC
MLP 7-22-2	0.885	0.917	0.933	0.564	0.900	0.920	0.885	0.902	0.801
MLP 7-10-2	0.917	0.885	0.941	0.485	0.900	0.880	0.917	0.898	0.801
MLP 7-7-2	0.875	0.846	0.954	0.490	0.860	0.840	0.875	0.857	0.721
RBF 7-9-2	0.852	0.913	0.931	0.563	0.880	0.920	0.852	0.885	0.762
RBF 7-10-2	0.875	0.846	0.881	0.285	0.860	0.840	0.875	0.857	0.721
RBF 7-5-2	0.840	0.840	0.860	0.556	0.840	0.840	0.840	0.840	0.680

In order to further compare the proposed classifiers, measures such as F1 score and Matthews correlation coefficient (MCC) were determined. F1 score is a measure of model precision on a dataset and it is most commonly used in evaluating binary classification systems. It is a way to combine model precision and recall. It is defined as the harmonic mean of model precision and recall (Chicco & Jurman, 2020). In contrast, the Matthews

correlation coefficient is one of the most informative single parameters for determining the prediction quality of a binary classifier in the context of a confusion matrix. It can be used even in cases where two classes have very different counts (Matthews, 1975; Powers, 2020).

The highest F1 score of 0.902 was obtained for the MLP-type network with twenty-two neurons in the hidden layer at a precision of 0.920 and recall of 0.885, while the lowest value of 0.840 was obtained for the RBF-type network with five neurons in the hidden layer at a precision and recall of 0.840. In the case of MCC, the highest value of 0.801 was obtained for the MLP-type network with twenty-two and ten neurons in the hidden layer, respectively, while the lowest value of 0. 680 as in the case of the F1 index was obtained for the RBF7-5-2 network. Detailed results for the parameters of the individual classifiers are presented in Table 7. The results obtained show that both multilayer perceptron (MLP) type networks and networks with radial basis functions give good results for the analyzed problem with a slight advantage of MLP type networks in most of the analyzed parameters of the classifiers studied.

A limitation of this study is undoubtedly the use of a simplified classification model, involving the assignment of results to two groups. To the limitations should also be added the fact of large differences in personal characteristics between the analyzed groups.

Further studies are planned, including the development of a method to precisely determine the degree of damage according to the ICRS scale and the approximate location of degenerative changes.

4. CONCLUSIONS

The obtained results confirm the effectiveness of the proposed method for diagnosing articular cartilage damage, which involves the selection of optimal discriminants of acoustic signals recorded for knee joints based on the results of statistical analyses and subsequent classification using artificial neural networks such as MLP and RBF. Vibroacoustic assessment may be a cheap and non-invasive alternative to typical imaging diagnostic methods, which will complement the physical examination performed during a standard visit at an orthopedic clinic.

REFERENCES

Ahn, J. M., & El-Khoury, G. Y. (2006). Computed Tomography of Knee Injuries. *Imaging Decisions MRI*, *10*(1), 14–23. https://doi.org/10.1111/j.1617-0830.2006.00063.x

Arendt, E. A., Miller, L. E., & Block, J. E. (2014). Early knee osteoarthritis management should first address mechanical joint overload. *Orthopedic Reviews*, *6*(1). https://doi.org/10.4081/or.2014.5188

Badurowicz, M. (2022). Detection of source code in internet texts using automatically generated machine learning models. Applied Computer Science. *Applied Computer Science*, *18*(1), 89–98. https://doi.org/10.23743/acs-2022-07

Bauer, L., Stütz, L., & Kley, M. (2021). Black box efficiency modelling of an electric drive unit utilizing methods of machine learning. *Applied Computer Science*, *17*(4), 5–19. https://doi.org/10.23743/acs-2021-25

Będziński, R. (1997). *Biomechanika inżynierska: Zagadnienia wybrane*. Oficyna Wydawnicza Politechniki Wrocławskiej.

Befrui, N., Elsner, J., Flesser, A., Huvanandana, J., Jarrousse, O., Le, T. N., Müller, M., Schulze, W. H. W., Taing, S., & Weidert, S. (2018). Vibroarthrography for early detection of knee osteoarthritis using normalized frequency features. *Medical & Biological Engineering & Computing*, *56*(8), 1499–1514. https://doi.org/10.1007/s11517-018-1785-4

Blodgett, W. E. (1902). Auscultation of the Knee Joint. *The Boston Medical and Surgical Journal*, *146*(3), 63–66. https://doi.org/10.1056/NEJM190201161460304

Brittberg, M., & Winalski, C. S. (2003). Evaluation of cartilage injuries and repair. *The Journal of Bone and Joint Surgery. American Volume*, *85-A Suppl 2*, 58–69.

Cameron, M. L., Briggs, K. K., & Steadman, J. R. (2003). Reproducibility and Reliability of the Outerbridge Classification for Grading Chondral Lesions of the Knee Arthroscopically. *The American Journal of Sports Medicine*, *31*(1), 83–86. https://doi.org/10.1177/03635465030310012601

Cempel, C. (2005). Diagnostyka wibroakustyczna maszyn-historia, stan obecny, perspektywy rozwoju. *Problemy Eksploatacji*, *3*, 7–25.

Chicco, D., & Jurman, G. (2020). The advantages of the Matthews correlation coefficient (MCC) over F1 score and accuracy in binary classification evaluation. *BMC Genomics*, *21*(1), 6. https://doi.org/10.1186/s12864-019-6413-7

Cross, M., Smith, E., Hoy, D., Nolte, S., Ackerman, I., Fransen, M., Bridgett, L., Williams, S., Guillemin, F., Hill, C. L., Laslett, L. L., Jones, G., Cicuttini, F., Osborne, R., Vos, T., Buchbinder, R., Woolf, A., & March, L. (2014). The global burden of hip and knee osteoarthritis: Estimates from the Global Burden of Disease 2010 study. *Annals of the Rheumatic Diseases*, *73*(7), 1323–1330. https://doi.org/10.1136/annrheumdis-2013-204763

Dudek-Dyduch, E., Tadeusiewicz, R., & Horzyk, A. (2009). Neural network adaptation process effectiveness dependent of constant training data availability. *Neurocomputing*, *72*(13-15), 3138–3149. https://doi.org/10.1016/j.neucom.2009.03.017

Felson, D. T. (2004). Obesity and vocational and avocational overload of the joint as risk factors for osteoarthritis. *The Journal of Rheumatology Supplement*, *70*, 2–5.

Figlus, T., Kozioł, M., & Kuczyński, Ł. (2019). The Effect of Selected Operational Factors on the Vibroactivity of Upper Gearbox Housings Made of Composite Materials. *Sensors*, *19*(19), 4240. https://doi.org/10.3390/s19194240

Hayashi, D., Roemer, F. W., & Guermazi, A. (2019). Imaging of Osteoarthritis by Conventional Radiography, MR Imaging, PET–Computed Tomography, and PET-MR Imaging. *PET Clinics*, *14*(1), 17–29. https://doi.org/10.1016/j.cpet.2018.08.004

Huang, N. E., Shen, Z., Long, S. R., Wu, M. C., Shih, H. H., Zheng, Q., Yen, N.-C., Tung, C. C., & Liu, H. H. (1998). The empirical mode decomposition and the Hilbert spectrum for nonlinear and non-stationary time series analysis. *Proceedings of the Royal Society of London. Series A: Mathematical, Physical and Engineering Sciences*, *454*(1971), 903–995.

Hunter, D. J., & Bierma-Zeinstra, S. (2019). Osteoarthritis. *The Lancet*, *393*(10182), 1745–1759. https://doi.org/10.1016/S0140-6736(19)30417-9

Jedliński, Ł., Caban, J., Krzywonos, L., Wierzbicki, S., & Brumerčík, F. (2015). Application of vibration signal in the diagnosis of IC engine valve clearance. *Journal of Vibroengineering*, *17*(1), 175–187.

Jedliński, Ł., & Jonak, J. (2015). Early fault detection in gearboxes based on support vector machines and multilayer perceptron with a continuous wavelet transform. *Applied Soft Computing*, *30*, 636–641. https://doi.org/10.1016/j.asoc.2015.02.015

Jedliński, Ł., & Jonak, J. (2020). *Kontrola montazu zebatych przekladni stozkowych metoda bezdemontazowa*. Wydawnictwo Politechniki Lubelskiej.

Johnson, V. L., & Hunter, D. J. (2014). The epidemiology of osteoarthritis. *Best Practice & Research Clinical Rheumatology*, *28*(1), 5–15. https://doi.org/10.1016/j.berh.2014.01.004

Jonak, J., Karpinski, R., Machrowska, A., Krakowski, P., & Maciejewski, M. (2019). A preliminary study on the use of EEMD-RQA algorithms in the detection of degenerative changes in knee joints. *IOP Conference Series: Materials Science and Engineering*, *710*, 012037. https://doi.org/10.1088/1757-899X/710/1/012037

Karpiński, R., Krakowski, P., Jonak, J., Machrowska, A., Maciejewski, M., & Nogalski, A. (2021a). Analysis of differences in vibroacoustic signals between healthy and osteoarthritic knees using EMD algorithm and statistical analysis. *Journal of Physics: Conference Series*, *2130*(1), 012010. https://doi.org/10.1088/1742-6596/2130/1/012010

Karpiński, R., Krakowski, P., Jonak, J., Machrowska, A., Maciejewski, M., & Nogalski, A. (2021b). Estimation of differences in selected indices of vibroacoustic signals between healthy and osteoarthritic patellofemoral joints as a potential non-invasive diagnostic tool. *Journal of Physics: Conference Series*, *2130*(1), 012009. https://doi.org/10.1088/1742-6596/2130/1/012009

Karpiński, R., Krakowski, P., Jonak, J., Machrowska, A., Maciejewski, M., & Nogalski, A. (2022a). Diagnostics of Articular Cartilage Damage Based on Generated Acoustic Signals Using ANN-Part II: Patellofemoral Joint. *Sensors*, *22*(10). https://doi.org/10.3390/s22103765

Karpiński, R., Krakowski, P., Jonak, J., Machrowska, A., Maciejewski, M., & Nogalski, A. (2022b). Diagnostics of Articular Cartilage Damage Based on Generated Acoustic Signals Using ANN-Part I: Femoral-Tibial Joint. *Sensors*, *22*(6), 2176. https://doi.org/10.3390/s22062176

Karpiński, R., Machrowska, A., & Maciejewski, M. (2019). Application of acoustic signal processing methods in detecting differences between open and closed kinematic chain movement for the knee joint. *Applied Computer Science*, *15*(1), 36–48. https://doi.org/10.23743/acs-2019-03

Karpiński, R., Szabelski, J., & Maksymiuk, J. (2019a). Effect of Physiological Fluids Contamination on Selected Mechanical Properties of Acrylate Bone Cement. *Materials*, *12*(23), 3963. https://doi.org/10.3390/ma12233963

Karpiński, R., Szabelski, J., & Maksymiuk, J. (2019b). Seasoning Polymethyl Methacrylate (PMMA) Bone Cements with Incorrect Mix Ratio. *Materials*, *12*(19), 3073. https://doi.org/10.3390/ma12193073

Kernohan, W. G., Beverland, D. E., McCoy, G. F., Hamilton, A., Watson, P., & Mollan, R. A. B. (1990). Vibration arthrometry. *Acta Orthopaedica Scandinavica*, *61*(1), 70–79.

Kosicka, E., Krzyzak, A., Dorobek, M., & Borowiec, M. (2022). Prediction of Selected Mechanical Properties of Polymer Composites with Alumina Modifiers. *Materials*, *15*(3), 882. https://doi.org/10.3390/ma15030882

Krakowski, P., Gerkowicz, A., Pietrzak, A., Krasowska, D., Jurkiewicz, A., Gorzelak, M., & Schwartz, R. A. (2019). Psoriatic arthritis – new perspectives. *Archives of Medical Science*, *15*(3), 580–589. https://doi.org/10.5114/aoms.2018.77725

Krakowski, P., Karpiński, R., Jojczuk, M., Nogalska, A., & Jonak, J. (2021). Knee MRI Underestimates the Grade of Cartilage Lesions. *Applied Sciences*, *11*(4), 1552. https://doi.org/10.3390/app11041552

Krakowski, P., Karpiński, R., Jonak, J., & Maciejewski, R. (2021). Evaluation of diagnostic accuracy of physical examination and MRI for ligament and meniscus injuries. *Journal of Physics: Conference Series*, *1736*, 012027. https://doi.org/10.1088/1742-6596/1736/1/012027

Krakowski, P., Karpiński, R., Maciejewski, R., & Jonak, J. (2021). Evaluation of the diagnostic accuracy of MRI in detection of knee cartilage lesions using Receiver Operating Characteristic curves. *Journal of Physics: Conference Series*, *1736*, 012028. https://doi.org/10.1088/1742-6596/1736/1/012028

Krakowski, P., Karpiński, R., Maciejewski, R., Jonak, J., & Jurkiewicz, A. (2020). Short-Term Effects of Arthroscopic Microfracturation of Knee Chondral Defects in Osteoarthritis. *Applied Sciences*, *10*(23), 8312. https://doi.org/10.3390/app10238312

Krakowski, P., Nogalski, A., Jurkiewicz, A., Karpiński, R., Maciejewski, R., & Jonak, J. (2019). Comparison of Diagnostic Accuracy of Physical Examination and MRI in the Most Common Knee Injuries. *Applied Sciences*, *9*(19), 4102. https://doi.org/10.3390/app9194102

Krishnan, S., Rangayyan, R. M., Bell, G. D., & Frank, C. B. (2000). Adaptive time-frequency analysis of knee joint vibroarthrographic signals for noninvasive screening of articular cartilage pathology. *IEEE Transactions on Biomedical Engineering*, *47*(6), 773–783. https://doi.org/10.1109/10.844228

Kyu, H. H., Abate, D., Abate, K. H., Abay, S. M., Abbafati, C., Abbasi, N., Abbastabar, H., Abd-Allah, F., Abdela, J., Abdelalim, A., Abdollahpour, I., Abdulkader, R. S., Abebe, M., Abebe, Z., Abil, O. Z., Aboyans, V., Abrham, A. R., Abu-Raddad, L. J., Abu-Rmeileh, N. M. E., … Murray, C. J. L. (2018). Global, regional, and national disability-adjusted life-years (DALYs) for 359 diseases and injuries and healthy life expectancy (HALE) for 195 countries and territories, 1990–2017: A systematic analysis for the Global Burden of Disease Study 2017. *The Lancet*, *392*(10159), 1859–1922. https://doi.org/10.1016/S0140-6736(18)32335-3

Machrowska, A., & Jonak, J. (2018). xEMD procedures as a data—Assisted filtering method. *AIP Conference Proceedings*, 1922, 120007. https://doi.org/10.1063/1.5019122

Machrowska, A., Karpiński, R., Jonak, J., Szabelski, J., & Krakowski, P. (2020). Numerical prediction of the component-ratio-dependent compressive strength of bone cement. *Applied Computer Science*, *16*(3), 88–101. https://doi.org/10.23743/acs-2020-24

Machrowska, A., Szabelski, J., Karpiński, R., Krakowski, P., Jonak, J., & Jonak, K. (2020). Use of Deep Learning Networks and Statistical Modeling to Predict Changes in Mechanical Parameters of Contaminated Bone Cements. *Materials*, *13*(23), 5419. https://doi.org/10.3390/ma13235419

Madej, H., Czech, P., & Konieczny, Ł. (2003). Wykorzystanie dyskryminant bezwymiarowych w diagnostyce przekładni zębatych. *Diagnostyka*, *28*, 17–22.

Mathiessen, A., Cimmino, M. A., Hammer, H. B., Haugen, I. K., Iagnocco, A., & Conaghan, P. G. (2016). Imaging of osteoarthritis (OA): What is new? *Best Practice & Research Clinical Rheumatology*, *30*(4), 653–669. https://doi.org/10.1016/j.berh.2016.09.007

Matthews, B. W. (1975). Comparison of the predicted and observed secondary structure of T4 phage lysozyme. *Biochimica et Biophysica Acta (BBA) – Protein Structure*, *405*(2), 442–451. https://doi.org/10.1016/0005-2795(75)90109-9

McDonough, C. M., & Jette, A. M. (2010). The Contribution of Osteoarthritis to Functional Limitations and Disability. *Clinics in Geriatric Medicine*, *26*(3), 387–399. https://doi.org/10.1016/j.cger.2010.04.001

Möller, I., Bong, D., Naredo, E., Filippucci, E., Carrasco, I., Moragues, C., & Iagnocco, A. (2008). Ultrasound in the study and monitoring of osteoarthritis. *Osteoarthritis and Cartilage*, *16*, S4–S7. https://doi.org/10.1016/j.joca.2008.06.005

Powers, D. M. W. (2020). Evaluation: From precision, recall and F-measure to ROC, informedness, markedness and correlation. *ArXiv:2010.16061 [Cs, Stat]*. http://arxiv.org/abs/2010.16061

Prior, J., Mascaro, B., Shark, L.-K., Stockdale, J., Selfe, J., Bury, R., Cole, P., & Goodacre, J. A. (2010). Analysis of high frequency acoustic emission signals as a new approach for assessing knee osteoarthritis. *Annals of the Rheumatic Diseases*, *69*(5), 929–930. https://doi.org/10.1136/ard.2009.112599

Rabiej, M. (2018). *Analizy statystyczne z programami Statistica i Excel*. Wydawnictwo Helion.

Rangayyan, R. M., & Wu, Y. F. (2008). Screening of knee-joint vibroarthrographic signals using statistical parameters and radial basis functions. *Medical & Biological Engineering & Computing*, *46*(3), 223–232. https://doi.org/10.1007/s11517-007-0278-7

Reyes, C., Garcia-Gil, M., Elorza, J. M., Mendez-Boo, L., Hermosilla, E., Javaid, M. K., Cooper, C., Diez-Perez, A., Arden, N. K., Bolibar, B., Ramos, R., & Prieto-Alhambra, D. (2015). Socio-economic status and the risk of developing hand, hip or knee osteoarthritis: A region-wide ecological study. *Osteoarthritis and Cartilage*, *23*(8), 1323–1329. https://doi.org/10.1016/j.joca.2015.03.020

Richette, P., & Latourte, A. (2019). Osteoarthritis: Value of imaging and biomarkers. *La Revue Du Praticien*, *69*(5), 507–509.

Rogala, M. (2020). Neural Networks in Crashworthiness Analysis of Thin-Walled Profile with Foam Filling. *Advances in Science and Technology Research Journal*, *14*(3), 93–99. https://doi.org/10.12913/22998624/120989

Stanik, Z. (2013). *Diagnozowanie lozysk tocznych pojazdów samochodowych metodami wibroakustycznymi*. Wydawnictwo Naukowe Instytutu Technologii Eksploatacji – Państwowego Instytutu Badawczego.

Szabelski, J. (2018). Effect of incorrect mix ratio on strength of two component adhesive Butt-Joints tested at elevated temperature. *MATEC Web of Conferences*, *244*, 01019. https://doi.org/10.1051/matecconf/201824401019

Szabelski, J., Karpiński, R., & Machrowska, A. (2022). Application of an Artificial Neural Network in the Modelling of Heat Curing Effects on the Strength of Adhesive Joints at Elevated Temperature with Imprecise Adhesive Mix Ratios. *Materials*, *15*(3), 721. https://doi.org/10.3390/ma15030721

Tadeusiewicz, R. (1993). *Sieci neuronowe* (Vol. 110). Akademicka Oficyna Wydawnicza.

Van den Borne, M. P. J., Raijmakers, N. J. H., Vanlauwe, J., Victor, J., de Jong, S. N., Bellemans, J., & Saris, D. B. F. (2007). International Cartilage Repair Society (ICRS) and Oswestry macroscopic cartilage evaluation scores validated for use in Autologous Chondrocyte Implantation (ACI) and microfracture. *Osteoarthritis and Cartilage*, *15*(12), 1397–1402. https://doi.org/10.1016/j.joca.2007.05.005

Walters, C. F. (1929). The value of joint auscultation. *The Lancet*, *213*(5514), 920–921.

Wu, Y. (2015). *Knee joint vibroarthrographic signal processing and analysis*. Springer.

Applied Computer Science, vol. 18, no. 2, pp. 86–100
doi: 10.35784/acs-2022-15

Submitted: 2022-04-24 | Revised: 2022-06-08 | Accepted: 2022-06-08

Keywords: RowHammer, Cyber Security, DRAM

Hakan AYDIN [0000-0002-0122-8512]*, *Ahmet SERTBAŞ* [0000-0001-8166-1211]**

CYBER SECURITY IN INDUSTRIAL CONTROL SYSTEMS (ICS): A SURVEY OF ROWHAMMER VULNERABILITY

Abstract

Increasing dependence on Information and Communication Technologies (ICT) and especially on the Internet in Industrial Control Systems (ICS) has made these systems the primary target of cyber-attacks. As ICS are extensively used in Critical Infrastructures (CI), this makes CI more vulnerable to cyber-attacks and their protection becomes an important issue. On the other hand, cyberattacks can exploit not only software but also physics; that is, they can target the fundamental physical aspects of computation. The newly discovered RowHammer (RH) fault injection attack is a serious vulnerability targeting hardware on reliability and security of DRAM (Dynamic Random Access Memory). Studies on this vulnerability issue raise serious security concerns. The purpose of this study was to overview the RH phenomenon in DRAMs and its possible security risks on ICSs and to discuss a few possible realistic RH attack scenarios for ICSs. The results of the study revealed that RH is a serious security threat to any computer-based system having DRAMs, and this also applies to ICS.

1. INTRODUCTION

The industry 4.0 concept represents the new industrial revolution, which aims to bring together Information Technologies (IT) and Industry. This concept has enabled the inclusion of Cyber-Physical Systems (CPSs) in production systems. CPS is defined as integrations of computation, communication, and control to achieve the desired performance from physical processes (Mahmoud & Hamdan, 2019). Examples of CPSs include smart grids, autonomous car systems, medical monitoring, Industrial Control Systems (ICSs), robotic systems, and autopilot avionics projects (Khaitan & McCalley, 2014). CPS is often associated with the Industry 4.0 perspective (Carvajal, Rojas & Chacón, 2018; Johari et al., 2022; Lieu et al., 2019) and it is one of the underlying forces of Industry 4.0. Today, CPS, and thus Industry 4.0, seems to be promising in terms of producing new solutions, improving resource usage, and increasing efficiency. The most common example of CPSs is ICS, which is widely used in almost every Critical Infrastructure (CI) (Lu et al., 2014). Cyber security incidents that may occur in ICSs involve risks of causing large scale economic damage, loss of life,

* Istanbul Topkapı University, Faculty of Engineering, Istanbul, Turkey, hakanaydin@topkapi.edu.tr
** Istanbul University-Cerrahpasa, Faculty of Engineering, Istanbul, Turkey, asertbas@iuc.edu.tr

and even damage to national security. The integration of CI into public networks exposes the underlying ICS to a various attack vector (Zimba, Wang & Chen, 2018). According to Kaspersky ICS CERT (Industrial control systems threat medley: spyware and malicious scripts on the rise in H1 2021, 2021), almost one in three industrial computers is subject to malicious activity as shown in Figure 1.

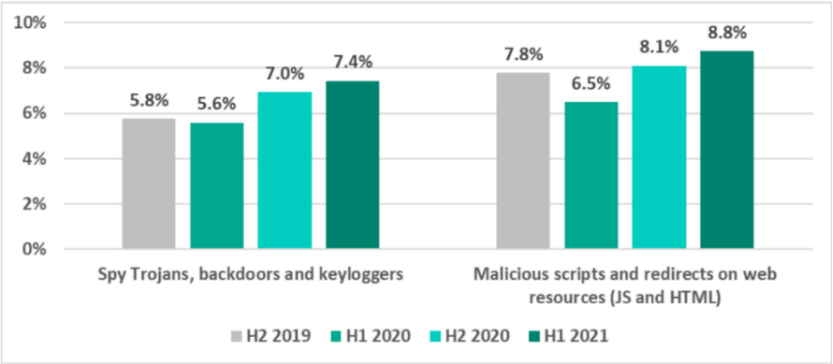

Fig. 1. Percentage of ICS computers on which malicious objects were blocked

However, cyber-attacks target not only software but also hardware. That is, such attacks also target the fundamental physical aspects of computing. Rowhammer (RH) is a fault injection attack targeting hardware on reliability and security of Dynamic Random Access Memory (DRAM). This security exploit targets DRAM, in which memory cells interact among themselves, by changing the contents of adjacent memory rows that are not addressed in the original memory access. RH was first introduced at the ISCA 2014 conference (Kim et al., 2014). RH bug occurs in most of today's memory modules and has destructive consequences for the security of all affected systems (e.g., privilege escalation attacks) (Gruss, Maurice & Mangard, 2016). It is stated that 85% of the DDR3 memories are vulnerable to RH (Kim et al., 2014). Today's DRAMs, including DDR4, are also vulnerable to RH (Cojocar et al., 2014; Gruss et al., 2018).

The purpose of this study is to provide an overview of RH, highlight the security risks that this vulnerability can pose to ICSs, and present a few realistic RH attack scenarios for ICSs. The scenarios described in this study are presented for the first time. For the purpose of the study, two basic questions are tried to be answered:

1. How can the RH cyber threat be evaluated within the scope of cyber security of ICSs?
2. What is the possible RH cyberattacking scenarios? The descriptive method was used in the research.

The contributions of this study to the literature can be expressed as follows:

– A comprehensive cybersecurity analysis of the RH problem is investigated within the scope of ICS cybersecurity.
– For the first time, several realistic RH attack scenarios and countermeasures for cybersecurity of ICSs are presented.

In the remaining of this article, a literature review on the related studies is presented in the 2nd section, while CPS & ICS and RH are overviewed in the 3rd section. RH attack scenarios are presented in the 4th section. Finally, in the 5th section, the study is concluded, and some ideas for future studies are explained.

2. LITERATURE REVIEW

The RH problem was first raised by Kim et al. (2014). By conducting experimental studies on Intel (Sandy Bridge, Ivy Bridge, and Haswell) and AMD (Piledriver) systems using 2GB DDR3 modules, they showed that activating the same row in DRAM repeatedly corrupted the data in rows near this row. In addition, they proved in their study that up to 139K accesses were required to cause RH vulnerability and that up to one in every 1.7K cell was prone to errors. The authors proposed a low-cost solution to the RH problem they identified in their study. In the study conducted by Razavi et al. (2016), Flip Feng Shui (FFS) was presented as a new exploit vector that allowed an attacker to initiate random bit flips on physical memory in a completely controlled manner. By implementing an instance using the RH bug and memory deduplication, the authors showed that FFS was possible with very few constraints on the target data. They showed that FFS is extremely powerful; that is, a malicious VM in a practical cloud setting can gain unauthorized access to a co-hosted victim VM running OpenSSH. Using FFS, they exemplified end-to-end attacks breaking OpenSSH public-key authentication and forging GPG signatures from trusted keys, thereby compromising the Ubuntu/Debian update mechanism. Bosman et al. (2016) showed that a JavaScript-enabled attacker could use it to generate the RH exploit. The authors demonstrated in their study that random memory read/write access is possible with a modern Microsoft Edge browser. Gruss et al. (2016) showed that a fully automated attack through a website containing Javascript triggers failures on remote hardware. They showed that caches could be forced into fast cache eviction to trigger the RH bug with only regular memory accesses. Tatar et al. (2016) revealed that an attacker could trigger and exploit RH bitflips directly from a remote machine by only sending network packets. This is made possible by RDMA-enabled networks, which are widely used in clouds and data centers and are becoming increasingly fast. To demonstrate the threat, they showed how a malicious client could exploit RH bit flips to gain code execution on a remote key value server application. To counter this threat, they proposed protecting unmodified applications with a new buffer allocator that could achieve fine-grained memory isolation in the DRAM address space. Aweke et al. (2016) presented a software-based defense, ANVIL, which can block all known RH attacks on existing systems. ANVIL detects RH attacks by tracking the locality of DRAM accesses using existing hardware performance counters. The detector identifies the rows that are frequently accessed (i.e., the aggressors) and then selectively refreshes the nearby victim rows to prevent hammering. Experiments conducted on real hardware with the SPEC2006 benchmarks have shown that ANVIL has less than a 1% false-positive rate and an average slowdown of 1%. Aweke et al. (2016) also claimed that ANVIL is an effective approach for protecting existing and future systems from even advanced RH attacks. In a study conducted by Aga et al. (2017), a virtual-memory-based cache-flush free attack was enabled by the Cache Allocation Technology, a mechanism designed in part to protect virtual machines from denial-of-service (DOS) attacks. In the study of Bhattacharya & Mukhopadhyay (2018), a methodology combining timing analysis to perform hammering in a controlled manner for the purpose of creating bitflips in cryptographic keys stored in memory was presented. Barenghi et al. (2018) proposed a methodology to reverse engineer such maps without direct physical probing of the DRAM bus of the target platform. In a study con-ducted by Gruss et al. (2018), a new technique, named opcode flipping, that bypassed recent isolation mechanisms by flipping bits in a predictable and targeted way

in user space binaries was proposed. The scholars replaced conspicuous and memory-exhausting spraying and grooming techniques with a novel reliable technique called memory waylaying. They abused Intel SGX to hide the attack entirely from the user and the operating system, making any inspection or detection of the attack infeasible. Cojocar et al. (2020) presented an end-to-end methodology to determine if cloud servers were susceptible to RH. They applied their methodology to three classes of servers from a major cloud provider. Their findings showed that none of the CPU instruction sequences used in previous studies to initiate RH attacks create worst-case DRAM testing conditions. To address this limitation, they developed an instruction sequence that leveraged microarchitectural side effects to hammer DRAM at a near-optimal rate on modern Intel Skylake and Cascade Lake platforms. They also designed a DDR4 fault injector that can reverse engineer row adjacency for any DDR4 DIMM. When applied to their cloud provider's DIMMs, they found that DRAM rows did not always follow a linear map. Hassan et al. (2021) proposed U-TRR, a novel experimental methodology for reverse-engineering Target RowRefresh (TRR), to implement in modern DRAM chips. Farmani et al. (2021) proposed an efficient test framework, called RHAT, to address the detection of RH vulnerable cells, which was very difficult, time-consuming, and expensive. It was stated that RHAT could be used for both manufacturing tests and in-field (deployment) tests. Kim et.al (2020) conducted experimental studies on 1580 DRAM chips (408× DDR3, 652× DDR4, and 520× LPDDR4) out of 300 DRAM modules (60× DDR3, 110× DDR4, and 130× LPDDR4) to reveal how RH affected modern and future devices at the circuit level. Zhang et al. (2022) systematized RH attacks and defenses by focusing on DRAM. Chekole et al. (2017) investigated the applicability of strong counter-measures against memory-safety attacks in the context of realistic ICS. They designed an experimental setup based on Programmable Logic Controller (PLC). Their results showed the security measure was highly effective in detecting memory-safety violations. Peng et al. (2015) presented an ICS-CPS operation dual-loop analysis model (ICONDAM) to be able to analyse human-cyber-physical interdependences of ICSs. According to the ICONDAM, a unified and fusion view for ICS is presented in Figure 2.

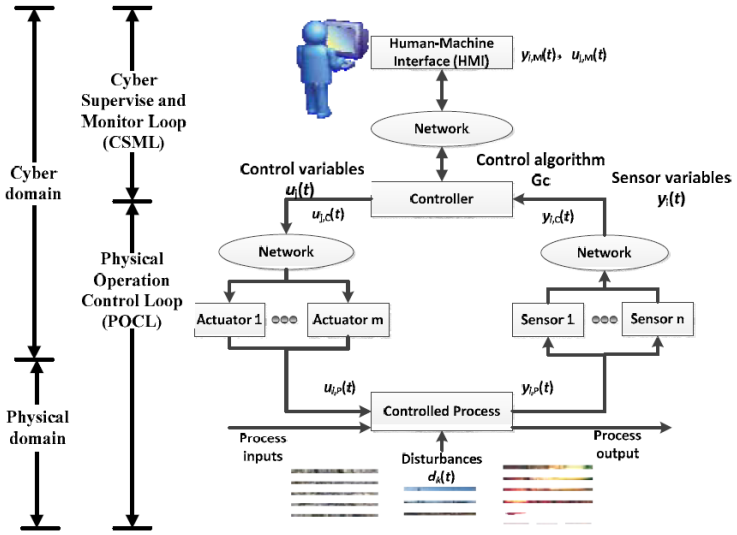

Fig. 2. ICS-CPS operation dual-loop analysis model (Peng et al., 2015)

A summary of the studies reviewed above is presented in Table 1.

Tab. 1. A summary of the studies reviewed

Research	Year	Summary
Kim et al.	2014	RH was first introduced as a failure mechanism in DRAM at the ISCA 2014 conference.
Gruss et al.	2016	It is demonstrated that a remote takeover of a server was vulnerable to RH via JavaScript code execution.
Razavi et al.	2016	It was shown that the victim virtual machine (VM) was hijacked by another attacker VM running on the same system.
Van Der Veen et al.	2016	This study shows that existing mobile systems are widely vulnerable to RH attacks.
Aga et al.	2017	A virtual memory-based non-cache attack, which was fast enough for RH with a double-speed refresh, was presented.
Jang et al.	2017	The Intel Software Guard Extensions (SGX)-Bomb attack that launches the RH attack against enclave memory to trigger the processor lockdown was introduced.
Frigo et al.	2018	Hijacking a mobile system by triggering RH using the WebGL interface on a mobile GPU was studied.
Lipp et al.	2018	The takeover over a remote system by triggering RH through the Remote Direct Memory Access (RDMA) protocol was presented.
Cojocar et al.	2020	In the study, an end-to-end methodology was proposed to determine if cloud servers were susceptible to RH.
Kim et al.	2020	Experimental studies on 1580 DRAM chips (408× DDR3, 652× DDR4, and 520× LPDDR4) out of 300 DRAM modules (60× DDR3, 110× DDR4, and 130× LPDDR4) were conducted. It was definitively shown that new DRAM chips were more vulnerable to RH.
Hassan et al.	2021	U-TRR, which is a novel experimental methodology for the reverse-engineering main RH mitigation mechanism was proposed.
Yağlikçi et al.	2021	BlockHammer, a low-cost, effective, and easy-to-adopt RH mitigation mechanism that prevents all RH bit-flips while overcoming the two key challenges was proposed. The proposed throttling technique selectively throttles memory accesses that could potentially cause RH bit flips.
Farmani et al.	2021	An efficient test framework, called RHAT, which can be employed for both manufacturing tests and in-field (deployment) tests was proposed.
Lee & Kwak	2021	A new attack detection technique, which extracts common features of RH attack files by performing static analysis of the attack codes, was proposed.
Zhang et al.	2022	The authors systematized RH attacks and defenses by focusing on DRAM.

The literature review presented in this study shows that RH is identified as a security threat to any computer-based system with DRAM.

3. BACKGROUND

3.1. An Overview of Industrial Control Systems (ICSs)

CPS refer to a modern system that integrates real-time data and modern Information and Communications Technologies (ICT) into the physical world (Carvajal, Rojas, & Chacón, 2018). In general, a CPS consists of the following elements: Plants, Sensors, PLCs, Actuators, Communication networks, and SCADA (Chekole et al., 2017). CIs, such as the power grid or water distribution network, are CPSs (Friedberg et al., 2017). CPS, which is an integration of computation, networking, and physical processes, plays an increasingly important role in critical infrastructure, government, and everyday life (Ding et al., 2018). ICT is increasingly becoming embedded and pervasive, which leads to CPSs (Chekole et al., 2017). CPS is the basis for the development of the areas such as smart manufacturing, smart medicine, smart buildings and infrastructures, smart city, smart vehicles, wearable devices, mobile systems, defense systems, meteorology, etc. (Figure 3).

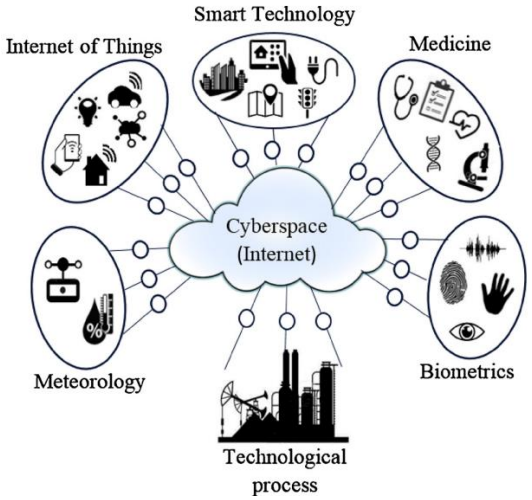

Fig. 3. Cyber-physical systems (Alguliyev, Imamverdiyev & Sukhostat, 2018)

CPS includes ICS (Khaitan & McCalley, 2014). According to Peng et al. (2015), ICSs are CPSs, and they affect the physical world directly. ICSs are used in industry to monitor and control processes related to industrial areas such as water, oil, gas, chemistry, paper, food, beverage, pharmaceutical, petroleum, natural gas pipelines, electrical networks, transportation, and railways. ICSs serve as the basic infrastructure to control or operate any type of industrial system, including those used in CI. ICS is the central nervous system of national critical infrastructures such as power plants, power grids, oil refineries, oil and gas pipelines, chemical plants, urban transport, railways, shipbuilding, and defense (Lu et al., 2014). Moreover, ICS is an all-encompassing term used for various automation systems and their de-vices, such as PLC, Human Machine Interface (HMI), Supervisory Control and Data Acquisition (SCADA) systems, Distributed Control Systems (DCS), Safety Instrumented Systems (SIS), and many others (Figure 4).

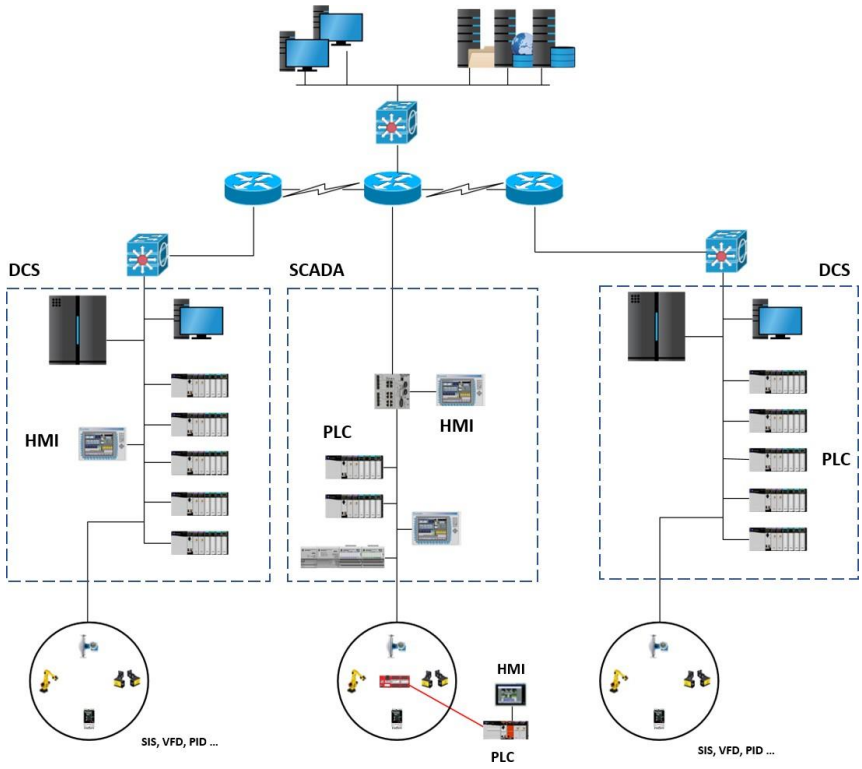

Fig. 4. Industrial Control System (ICS) Components (Ackerman, 2017)

The largest subgroup of ICS is SCADA systems (Stouffer, Falco & Scarfone, 2011). SCADA systems are a type of ICS that provides surveillance and control of a system and is designed to control, manage and monitor systems remotely and automatically. Control systems include SCADA systems that are used to monitor and control various decentralized operations; this actually means that the person who runs it is not physically right next to you (Teixeira et al., 2018). ICS and CI operated via SCADA systems can be shown as examples of operating CPSs through IT infrastructures that ensure timely data transmission between system components (Mahmoud & Hamdan, 2019).

PLC can be defined as automation devices that are generally used in production departments in factories or in the control of processes such as the control of machines. In general, a PLC consists of a Central Processing Unit (CPU), a Memory Unit, an Input Unit, and an Output Unit. A PLC Memory Unit (RAM, ROM, PROM, etc.) is the unit where the specific program used by the PLC is stored. PLC can use RAM, ROM PROM, EPROM, or EEPROM type memories. PLC memories, which are important and inseparable parts of PLC, are Internal and External Memories. The internal memory in the PLC is a type of burner in the user-accessible RAM structure. External memory, on the other hand, is the memory out-side the PLC and is usually of the EPROM or EEPROM type. However, the memory element used more often in PLCs is EPROM. As the name suggests, EPROM stands for erasable programmable read-only memory. On the other hand, DCSs are used to control production systems for industries such as oil refineries, water, and wastewater treatment, electrical power generation plants, and pharmaceutical processing plants.

Today, the increasing dependency of ICS on ICT and especially on the Internet has exposed these systems to cyber-attacks and threats. The interconnection of SCADA systems to various networks has exposed them to network security problems (Igure, Laughter & Williams, 2006). Since ICS is responsible for monitoring and controlling many CIs, a security vulnerability in these systems can cause not only economic damage but also the inability of people to receive critical services that are necessary for their lives and perhaps even loss of life. Cyber-attacks that may occur in ICS systems can cause some problems such as fire and explosion by stopping industrial production facilities in cyberspace, causing system crashes, and making wrong manoeuvres on the systems. As a vital part of CI infrastructure, protecting ICS from cyber threats has become a high priority (Barrère et al., 2020).

Cyber terrorism uses computer systems to shut down or damage critical national infrastructures such as energy, transportation, and state operations and to coerce or intimidate a government or civilian population. Currently, the most famous cyber-attack targeting ICSs is Stuxnet (Yampolskiy et al., 2013). Considering the sectoral distribution of cyber-attacks, it is seen that attacks against the energy sector are in the first place, and these CI hosting ICS/SCADA systems are among the sectors most exposed to cyber-attacks (Ackerman, 2017). ICS typically involve a large spectrum of overlapping cyber-physical security measures used to protect their operational components (Barrère et al., 2020). SCADA and other ICSs continue to present several challenges that make protection of them particularly difficult against determined attackers (Loukas, 2015). Cyberattacks exploiting memory-safety vulnerabilities constitute a major attack vector against CPSs (Chekole et al., 2017). The National Institute of Standards and Technology (NIST) states that possible events an ICS may encounter will include Blocked or delayed flow of information through ICS networks (Bhattacharya & Mukhopadhyay, 2018).

3.2. Rowhammer (RH) Vulnerability

Memory is the key component in computer systems and it is important for short-term data access within a computer. It is the central storage unit of the computer system made up of RAM and ROM, which communicate directly within the CPU, Auxiliary memory, and Cache memory. Computer systems use different memories, and the amount of memory that a computer system uses affects and determines the speed and performance of that system. That is, speed and cost are the two most important parameters of the memory of a computer system. The fastest memory circuits need adding a considerable number of circuits to the main memory, which makes the memory expensive. DRAM and SRAM are fast-speed and volatile memories, while ROM, PROM, EPROM, and EEPROM are non-volatile memories. DRAM capacity has been increased by downsizing it in size, and this scaling has brought more capacity, reasonable energy savings, and lower cost, but has not helped with latency that much. A modern DRAM cell consists of an access transistor and a capacitor (Figure 5).

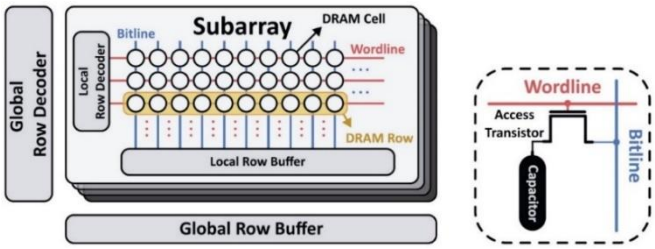

Fig. 5. DRAM bank and cell (Kim et al., 2020)

DRAM failure mode is now popularly called RH (Mutlu & Kim, 2019). A DRAM cell stores a single bit of data based on the charge level of the cell capacitor. But over time, charge leaks appear from the storage capacitor. Repeatedly opening (activating) and closing (pre-charging) a DRAM row causes RH bitflips in nearby cells. To access data on a DRAM row, the memory controller must first activate the DRAM row it wants to reach. Then, to be able to begin accessing data from another DRAM row, the memory controller must close or pre-charge the previous DRAM row. Rapidly activating and pre-charging a DRAM bank may cause bit flips on nearby rows. This phenomenon is known as RH. Shortly, RH is a problem related to some recent DRAM devices in which repeatedly accessing (i.e., hammering) a row of memory can cause bit flips in adjacent rows (Kim et al., 2014; Seaborn & Dullien, 2015; Orosa et al., 2021). It has been demonstrated in the literature that parasitic effects in DRAM can alter the contents of a memory cell without accessing it, but by accessing other memory lo-cations at a high frequency (Gruss et al., 2016). RH has emerged as a vulnerability where repeated ac-cess to a DRAM row could speed up the unloading of neighbouring bits (Aga, Aweke & Austin, 2017). The RH problem enables powerful privilege-escalation attacks by allowing unauthorized changing of bits in DRAM cells (Gruss et al., 2018). This is a classic example of how layered abstractions and trust (in this case, virtual memory) can be broken from a hardware level (Qiao & Seaborn, 2016). In the RH problem, the same address in DRAM is read over and over again and the data at the addresses close to this address is corrupted. Circuit-level charge leakage mechanisms that are exacerbated by certain memory access patterns cause RH bitflips (Cojocar et al., 2020). RH is a prime (and perhaps the first) example of how a circuit-level failure mechanism can cause a practical and widespread system security vulnerability (Mutlu & Kim, 2019).

The potential vulnerabilities of all DRAM types to RH attacks are published by studies related to the security issue. These attacks are a problem that has arisen as a result of DRAM scaling and threaten hardware reliability and security. By a RH attack, it is possible to change the data on the attacked hardware, such as altering existing data or elevating the attacker's privileges. These attacks have become a problem as a result of the gradually shrinking of modern memory cards known as RAM. A study showed that given the number of cores increasing faster than DRAM capacity, the expected memory capacity per core would decrease by 30% every two years (Mutlu & Subramanian, 2015). When scaling the size of the computing system, memory also must be scaled, but this makes the maintenance and enhancement of its capacity, energy efficiency, and reliability significantly costlier than conventional techniques (Mutlu, 2015). RH attacks are about the idea that hardware is not so vulnerable and one can attack hardware by exploiting its vulnerabilities. Hardware-related attacks, such as RH, prompted some researchers to examine hardware issues and focus on

other hardware-related issues. An RH attack can control user access and compromise the integrity of sensitive data with attacks such as a privilege escalation and an alteration of the encryption keys (Lee & Kwak, 2021). Kim at al. (2014) showed that a very simple user-level program can also reliably and consistently induce RH errors in AMD and Intel systems that use vulnerable DRAM modules.

3.3. Countermeasures for Rowhammer Vulnerability

As a defense against cyberattacks caused by exploiting the RH vulnerability, manufacturers attempt to improve the hardware's DRAM chips or fix errors using an error-correcting code (ECC). Studies are carried out on efforts for increasing the refresh rate, which is among these defenses. Since DRAMs affected by RH are currently used in the market, it is evaluated that RH attacks should be detected before they occur, and studies are carried out on defense measures against this vulnerability. In their study, Kim et al. (2014) examined seven solutions (Table 2) to tolerate, prevent, or reduce corruption errors. They stated that among these solutions, the seventh and final solution, called PARA, was the most efficient and cost-effective.

Tab. 2. Seven Solutions to Rowhammer (RH) Problem (Kim et al., 2014)

No.	Solution	Summary
1.	Make better chips	The problem can be fixed by manufacturers at the chip level.
2.	Correct errors	It is about employing ECC modules that have extra DRAM chips in server-grade systems. Due to their high cost, ECC modules are rarely used in consumer-grade systems.
3.	Refresh all rows frequently	For sufficiently short refresh intervals, corruption errors can be eliminated.
4.	Retire cells (manufacturer)	Victim cells can be identified and remapped to spare cells by manufacturers before DRAM chips are sold.
5.	Retire cells (end-user)	Modules can be tested by end-users, and system-level methods can be applied by them to struggle with problems
6.	Identify “hot” rows and refresh neighbors.	Refreshing neighbors of frequently opened rows only.
7.	PARA (Probabilistic Adjacent Row Activation) Solution	Refreshing of a given adjacent row with a probability when the row is closed.

Deployed defenses employ two strategies (Aweke et al., 2016): (1) doubling the system DRAM refresh rate and (2) restricting access to the CLFLUSH instruction that attackers use to bypass the cache to in-crease memory access frequency. To address the RH problem, computer and software vendors have: i) doubled DRAM refresh rates, ii) restricted access to virtual-to-physical page mappings, and iii) disabled access to cache-flush operations in sandboxed environments (Aga, Aweke & Austin, 2017). RH is a critical vulnerability and it is important to address and provide solutions to the issues identified in the potential RH scenarios suggested above. Enforcing Error Correction Codes (ECC) protection, increasing the refresh rate of DRAM cells, abolishing the use of DRAM cells that the DRAM manufacturers identify as victim cells, and refreshing vulnerable rows can be shown among the solutions to the RH problem (Kim et al., 2014). Regarding this problem, in their critical

security release, Apple has publicly mentioned that they increased the memory refresh rates (Mutlu & Kim, 2019). ANVIL, which ended up as another solution proposal, proposes software-based detection of RH attacks. In this method hardware, performance counters, and selective explicit refreshing of victim rows that are determined to be under attack are monitored (Aweke et al., 2016).

4. CYBER ATTACK SCENARIOS

Considering the RH vulnerability issue as a security threat to ICSs, this section describes the RH exploit attempts against ICSs in five different scenarios as shown in Figure 6.

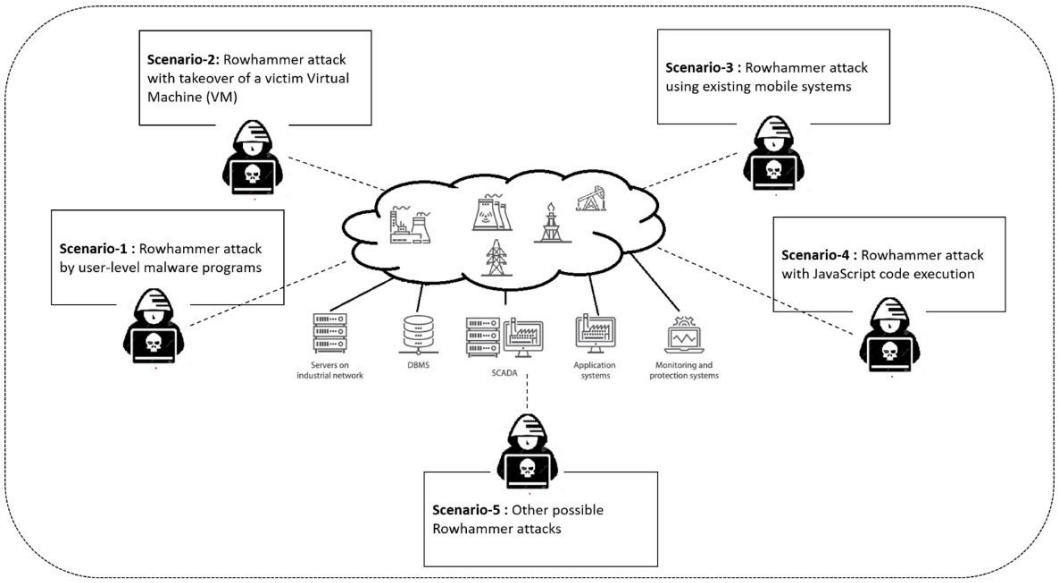

Fig. 6. Row Hammer Attack Scenarios for ICS Security

The first scenario is based on attacking ICS hardware by user-level malware programs. Using malware in cyber-attacks is one of the most typical incidents in practice. RH can be exploited by a user-level malicious program to breach memory protection and compromise the ICS system. The cyber-attacks in this scenario can be carried out by triggering the RH threat with spy trojans, backdoors and keyloggers, malicious scripts, and redirects on web resources (JS and HTML). In the scenario, it is assumed that with some engineering effort, a program is developed that triggers the RH problem, crashing the system or taking control of the system. This scenario is one of the most likely in ICSs since malware programs are designed specifically to target ICSs. The malicious codes can be injected into programs or used to intercept the system control by utilizing a bit flip attack.

The second scenario, a victim virtual machine (VM) is hijacked by another attacker VM running on the same system. Virtualization is one of the most important technology catalysts for the new industrial revolution. Virtualized solutions require fewer physical servers because multiple virtual control functions can be combined on industry-standard hardware along with information technology (IT) and operational technology (OT) functions, rather

than deploying each function as a dedicated device. Virtualization enables CI companies to reduce operating costs with secure, robust, flexible software-based solutions as an alternative to legacy, fixed-function hardware. In the case of such an attack, since RH attacks modify memory without writes, the modification cannot be detected, and the victim VM continues to use the corrupted page.

The third scenario is based on the idea that existing mobile systems used in ICSs are widely vulnerable to RH attacks. In this scenario, there is an attack that exploits RH on a mobile device using a malicious user-level application that requires no permissions. This third scenario of our study takes advantage of the deterministic memory allocation patterns in the Android Linux Operating System. In this RH attack scenario, which is not based on software vulnerability and does not require user permission, an Android-based root exploit is used.

The fourth scenario is based on the idea that an RH attack can be launched by a website to gain root privileges on an ICS that uses or visits the website. In this scenario, the RH attack is initiated by a website to gain root privileges on an ICS system that uses or visits the website via JavaScript. In the scenario, a server vulnerable to RH is taken over remotely via JavaScript code execution. Since JavaScript is available and enabled by default in every modern browser, this fourth attack can be launched by a web-site to gain root privileges on a system that visits the website. Since this type of attack, which can be done through a website, can be carried out simultaneously and secretly on ICSs, it creates a huge security threat. In this scenario, the fully automated attack runs in JavaScript through a remote website and can gain unrestricted access to systems. As a result of this attack, unlimited access to the systems of website visitors can be achieved.

The fifth scenario is based on the idea that different types of RH attacks can be carried out by cyber attackers, especially on ICS components. Many studies in the literature show other practical hacks using this fault injection attack. In this context, it can be said that new types of RH attacks targeting ICSs can be carried out by cyber attackers, except for the attack scenarios specifically mentioned above.

5. CONCLUSION

In this study, after an overview of the phenomenon of RowHammer (RH) in DRAMs, RH induced security risks to ICSs, and scenarios for possible RH attacks targeting ICSs were discussed. In this context, the RH security exploits that take advantage of an unintended and undesirable side effect in DRAM were presented as a security threat to ICSs. The overview of the RH problem in DRAMs, ways to induce it, countermeasure techniques against it, and the possible attack scenarios discussed in the paper were adopted from the studies published in the literature. It is seen in this study that the RH problem is identified as a security threat to any computer-based system with DRAMs. This is also important in terms of computer architecture because modern computer architecture also aims to design secure computer hardware that can prevent and be immune to cyber-attacks. It is an inevitable fact that even a simple hardware failure mechanism at the circuit level will endanger the security of the entire system. Even though ICSs generally use industry-standard computers, today they have begun to resemble classical computer systems in terms of operating systems, network protocols, remote access capabilities, wireless networking, etc. Different units of ICSs,

such as SCADA, HMI, and PLC, contain DRAM. In this respect, RH vulnerability also arises as a security threat to ICSs, as in any other cyber-physical system with DRAMs. This study can inspire many researchers to take RH into account in studies to be conducted to identify new attacks that may be carried out against CPSs.

For future studies, we plan to perform some of the RH attack scenarios described in this study in a real ICS simulation test environment and evaluate their results.

REFERENCES

Ackerman, P. (2017). *Industrial Cybersecurity: Efficiently secure critical infrastructure systems*. Packt Publishing Ltd.

Aga, M. T., Aweke, Z. B., & Austin, T. (2017). When good protections go bad: Exploiting anti-DoS measures to accelerate Rowhammer attacks. In *2017 IEEE International Symposium on Hardware Oriented Security and Trust (HOST)* (pp. 8–13). IEEE. https://doi.org/10.1109/HST.2017.7951730

Alguliyev, R., Imamverdiyev, Y., & Sukhostat, L. (2018). Cyber-physical systems and their security is-sues. *Computers in Industry*, *100*, 212-223. https://doi.org/10.1016/j.compind.2018.04.017

Aweke, Z. B., Yitbarek, S. F., Qiao, R., Das, R., Hicks, M., Oren, Y., & Austin, T. (2016). ANVIL: Soft-ware-based protection against next-generation Rowhammer attacks. *ACM SIGPLAN Notices*, *51*(4), 743–755. https://doi.org/10.1145/2954679.2872390

Barenghi, A., Breveglieri, L., Izzo, N., & Pelosi, G. (2018). Software-only reverse engineering of physical DRAM mappings for RowHammer attacks. In *2018 IEEE 3rd International Verification and Security Workshop (IVSW)* (pp. 19–24). IEEE. https://doi.org/10.1109/IVSW.2018.8494868

Barrère, M., Hankin, C., Nicolaou, N., Eliades, D. G., & Parisini, T. (2020). Measuring cyber-physical security in industrial control systems via minimum-effort attack strategies. *Journal of information security and applications*, *52*, 102471. https://doi.org/10.1016/j.jisa.2020.102471

Bhattacharya, S., & Mukhopadhyay, D. (2018). Advanced fault attacks in software: Exploiting the RowHammer bug. In *Fault Tolerant Architectures for Cryptography and Hardware Security* (pp. 111–135). Springer. https://doi.org/10.1007/978-981-10-1387-4_6

Bosman, E., Razavi, K., Bos, H., & Giuffrida, C. (2016). Dedup est machina: Memory deduplication as an advanced exploitation vector. In *2016 IEEE symposium on security and privacy* (SP) (pp. 987–1004). IEEE. https://doi.org/10.1109/SP.2016.63

Carvajal, J. H., Rojas, O. A., & Chacón, E. (2018). Cyber-physical system for industrial control automation based on the holonic approach and the IEC 61499 standard. In *2018 Forum on Specification & Design Languages (FDL)* (pp. 5–16). IEEE. https://doi.org/10.1109/FDL.2018.8524082

Chekole, E. G., Castellanos, J. H., Ochoa, M., & Yau, D. K. (2017). Enforcing memory safety in cyber-physical systems. *In Computer security* (pp. 127–144). Springer. https://doi.org/10.1007/978-3-319-72817-9_18

Cojocar, L., Kim, J., Patel, M., Tsai, L., Saroiu, S., Wolman, A., & Mutlu, O. (2020). Are we susceptible to Rowhammer? An end-to-end methodology for cloud providers. In *2020 IEEE Symposium on Security and Privacy (SP)* (pp. 712–728). IEEE. https://doi.org/10.1109/SP40000.2020.00085

Ding, D., Han, Q. L., Xiang, Y., Ge, X., & Zhang, X. M. (2018). A survey on security control and attack detection for industrial cyber-physical systems. *Neurocomputing*, *275*, 1674–1683. https://doi.org/10.1016/j.neucom.2017.10.009

Farmani, M., Tehranipoor, M., & Rahman, F. (2021). RHAT: Efficient RowHammer-Aware Test for Modern DRAM Modules. In *2021 IEEE European Test Symposium (ETS)* (pp. 1–6). IEEE. https://doi.org/10.1109/ETS50041.2021.9465436

Friedberg, I., McLaughlin, K., Smith, P., Laverty, D., & Sezer, S. (2017). STPA-SafeSec: Safety and security analysis for cyber-physical systems. *Journal of information security and applications*, *34*, 183–196. https://doi.org/10.1016/j.jisa.2016.05.008

Frigo, P., Giuffrida, C., Bos, H., & Razavi, K. (2018). Grand pawning unit: Accelerating microarchitectural attacks with the GPU. In *2018 IEEE Symposium on Security and Privacy* (sp) (pp. 195–210). IEEE. https://doi.org/10.1109/SP.2018.00022

Gruss, D., Lipp, M., Schwarz, M., Genkin, D., Juffinger, J., O'Connell, S., Yarom, Y. (2018). An-other flip in the wall of Rowhammer defenses. In *2018 IEEE Symposium on Security and Privacy* (SP) (pp. 245–261). IEEE. https://doi.org/10.1109/SP.2018.00031

Gruss, D., Maurice, C., & Mangard, S. (2016). Rowhammer. js: A remote software-induced fault attack in JavaScript. In *International conference on detection of intrusions and malware, and vulnerability assessment* (pp. 300–321). Springer. https://doi.org/10.1007/978-3-319-40667-1_15

Hassan, H., Tugrul, Y. C., Kim, J. S., Van der Veen, V., Razavi, K., & Mutlu, O. (2021). Uncovering In-DRAM RowHammer Protection Mechanisms: A New Methodology, Custom RowHammer Patterns, and Implications. In *MICRO-54: 54th Annual IEEE/ACM International Symposium on Microarchitecture* (pp. 1198–1213). https://doi.org/10.1145/3466752.3480110

Igure, V. M., Laughter, S. A., & Williams, R. D. (2006). Security issues in SCADA networks. *Computers & Security*, *25*(7), 498–506. https://doi.org/10.1016/j.cose.2006.03.001

Industrial control systems threat medley: spyware and malicious scripts on the rise in H1 2021. (2021). *Kaspersky*. Retrieved April 8, 2022 from https://www.kaspersky.com/about/press-releases/2021_industrial-control-systems-threat-medley-spyware-and-malicious-scripts-on-the-rise-in-h1-2021

Jang, Y., Lee, J., Lee, S., & Kim, T. (2017). SGX-Bomb: Locking down the processor via Row-hammer attack. In *Proceedings of the 2nd Workshop on System Software for Trusted Execution* (pp. 1–6). https://doi.org/10.1145/3152701.3152709

Johari, R., Kaur, A., Hashim, M., Rai, P. K., & Gupta, K. (2022). SEVA: Secure E-Voting Application in Cyber Physical System. *Cyber-Physical Systems*, *8*(1), 1–31. https://doi.org/10.1080/23335777.2020.1837250

Khaitan, S. K., & McCalley, J. D. (2014). Design techniques and applications of cyberphysical systems: A survey. *IEEE Systems Journal*, *9*(2), 350-365. https://doi.org/10.1109/JSYST.2014.2322503

Kim, J. S., Patel, M., Yağlıkçı, A. G., Hassan, H., Azizi, R., Orosa, L., & Mutlu, O. (2020). Revisiting Rowhammer: An experimental analysis of modern dram devices and mitigation techniques. In *2020 ACM/IEEE 47th Annual International Symposium on Computer Architecture (ISCA)* (pp. 638–651). IEEE. https://doi.org/10.1109/ISCA45697.2020.00059

Kim, Y., Daly, R., Kim, J., Fallin, C., Lee, J. H., Lee, D., Mutlu, O. (2014). Flipping bits in memory without accessing them: An experimental study of DRAM disturbance errors. *ACM SIGARCH Computer Architecture News*, *42*(3), 361–372. https://doi.org/10.1145/2678373.2665726

Lee, M., & Kwak, J. (2021). Detection Technique of Software-Induced Rowhammer Attacks. *CMC-Computers Materials & Continua*, *67*(1), 349–367.

Lieu Tran, T. B., Törngren, M., Nguyen, H. D., Paulen, R., Gleason, N. W., & Duong, T. H. (2019). Trends in preparing cyber-physical systems engineers. *Cyber-Physical Systems*, *5*(2), 65–91. https://doi.org/10.1080/23335777.2019.1600034

Lipp, M., Schwarz, M., Raab, L., Lamster, L., Aga, M. T., Maurice, C., & Gruss, D. (2020). Nethammer: Inducing Rowhammer faults through network requests. In *2020 IEEE European Symposium on Security and Privacy Workshops (EuroS&PW)* (pp. 710–719). IEEE. https://doi.org/10.1109/EuroSPW51379.2020.00102

Loukas, G. (2015). Cyber-physical attacks on industrial control systems. In *Cyber-Physical Attacks* (pp. 105–144). Elsevier.

Lu, T., Guo, X., Li, Y., Peng, Y., Zhang, X., Xie, F., & Gao, Y. (2014). Cyberphysical security for industrial control systems based on wireless sensor networks. *International Journal of Distributed Sensor Networks*, *10*(6), 438350. https://doi.org/10.1155/2014/438350

Mahmoud, M. S., & Hamdan, M. M. (2019). Improved control of cyber-physical systems subject to cyber and physical attacks. *Cyber-Physical Systems*, *5*(3), 173–190. https://doi.org/10.1080/23335777.2019.1631889

Mutlu, O. (2015). Main memory scaling: Challenges and solution directions. In *More than Moore technologies for next generation computer design* (pp. 127–153). Springer. https://doi.org/10.1007/978-1-4939-2163-8_6

Mutlu, O., & Kim, J. S. (2019). Rowhammer: A retrospective. *IEEE Transactions on Computer-Aided Design of Integrated Circuits and Systems*, *39*(8), 1555–1571. https://doi.org/10.1109/TCAD.2019.2915318

Mutlu, O., & Subramanian, L. (2014). Research problems and opportunities in memory systems. *Supercomputing frontiers and innovations*, *1*(3), 19–55.

Orosa, L., Yaglikci, A. G., Luo, H., Olgun, A., Park, J., Hassan, H., & Mutlu, O. (2021). A Deeper Look into RowHammer's Sensitivities: Experimental Analysis of Real DRAM Chips and Implications on Future Attacks and Defenses. In *MICRO-54: 54th Annual IEEE/ACM International Symposium on Microarchitecture* (pp. 1182–1197). https://doi.org/10.1145/3466752.3480069

Peng, Y., Wang, Y., Xiang, C., Liu, X., Wen, Z., Chen, D., & Zhang, C. (2015). Cyber-physical attack-oriented Industrial Control Systems (ICS) modeling, analysis and experiment environment. In *2015 International Conference on Intelligent Information Hiding and Multimedia Signal Processing (IIH-MSP)* (pp. 322–326). IEEE. https://doi.org/10.1109/IIH-MSP.2015.110

Qiao, R., & Seaborn, M. (2016). A new approach for Rowhammer attacks. In *2016 IEEE international symposium on hardware oriented security and trust (HOST)* (pp. 161–166). IEEE. https://doi.org/10.1109/HST.2016.7495576

Razavi, K., Gras, B., Bosman, E., Preneel, B., Giuffrida, C., & Bos, H. (2016). Flip feng shui: Hammering a needle in the software stack. In *25th USENIX Security Symposium (USENIX Security 16)* (pp. 1–18). USENIX Association.

Seaborn, M., & Dullien, T. (2015). Exploiting the DRAM Rowhammer bug to gain kernel privileges. *Black Hat*, *15*, 71.

Stouffer, K., Falco, J., & Scarfone, K. (2011). Guide to industrial control systems (ICS) security. *NIST special publication*, *800*(82), 16–16.

Tatar, A., Konoth, R. K., Athanasopoulos, E., Giuffrida, C., Bos, H., & Razavi, K. (2018). Throwhammer: Rowhammer attacks over the network and defenses. In *2018 USENIX Annual Technical Conference (USENIX ATC 18)* (pp. 213–226). USENIX Association.

Teixeira, M. A., Salman, T., Zolanvari, M., Jain, R., Meskin, N., & Samaka, M. (2018). SCADA system testbed for cybersecurity research using machine learning approach. *Future Internet*, *10*(8), 76. https://doi.org/10.3390/fi10080076

Van Der Veen, V., Fratantonio, Y., Lindorfer, M., Gruss, D., Maurice, C., Vigna, G.& Giuffrida, C. (2016). Drammer: Deterministic rowhammer attacks on mobile platforms. In *Proceedings of the 2016 ACM SIGSAC conference on computer and communications security* (pp. 1675–1689). https://doi.org/10.1145/2976749.2978406

Yağlikçi, A. G., Patel, M., Kim, J. S., Azizi, R., Olgun, A., Orosa, L., & Mutlu, O. (2021). Blockhammer: Preventing Rowhammer at low cost by blacklisting rapidly-accessed dram rows. In *2021 IEEE International Symposium on High-Performance Computer Architecture (HPCA)* (pp. 345–358). IEEE. https://doi.org/10.1109/HPCA51647.2021.00037

Yampolskiy, M., Horvath, P., Koutsoukos, X. D., Xue, Y., & Sztipanovits, J. (2013). Taxonomy for description of cross-domain attacks on CPS. In *Proceedings of the 2nd ACM international conference on High confidence networked systems* (pp. 135-142). ACM Digital Library https://doi.org/10.1145/2461446.2461465

Zhang, Z., Qi, J., Cheng, Y., Jiang, S., Lin, Y., Gao, Y., & Zou, Y. (2022). A Retrospective and Future-spective of Rowhammer Attacks and Defenses on DRAM. *arXiv preprint arXiv:2201.02986*. https://doi.org/10.48550/arXiv.2201.02986

Zimba, A., Wang, Z., & Chen, H. (2018). Multi-stage crypto ransomware attacks: A new emerging cyber threat to critical infrastructure and industrial control systems. *ICT Express*, *4*(1), 14–18. https://doi.org/10.1016/j.icte.2017.12.007

Applied Computer Science, vol. 18, no. 2, pp. 101–109
doi: 10.35784/acs-2022-16

Submitted: 2022-04-02 | Revised: 2022-05-16 | Accepted: 2022-05-21

Keywords: forward problem, ultrasound transmission tomography, sensors, machine learning, finite difference

Konrad KANIA [0000-0003-1545-0891]*, *Mariusz MAZUREK* [0000-0002-9646-6897]**, *Tomasz RYMARCZYK* [0000-0002-3524-9151]***

APPLICATION OF FINITE DIFFERENCE METHOD FOR MEASUREMENT SIMULATION IN ULTRASOUND TRANSMISSION TOMOGRAPHY

Abstract

In this work, we present a computer simulation model that generates the propagation of sound waves to solve a forward problem in ultrasound transmission tomography. The simulator can be used to create data sets used in the supervised learning process. A solution to the "free-space" boundary problem was proposed, and the memory consumption was significantly optimized from $O(n^2)$ to $O(n)$. The given method of simulating wave scattering enables the control of the noise extinction time within the tomographic probe and the permeability of the sound wave. The presented version of the script simulates the classic variant of a circular probe with evenly distributed sensors around the circumference.

1. INTRODUCTION

1.1. Ultrasound Transmission Tomography

Measurement methods using the information contained in the ultrasonic signal after its passage through the medium under test are called ultrasonic transmission methods (Polakowski, Rymarczyk & Sikora, 2020). The main advantage of ultrasonic testing is the non-invasive measurement in the tested environment, not causing any changes in physical and chemical parameters that could interfere with the measurement results. In addition, because ultrasound waves belong to the category of short waves, they possess propagation and radiation properties such that they can be treated as rays. The wavelengths of these waves depend on the medium they are radiated into and range from a few micrometres in liquids to tens of centimetres in metals. Therefore, they can be used to measure the attenuation coefficient and transit time of the ultrasonic signal in the medium subjected to their influence.

* Lublin University of Technology, Lublin, Poland, k.kania@pollub.pl
** Institute of Philosophy and Sociology of the Polish Academy of Sciences, Warsaw, Poland, mmazurek@ifispan.edu.pl
*** R&D Center Netrix S.A., Lublin, Poland; University of Economics and Innovation in Lublin, Lublin, Poland, tomasz@rymarczyk.com

Moreover, with the help of ultrasound, it is possible to make multiple measurements without fear of damage or irradiation of the tested objects. Measurements of such parameters as signal transit time, damping factor and its derivative after frequency allow, after appropriate reconstruction transformations, to image the internal structure of the tested medium and such flow parameters as its instantaneous velocity, average velocity or velocity profile. Differences in local values of specific acoustic parameters are the basis for such imaging. The image obtained using appropriate reconstruction methods presents the distribution of local values of selected acoustic parameters, obtained from the measurement of data with the scanning technique from as many directions as possible after the passage of ultrasonic impulses through the surveyed medium. In addition, this technique allows obtaining quantitative images of the internal structure, in which numerical values of each pixel describe such physical properties of the studied objects as flow velocity, temperature distribution, density, and viscosity (Antunes dos Santos Júnior, 2012). A characteristic feature of ultrasonic techniques is that the measurement of only two to three selected acoustic parameters can be the basis for a whole range of different measurement technologies because ultrasonic waves interact with the tested environment in many different ways (Polakowski & Sikora, 2016).

1.2. Finite difference approaches

This method was proposed by A. Thom in the twenties of the twentieth century, under the name of the "square method", to solve the nonlinear hydrodynamic equation. Since then, the method has found applications in solving various problems. Finite difference techniques are based on approximations that allow the differential equation to be replaced by finite difference equations. These approximations have an algebraic form. They bind the value of the dependent variable at the solution region point with the values at several adjacent points. The Finite Difference Method (FDM) is one of the most frequently used methods of approximating partial differential equations using a system of algebraic equations, which is usually solved using a computer (Degroot-Hedlin, 2008).

The areas in which the output equations are determined coincide with the solution grid, and the derivatives of the solution sought are approximated by appropriate difference quotients, using only values in the grid nodes. The so constructed differential scheme is used to determine the value of the approximate solution in the mesh nodes, and it leads directly to a system of equations with a special structure related to the local character of the approximation of the differential operator.

The classical method of finite differences is an approximate method of discrete solving of boundary problems described by ordinary or partial differential equations. The idea of the method is to replace the differential operators with appropriate differential operators, defined on a discrete and regular set of points; this set was called a mesh, and its elements were called nodes. As a result, the initial-boundary problem is reduced to a system of equations in which the values of the function and, in some cases, their derivatives are the unknowns (Bilbao, 2013).

The generalization of the classical method of finite differences is the method with an arbitrarily irregular mesh of nodes, also used to solve problems formulated in the variational form. The research conducted as part of the work was limited to applying the classical finite difference method to solve partial differential equations; solving ordinary or partial differential equations is elementary. Examples of applications can be found in textbooks on numerical

methods. During the research, the basic issue was the correct setting of the tasks, where an important element is the uniqueness of the solution and its continuous dependence on the right sides of the equations and boundary conditions that guarantee the stability of the differential problem. In addition, the research showed whether the approximate solutions converge to the exact solution and the speed of this convergence. In this way, information about the numerical correctness of the respective algorithms was also taken into account (Li Li, Shao & Li, 2019).

In the early 1990s, when wave-based approaches started to become computationally viable, finite difference methods started to be applied to the problem of simulating acoustics in low frequencies, using mathematical formulations stemming from analogous equations in electromagnetics (Botteldooren, 1994; Chiba et al., 1993; Mickens, 1994; Ishimaru, 2017) and, independently, stemming from developments in digital waveguide sound synthesis techniques (Asadzadeh, 2020). Other well-known families of numerical methods were also applied to acoustic problems, including finite volume (in the time domain) (Botteldooren, 1994) and finite element and boundary element methods in both times- and frequency domains (Svensson, Fred & Vanderkooy, 1999). However, concerning the methods implemented for the wave equation itself (i.e., in the time domain), finite difference methods seem to have gained the most popularity over the years, e.g. (Benito et al., 2020; Sullivan & Young, 2001; Liu, Ding & Sen, 2011; Liu & Sen, 2009; Kumar, 2004), most likely due to their simplicity in formulation and ease in implementation. Seminal texts on finite difference methods (and other numerical methods) include (Thomas, 2013; Forsythe & Wasow, 1960; Knabner & Angermann, 2021). See also (Thomée, 2001) for a detailed history of finite difference methods.

2. AIM OF THE RESEARCH

A modern approach to solving inverse ultrasound tomography problems aims to use novel methods based on machine learning techniques. As those methods are excellent for almost automatic search for solutions for complex problems, most ML algorithms are the supervised methods with the means to find a proper model for a problem. It needs to provide input data and referenced output data sets. In tomography, for training, e.g. deep neural network, we need to collect a large amount of measurement data with prior knowledge of the distribution of imaged medium. It leads to the technical problem that we need another reference method to solve the same problem and an inverse problem with one method. Another approach to that impasse is to create a forward problem solver capable of simulating measurement data on defined medium distribution. That type of solver needs to meet a few requirements. It must be quick and thus simple enough to generate large data sets. Moreover, simulations need to allow for easy defining a broad range of heterogeneous distributions inside the tomographic probe. This research aimed to create a simple but sufficiently versatile framework for the quick generation of simulations suitable for tomographic applications, focusing on machine learning techniques.

In the future work, authors plan to use created simulations as a start point for various types of tomographic problems like examination of the shapes of sensitivity maps of tomographic settings, experimentations of transducers excitations patterns, application of style-transfer learning for forward and inverse problems, designing compression algorithms for ultrasound measurement data etc.

3. COMPUTER SIMULATION MODEL

Based on the simulation of acoustic wave propagation on a regular square grid, we measure the value of acoustic pressure that excites the movement of the diaphragm of the measurement sensor, causing the excitation of an electric voltage. Such an approach gives the possibility of solving a forward problem. It consequently allows the creation of learning sets used in machine learning, especially in supervised deep learning.

Simulation of acoustic wave propagation inside the tomographic probe is necessary to reflect the wave propagation and generated voltages in sensors at a given distribution of the internal medium of the probe. Such a situation is not fully possible to reproduce in real measurements and, at the same time, is very time consuming and requires a significant amount of work. Machine learning requires tagged sets with large volumes, even up to several tens of thousands. Moreover, real measurements performed by a human can be burdened with uneven distribution of objects inside the tomographic probe, which lead to biased measurement data set, which can affect the learning capabilities of neural network.

Radial models are commonly used to solve the inverse problem (Kania et al., 2019). However, despite the effectiveness of these models in imaging on real measurement systems, it is not possible to use them to simulate acoustic processes (Kania, Rymarczyk, Maj & Gołąbek, 2019). In work (Kania et al., 2020), an attempt was made to simulate acoustic phenomena using ray tracing with Fermat's principle, thus succeeding in tracing acoustic wave trajectories and reproducing the lensing phenomenon depending on the objects and the medium filling the measurement probe. However, due to technical problems, using this method for simulation is not an effective method of carrying it out. Furthermore, these problems generated the need to use finite difference methods to solve the wave equation.

3.1. Finite difference methods for the wave equation

The simulation is performed on a grid of 128x128 spatial nodes during 8000 steps, on a 40x40 cm square with a probe with a diameter of 20 cm. A sequence of 16 sensors triggered with intervals of 500 steps is simulated with the time of activation: 20 iterations and sinusoidal excitation:

$$U = Asin(wt) \tag{1}$$

where: $A = 10$,
$w = 1.0$.

Full simulation of the measurement sequence (8000 iterations, 16 sensors) is determined in about 7 seconds (on an i9-11900F processor) due to the stability conditions, which corresponds to approximately 12 ms of real-time.

First, matrix boundary conditions were implemented, taking into account the acoustic impedance of the "walls" of the simulated area. Through numerical experiments, it turned out that implementation of the lossy condition does not allow for the simulation of the total absorption of the wave by the border of the simulation area. By analyzing the free-space boundary problem, i.e. the condition in which the wave freely "flies" across the simulated boundary, it has been established that there are currently no typical boundary conditions for

two-dimensional and/or more-dimensional problems. The most common solution to the problem is to extend, in some way, the scope of the simulation beyond the area of interest. Ultimately, therefore, the scope of the simulation was increased, and the wave energy outside the probe circle was periodically reset to zero once for a specified number of simulation steps (in this case, Fig. 1, once every 100 iterations). Increasing the simulation area allows modelling the wave "drift" outside the region of interest. After erasing the wave outside the region of interest, the wave in the probe propagates further undisturbed.

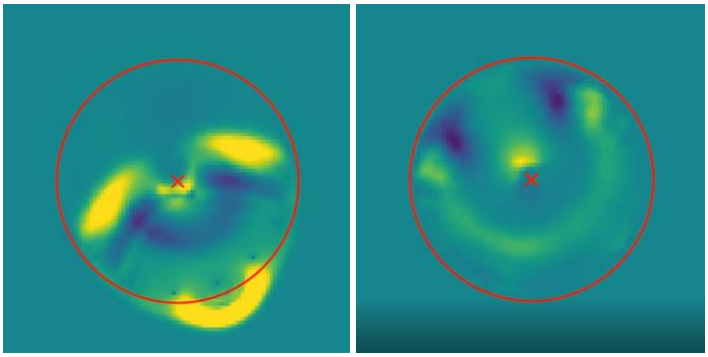

Fig. 1. Simulation results: a collision of an acoustic wave on a square object filled with air (left) and view of the wave passing behind the object (right)

The number of frames after which the deletion takes place is selected in such a way that the wave has, on the one hand, sufficient time to escape from the probe, on the other hand, so that its reflection from the border of the simulated area does not return to the interior. Therefore, it is indirectly related to the allowance to the simulated domain to be considered in determining the area of interest of the simulation. The necessity to increase the simulation area in relation to FOV causes the reconstructed to be indisputably more pixels than results from the FOV size alone. Using the implementation of the simulation, taking into account the lossy boundary conditions, based on the matrix equation, we have:

$$u^{t+1} = (\lambda B + I)^{-1}(2I + \lambda^2 L)u^t + (\lambda B - I)u^{t-1} \tag{2}$$

We must therefore store in memory two matrices of size $n^2 \times n^2$, where the simulation is performed over the area of size $n \times n$. The rigid implementation of the Dirichlet conditions allows to simplify the equation to the formula:

$$u^{t+1} = (2I + \lambda^2 L)u^t - u^{t-1} \tag{3}$$

However, we still need at least one matrix of sizes $n^2 \times n^2$, which means that the simulation still needs $O(n^2)$ memory. To reduce this problem, an equivalent implementation based on the convolutional filter was used:

$$u^{t+1} = 2u - u^{t-1} + \lambda^2 Conv(u, L) \tag{4}$$

where: $L = \begin{pmatrix} 0 & 1 & 0 \\ 1 & -4 & 1 \\ 0 & 1 & 0 \end{pmatrix}$ is a filter implementing the discrete Laplacian.

Thanks to this, apart from the necessity to store u^{t+1}, u^t, u^{t-1} tables in the memory, there is no need for additional memory apart from the 3x3 table of the convolutional filter. We should also note that such implementation does not require u matrix expansion into vectors, as in the case of matrix equations. In addition, by experimenting, the simulation is more stable for the "soft" Laplacian variant, which is used in the simulation:

$$L^* = \begin{pmatrix} 0.25 & 0.5 & 0.25 \\ 0.5 & -3 & 0.5 \\ 0.25 & 0.5 & 0.25 \end{pmatrix} \tag{5}$$

The condition for the stability of the simulation for Laplacian L is the so-called Courant-Friedrichs-Lewy condition:

$$\lambda = \frac{v\,dt}{dx} \leq \sqrt{0.5} \approx 0.0707 \tag{6}$$

where: v – wave velocity at a node,
dx – the actual distance between nodes,
dt – actual time step length.

In practice, to meet this condition, the values of dt and dx are selected so that:

$$\lambda_c = \frac{c\,dt}{dx} = 0.07 \tag{7}$$

where: c – the maximum wave speed used in the simulation.

Thanks to this, by simulating the values of $lam \in [0, \lambda_c]$ on the mesh nodes, we can be sure that the stability of the simulation will be ensured. In this context, it turns out that the use of L^* Laplacian allows a slight increase in the range of lam values over λ_c (Fig. 2).

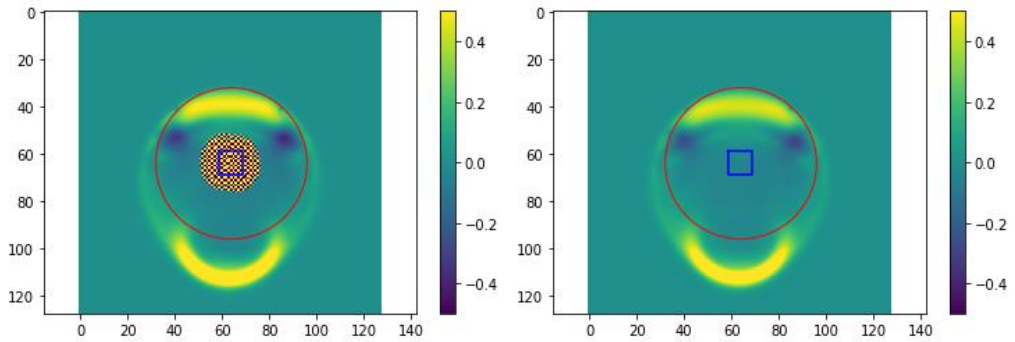

Fig. 2. Wave passage through an obstacle (the same 86th frame of simulation) not meeting the theoretically CFL condition ($lam = 1.2\lambda_c$), using Laplacian L (left, destabilization) and L^* (right, no destabilization artefact) – axis ticks in figures are pixel numbers (32 pixels correspond to 10 cm)

An additional aspect of the simulation is that in making a series of measurements, we must wait until after one sensor is excited until the acoustic wave inside is attenuated enough to not interfere with the wave produced by the next transmitter.

In the model currently used, the scattering factor was not considered, resulting in the probe's interior never reaching the level of complete silence. In order to control the wave scattering, Gauss Kernel Filter has been added to the simulation step. This way, by controlling the variance of the filter, the scattering of the wave can be increased (Fig. 3).

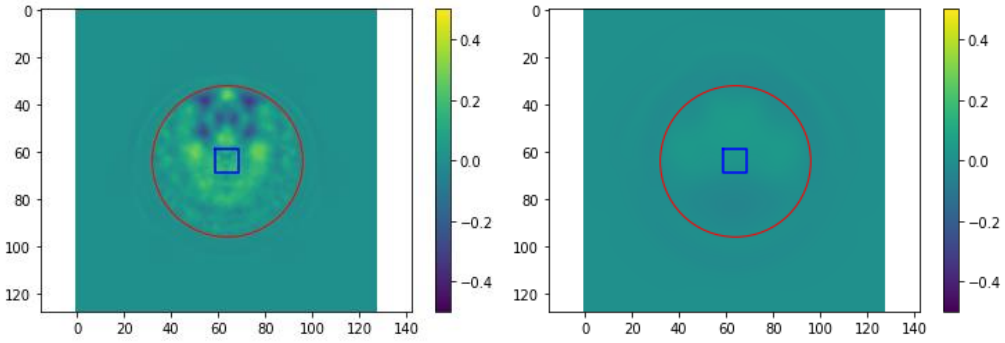

Fig. 3. View 390 of the simulation frame without dispersion $\sigma = 0$ (left) and with the same parameters but with dispersion $\sigma = 0.4$ (right) – axis ticks in figures are pixel numbers (32 pixels correspond to 10 cm)

By taking into account the dispersion, we can obtain much cleaner measurement waveforms, as the calming of the waveform does not disturb the measurement readings in the vicinity of the sensors.

The first extreme will be the variant without attenuation, where there is significant wave collimation and no mute (Fig. 4).

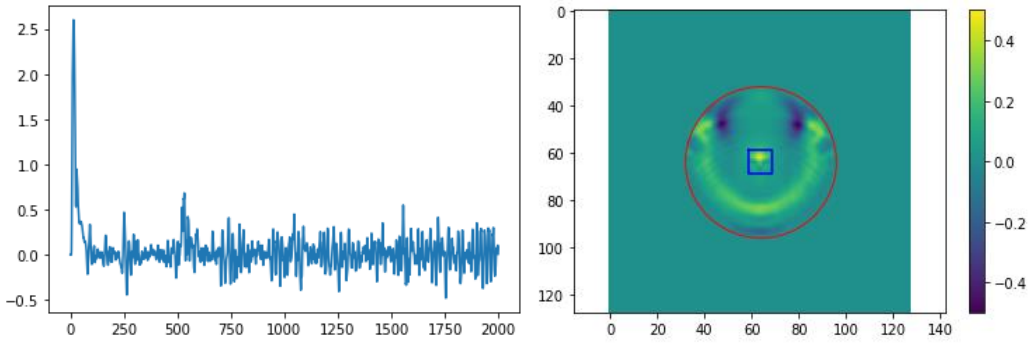

Fig. 4. Simulated measurement series of probe no. 0 for the first 2000 simulation steps at $\sigma = 0$ (left, X-axis descriptions are the number of iterations) and the effect of wave collimation on the circular edge of the probe $\sigma = 0$ (right)

On the other hand, too high attenuation causes almost undisturbed wave passage through the probe, eliminating the collimation effect, but we get much "cleaner" waveforms of the pulses (Fig. 5).

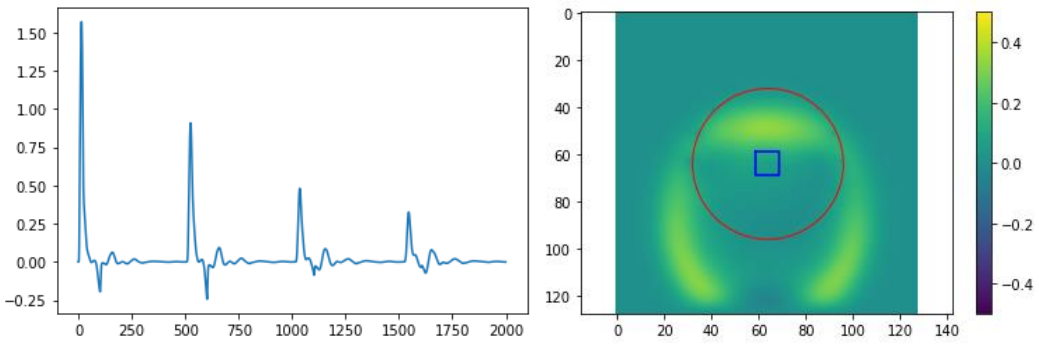

Fig. 5. Measurement of probe no. 0 for the first 2000 simulation steps at $\sigma = 1.0$ (left, X-axis descriptions are the number of iterations) and significant "blur" ($\sigma = 1.0$) of the wave eliminating collimation (right)

4. CONCLUSIONS

The results obtained so far allow for efficient and easy to perform simulations of acoustic phenomena on an arbitrary velocity distribution inside the probe, which will allow for the generation of simulated data sets of any size.

Finite difference methods comprise a simple starting point for such simulations, but they are known to suffer from approximation errors that may necessitate expensive grid refinements to achieve sufficient accuracy levels. As such, research has gone into designing finite difference methods that are highly accurate while remaining computationally efficient. A solution to the "free-space" boundary problem was proposed, and the memory consumption was significantly optimized from $O(n^2)$ to $O(n)$. The given method of simulating wave scattering enables the control of the noise extinction time within the tomographic probe and the permeability of the sound wave.

Further work will concern the verification of the simulator with real measurements (selection of parameters and signal conditioning) and the implementation of the possibility of defining custom measurement sequences, including those that enable beam-forming.

Author Contributions

Development of the concept of the simulator, research methodology, and implementation of in ultrasound transmission tomography, KK.; Development of the system concept, measurement methodology, techniques, image reconstruction and supervision, T.R.; Preparation of research methodology, literature review, formal analysis, general review, and editing of the manuscript, M.M. All authors have read and agreed to the published version of the manuscript.

Funding

This research received no external funding.

Conflicts of Interest

The authors declare no conflict of interest.

REFERENCES

Antunes dos Santos Júnior, A. (2012). *Ultrasonic Waves*. BoD – Books on Demand.

Asadzadeh, M. (2020). *An introduction to the finite element method for differential equations*. John Wiley & Sons.

Benito, J., García, A., Gavete, L., Negreanu, M., Ureña, F., & Vargas, A. (2020). Solving a fully parabolic chemotaxis system with periodic asymptotic behavior using generalized finite difference method. *Applied Numerical Mathematics*, *157*, 356–371. https://doi.org/10.1016/j.apnum.2020.06.011

Bilbao, S. (2013). Modeling of complex geometries and boundary conditions in finite difference/Finite volume time domain room acoustics simulation. *IEEE Transactions on Audio, Speech, and Language Processing*, *21*(7), 1524–1533. https://doi.org/10.1109/tasl.2013.2256897

Botteldooren, D. (1994). Acoustical finite-difference time-domain simulation in a quasi-Cartesian grid. *Journal of the Acoustical Society of America*, *95*, 2313–2319.

Chiba, O., Kashiwa, T., Shimoda, H., Kagami, S., & Fukai, I. (1993). Analysis of sound fields in three-dimensional space by the time-dependent finite-difference method based on the leapfrog algorithm. *Journal Acoustical Society of Japan*, *49*, 551–562.

Degroot-Hedlin, C. D. (2008). Finite difference time domain synthesis of infrasound propagation through an absorbing atmosphere. *The Journal of the Acoustical Society of America*, *123*(5), 3839–3839. https://doi.org/10.1121/1.2935641

Forsythe, G. E., & Wasow, W. R. (1960). *Finite-difference methods for partial differential equations*. John Wiley & Sons.

Ishimaru, A. (2017). *Electromagnetic wave propagation, radiation, and scattering: From fundamentals to applications*. John Wiley & Sons.

Kania, K., Maj, M., Rymarczyk, T., Adamkiewicz, P., & Gołąbek, M. (2020). Image reconstruction in ultrasound transmission tomography using the Fermat's principle. *Przegląd Elektrotechniczny*, *1*(1), 188–191. https://doi.org/10.15199/48.2020.01.41

Kania, K., Rymarczyk, T., Maj, M., & Gołąbek, M. (2019). *2019 applications of electromagnetics in modern engineering and medicine (PTZE)*. IEEE. https://doi.org/10.23919/PTZE.2019.8781687

Kania, K., Rymarczyk, T., Maj, M., Gołąbek, M., Adamkiewicz, P., & Sikora, J. (2019). *2019 international interdisciplinary PhD workshop (IIPhDW)*. IEEE. https://doi.org/10.1109/IIPHDW.2019.8755416

Knabner, P., & Angermann, L. (2021). *Numerical methods for elliptic and parabolic partial differential equations: With contributions by Andreas Rupp*. Springer Nature.

Kumar, A. (2004). Isotropic finite-differences. *Journal of Computational Physics*, *201*(1), 109–118. https://doi.org/10.1016/j.jcp.2004.05.005

Li, W., Li, S., Shao, X., & Li, Z. (2019). *Proceedings of the 6th conference on sound and music technology (CSMT): Revised selected papers*. Springer.

Liu, Y., & Sen, M. K. (2009). A new time-space domain high-order finite-difference method for the acoustic wave equation. *Journal of Computational Physics*, *228*(23), 8779–8806. https://doi.org/10.1016/j.jcp.2009.08.027

Liu, Y., Ding, L., & Sen, M. K. (2011). Comparisons between the hybrid ABC and the PML method for 2D high-order finite-difference acoustic modeling. *SEG Technical Program Expanded Abstracts 2011*. https://doi.org/10.1190/1.3627807

Mickens, R. E. (1994). *Nonstandard finite difference models of differential equations*. World Scientific.

Polakowski, K. A., Rymarczyk, T., & Sikora, J. (2020). *Obrazowanie ultradźwiękowe: Wybrane algorytmy obrazowania*. Oficyna Wydawnicza Politechniki Warszawskiej.

Polakowski, K., & Sikora, J. (2016). *Podstawy matematyczne obrazowania ultradźwiękowego*. Politechnika Lubelska.

Sullivan, D., & Young, J. (2001). Far-field time-domain calculation from aperture radiators using the FDTD method. *IEEE Transactions on Antennas and Propagation*, *49*(3), 464–469. https://doi.org/10.1109/8.918622

Svensson, U. P., Fred, R. I., & Vanderkooy, J. (1999). An analytic secondary source model of edge diffraction impulse responses. *The Journal of the Acoustical Society of America*, *106*(5), 2331–2344. https://doi.org/10.1121/1.428071

Thomas, J. (2013). *Numerical partial differential equations: Finite difference methods*. Springer Science & Business Media.

Thomée, V. (2001). From finite differences to finite elements a short history of numerical analysis of partial differential equations. *Partial Differential Equations*, *2001*, 1–54. https://doi.org/10.1016/b978-0-444-50616-0.50004-x